Pt(IV) anticancer prodrugs and liposomal encapsulation

Laura Kay Marsh

Hertford College
University of Oxford

A thesis submitted for the degree of
Doctor of Philosophy
August 2022

Contents

Abstract

This work describes the development of several photoactivatable platinum based anticancer prodrugs. The use of liposomes as a method of drug encapsulation for a known platinum complex is also explored. Finally, the synthesis of a microbubble-liposome conjugated system and the sonoluminescence effect of microbubbles are assessed.

Chapter 1 discusses the fundamental properties of platinum, how it is currently utilised in chemotherapy, and the potential benefits of light-activated platinum compounds. The use of liposomes in medicine, with particular focus on drug encapsulation, is discussed in detail. The clinical applications of microbubbles are also explored.

Chapter 2 describes the development and characterisation of two novel photoactivatable Pt^{IV} complexes. The solubilities, photochemical properties and pK_a values of these compounds are compared to those of two previously reported complexes.

Chapter 3 reviews the use of liposomes for the encapsulation of the drug iproplatin, with exploration of the best active loading method for this compound, and how the composition of the liposomes can be adapted to improve drug retention.

Chapter 4 discusses the optimisation of synthesis for a conjugated microbubble-liposome drug delivery system. The phenomenom of sonoluminescence, and it's potential use for activating photosensitive compounds is also explored.

Chapter 5 describes the conclusions for this work, and what the next steps of this research would involve.

Chapter 6 provides the experimental procedures and synthetic methods used in this work.

Publications

1. M. H. C. Boulet, L. K. Marsh, A. Howarth, A. Woolman and N. J. Farrer, *Dalt. Trans.*, 2020, **49**, 5703-5710, DOI:10.1039/c9dt04862f.

2. R. Browning, N. Thomas, L. K. Marsh, L. R. Tear, J. Owen, E. Stride and N. J. Farrer, *Chem. Open*, 2021, **10**, 1170-1176, DOI:10.1002/open.202100222.

Acknowledgements

Firstly I would like to say a huge thank you to Dr. Nicola Farrer, without whom this research project wouldn't even have existed. I'm so grateful to have been given such an incredible opportunity, and thank you for your support with my work over the past few years.

Secondly, I would like to say thank you to my co-supervisor Prof. Stephen Faulkner. Your generosity and compassion are unequalled, and there have been moments in which I don't know what I would have done without your wisdom and kind words.

Thank you to Prof. Stephen Evans and Aileen Delaney at the University of Leeds for their collaboration on the cross-linked liposomes. Thank you to Prof. Eleanor Stride and Dr. Richard Browning at the University of Oxford for their collaboration on the microbubble work included in this thesis.

To the members of the Farrer and Faulkner groups, thank you for all of the wonderful memories from my time in Oxford, both in and out of the lab. To Marie, who has been by my side for almost all of my DPhil and who has provided both incredible laughs and a shoulder to cry on. Thank you for the endless food and book recommendations, and for always knowing the difference between a good day and a bad day. To Louis, for all of the terrible jokes and accents that made so many days more bearable. To Clara, for your incredible chemistry knowledge and for your friendship and support. Your resilience and self-assuredness are admirable, don't ever let that be taken away from you. To Shitong, for being the best desk buddy and cocktail maker anyone could ask for. To Jevon, for providing so much unbridled joy. Your drive and positive outlook are inspirational. To Grace and Debs, for being my comrades in the trenches of HPLC repairs. To Kezi, for generally being wonderful and teaching me how to use HPLC

in the first place. Lastly, thank you to Agnes, Carlson, and Tom. The lab wouldn't have been the same without you.

Thank you to all my friends outside of Oxford for providing escapism and distraction when it was most needed. Special mentions go to Ella and Sonia. Thank you both for all of your support throughout, it has meant the world to me.

Thank you to my family; mum, nan, Maria, and Ben. You might not really understand what I've been doing, but thank you for believing in me and being there for me when I've needed it. Thank you to my dad, who didn't get to see me achieve any of this, but who I know would have been so proud of me.

Finally, the biggest thank you of all goes to my partner Corrie. I wouldn't have been able to get through the past two years without you, let alone finish this DPhil. Your love, encouragement, support, and unwavering faith in my abilities has been vital for me to get to this point. Thank you for picking me up whenever I was down, and for bringing so much happiness into my life.

Abbreviations

A	adenine
AU	arbitrary units
C	cytosine
CNS	central nervous system
CSA	chemical shift anisotropy
δ	delta
DIPG	diffuse intrinsic pontine glioma
DLS	dynamic light scattering
DNA	deoxyribonucleic acid
DSC	differential scanning calorimetry
EPR	enhanced permeability and retention
ES	electrospray
ESI	electrospray ionisation
eq	equivalents
FDA	food and drug administration
G	guanine
HPLC	high performance liquid chromatography
HRMS	high resolution mass spectrometry
ICP-MS	inductively coupled plasma mass spectrometry
IM	ionic membrane
^{i}Pr	isopropyl
M	mol dm^{-3}
M	parent molecule
mmol	millimoles
mM	mmol dm^{-3}
mol	moles

μm	micrometre
MS	mass spectrometry
m/z	mass/charge
nm	nanometre
NMR	nuclear magnetic resonance
PACT	photoactivated chemotherapy
PdI	polydispersity index
PDT	photodynamic therapy
ppb	parts per billion
ppm	parts per million
py	pyridine
pz	pyrazine
ROS	reactive oxygen species
RT	room temperature
T	thymine
tz	thiazole
UV-vis	ultraviolet-visible

Chapter 1 Introduction

The properties of platinum (Pt) complexes have long made them useful in the anticancer sector. This thesis will explore how established systems can be modified for improved treatment and for targeting specific types of cancer, namely diffuse intrinsic pontine glioma (DIPG). Mechanisms of drug delivery utilizing liposomes, microbubbles and ultrasound will also be discussed.

1.1 Diffuse intrinsic pontine glioma

A glioma is a type of tumour that originates in the glial cells, which provide support and insulation for neurons, of the central nervous system (CNS). DIPG is a type of high grade glioma, with a peak onset age of between 6 and 9 years old. It occurs within the pons, which is a section of the brainstem. Paediatric DIPG accounts for 10-20% of all paediatric brain cancers. Paediatric DIPG accounts for 10-20% of all paediatric brain cancers.[1] Symptoms show variation depending on the position and size of the lesion in the pons, but over 50% of cases present with a triad including; cranial nerve defects, cerebellar damage, and spinal cord damage.[2]

Currently, radiotherapy is the only treatment to show some efficiency in extending progression-free survival (PFS).[3] It can also provide improved neurological function and relief of some symptoms.[4] At present, there are no chemotherapeutic agents that improve overall survival (OS) or PFS.[5] Clinical trials for cisplatin and carboplatin, both alone or in conjunction with radiotherapy, have shown modest benefits.[6]

There is ongoing research into the effect of various mutations, and how the epigenetic changes that they cause are relevant in paediatric cancers. Research by both Jones and Monje have focussed on the H3-K27M mutation as being a driver mutation in cases of paediatric DIPG.[7,8] Research into the genetic contribution to, both the risk and expression of, DIPG allows for development of novel therapeutic agents which can target these mutations in an attempt to find an effective treatment.

One of the main issues encountered when trying to treat DIPG by chemotherapy is that drugs administered intravenously are not able to reach the tumour site due to the presence of the blood-brain barrier (BBB).[9] The BBB is a semipermeable layer of endothelial cells that prevents solutes in the blood from crossing into the extracellular fluid of the CNS.[10] Research has found that the use of focused ultrasound, in conjunction with microbubbles, can temporarily open the BBB.[11] This makes it more permeable to solutes circulating in the blood, and could therefore improve the delivery of drugs into this region.

1.2 Platinum chemistry

Platinum is a d-block element with the electronic configuration '[Xe] $4f^{14}$ $5d^{9}$ $6s^{1}$'. It is also a transition metal as it has an incomplete d subshell. In its +2 oxidation state platinum is a d^{8} metal, with 4 coordination availability, which forms square planar complexes. The preference for Pt^{II} to form square-planar complexes, rather than tetrahedral, is due to the ligand field stabilisation that comes from occupying the d_{xz}, d_{yz}, d_{z^2}, and d_{xy} orbitals. Platinum can also commonly access the +4 oxidation state, where it becomes 6 coordinate and forms octahedral complexes. In a Pt^{IV} complex, the metal centre is in a low spin d^{6} configuration with the t_{2g} orbitals (d_{xy}, d_{xz}, and d_{yz}) being fully occupied (Figure 1.1)

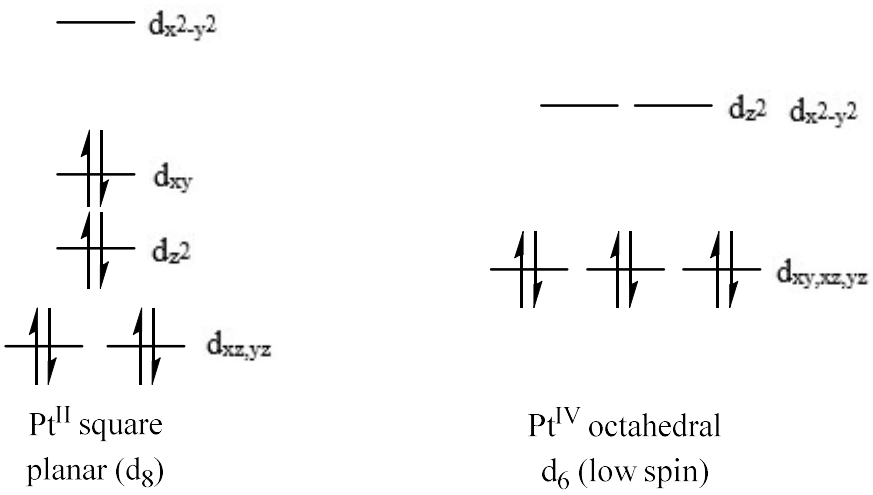

Figure 1.1 Crystal field splitting of the d-orbitals in Pt^{II} (square planer, d^{8}) and Pt^{IV} (octahedral, d^{6}) configurations.

Platinum has six naturally occurring isotopes; ^{190}Pt, ^{192}Pt, ^{194}Pt, ^{195}Pt, ^{196}Pt and ^{198}Pt, with ^{195}Pt being the most abundant at 33.82% of the total abundance. ^{195}Pt is also the only NMR active isotope (spin quantum number, $I = ½$), and as such it can be used in the direct observation of Pt NMR resonances. The signal to noise ratio is relatively low, giving rise to sharp signals. Chemical shifts for ^{195}Pt NMR spectroscopy range from +8000 to –7000 ppm, with the Pt nucleus being sensitive to several factors in the chemical environment; oxidation state, ligand substituents, stereochemistry, solvent and solvation effects, and temperature.[12] Small changes in the chemical environment can therefore result in large changes in the observed chemical shift. Figure 1.2 shows the approximate chemical shift ranges for different oxidation states of Pt. The lower the oxidation state, the higher the electron density at the Pt centre. This leads to increased shielding and a more upfield chemical shift.

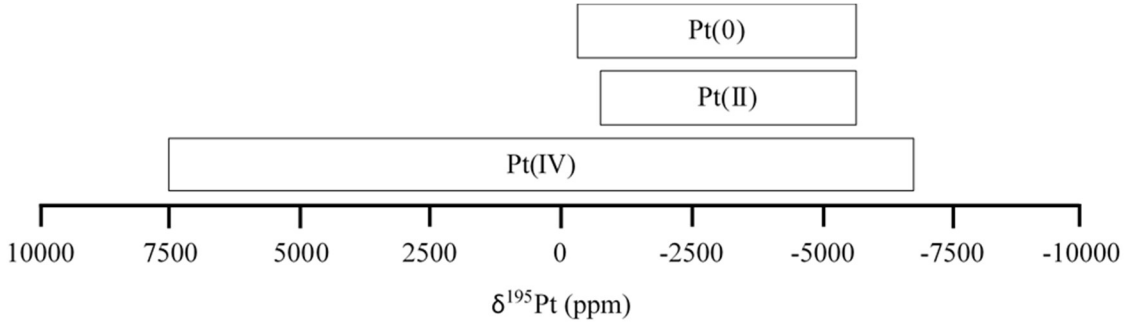

Figure 1.2 Approximate range of chemical shifts for different oxidation states of Pt. The chemical shifts are relative to $[PtCl_6]^{2-}$ in D_2O (adapted from Still et al.[12]).

The ^{195}Pt isotope can also couple to other nuclei, leading to the appearance of 'Pt satellites' (Figure 1.3) in the spectra of those elements. The splitting of these satellites presents as a symmetrical doublet around the central resonance, with the ratio of intensities approximately 1:4:1.[13]

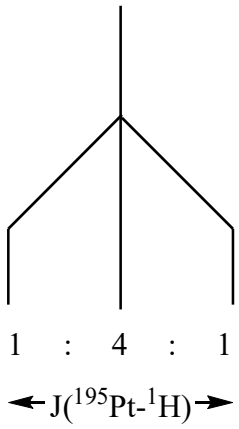

Figure 1.3 Diagram displaying 'Pt satellites' arising from coupling in a ^{1}H-NMR.[13,14]

The linewidth of the ^{195}Pt satellites varies between Pt^{II} and Pt^{IV} complexes, with the former having broader resonances and the latter having sharper peaks. This is due to Pt^{II} square planar complexes experiencing a much greater chemical shift anisotropy (CSA) effect because of their reduced symmetry.[14] The reduced symmetry means the opposing magnetic field for these Pt^{II} complexes is more anisotropic, leading to shorter relaxation times and broader resonances.[15]

1.2.1 Platinum^{II} in chemotherapy

Cisplatin is one of only three platinum-containing anticancer drugs approved by the FDA for use in humans worldwide (Figure 1.4). It was first synthesised by Peyrone in 1844, and its structure described by Werner in 1894, however its potential biological activity wasn't realised until 1965 by Barnett Rosenberg.[16,17] It has since paved the way for much research into platinum based chemotherapeutics.

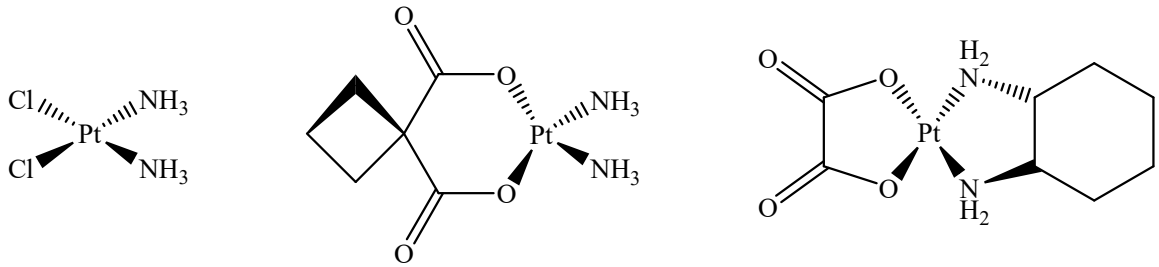

Figure 1.4 Structures of the three FDA approved Pt^{II} anticancer drugs; cisplatin, carboplatin, and oxaliplatin.[18]

There are three further platinum-containing drugs that are approved for human treatment in certain parts of Asia (Figure 1.5). These are nedaplatin, lobaplatin and heptaplatin, and are clinically used in Japan, China and Korea respectively.[19]

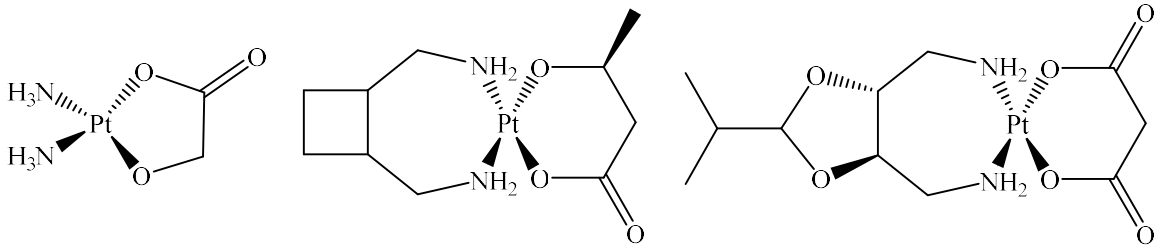

Figure 1.5 Structures of the three Pt^{II} drugs approved throughout Asia; nedaplatin, lobaplatin, and heptaplatin.

There are several design features that are common to all six of these drugs. Firstly, they are all neutral square planar Pt^{II} complexes. They also have similar ligand structures with there consistently being either two *cis* chloride ligands or a single dioxygen chelating ligand, and either two *cis* amine groups or a single diamine chelating group.[20]

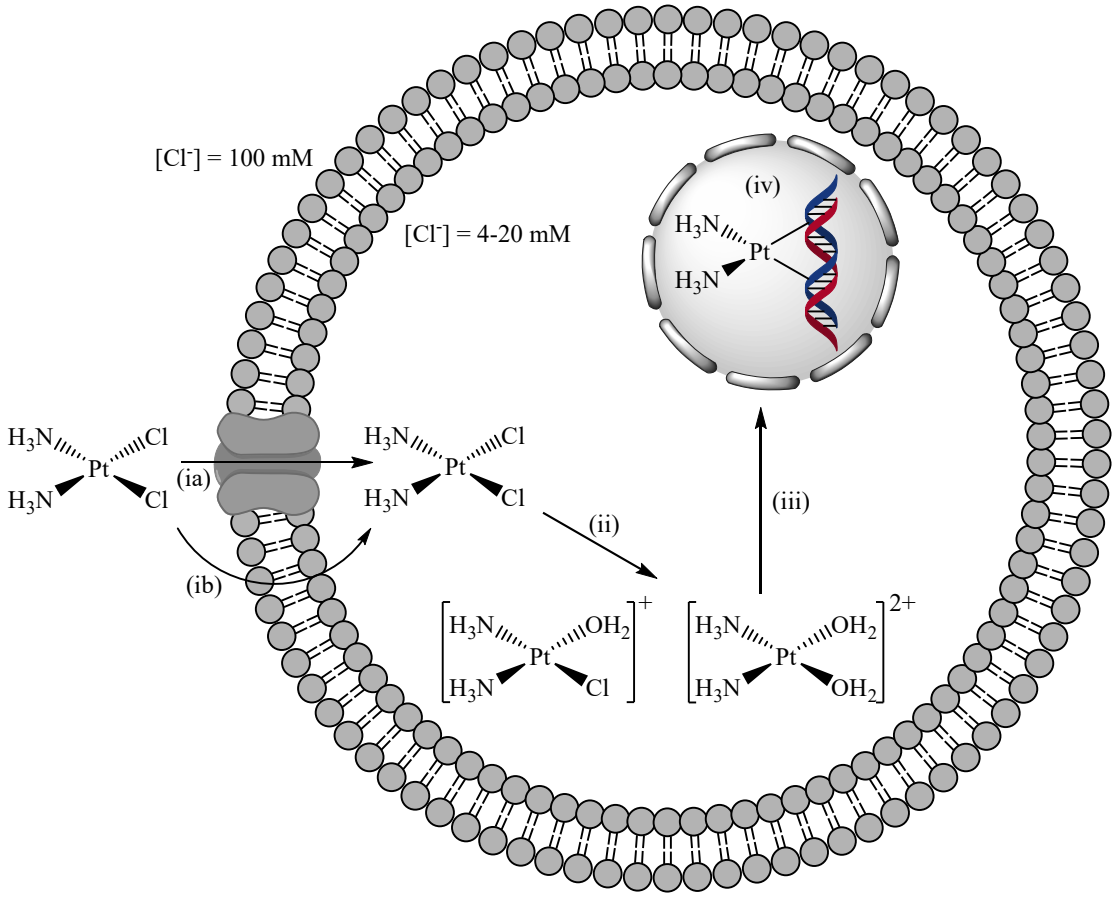

Figure 1.6 The mechanism of action for cisplatin in the cell (adapted from Zhao et al.[21]).

The mechanism of action for cisplatin, shown in Figure 1.6, is understood to occur in four key stages. The first step is cellular uptake (i). This can occur by either of two methods; (ia) active transport via a copper transporter protein, or (ib) passive diffusion.[22,23] Once the drug is inside the cell wall, aquation (ii) can occur. This is where one or both of the chloride ligands are replaced by water groups, to give the mono- and bis-substituted adducts. The disparity in the concentration of chloride ions between the intra- and extracellular matrix, and the higher concentrations of cisplatin in the cell, allows for this aquation to occur.[24,25] Aquated products are then able to enter the nucleus through nuclear pores (iii). The final step (iv) is the binding of cisplatin to the DNA in the nucleus, leading to deformation of the double helix.[26] The drug binds to the DNA by substitution of the Pt-coordinated water molecules with the heterocyclic

DNA base guanine.[27] Adenine is also able to be platinated, however studies have shown that there is a preference for guanine.[28] ^{195}Pt NMR studies have shown that the drug initialy forms a monosubstituted complex with the DNA, before the remaining chloride can be exchanged.[29] The damage this binding causes to the normal structure of DNA leads to initiation of the cellular processes that cause apoptosis.[30]

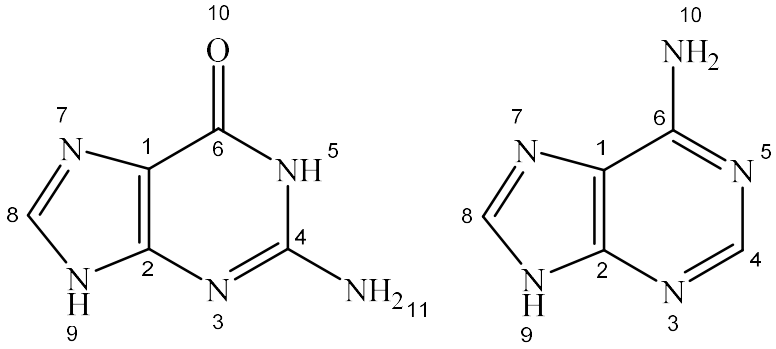

Figure 1.7 Structures of guanine (left), and adenine (right).

It is the N_7 position of guanine and adenine that are most favourably platinated due to their high (Figure 1.7).[31] Cisplatin is able to bind to neighbouring deoxyguanosine nucleobases that are not necessarily on the same strand of DNA. This can therefore give rise to interstrand and intrastrand cross-links (Figure 1.8). Intrastrand cross-links are the most frequently occurring, with the most common being 1,2-d(GpG) (65%). Other common intrastrand cross links are the 1,2-d(ApG) (25%), and the 1,3-d(GpTpG) (5-10%). Some GG interstrand links are seen, but these are less frequently occurring.[32]

There are other mechanisms via which cisplatin exerts cytotoxicity, such as by increasing the levels of reactive oxygen species (ROS) which, due to the effects of oxidative stress on biological function, can lead to cell death.[33] One method of ROS production may arise from cisplatin altering mitochondrial function through nicotinamide adenine dinucleotide phosphate (NADPH) depletion, which may increase the presence of $OH^{\cdot}$ and O_2^{-}.[34,35] It has also been

suggested that, in the treatment of head and neck cancer, interaction with mitochondria may be critical in the drug's clinical activity.[36,37]

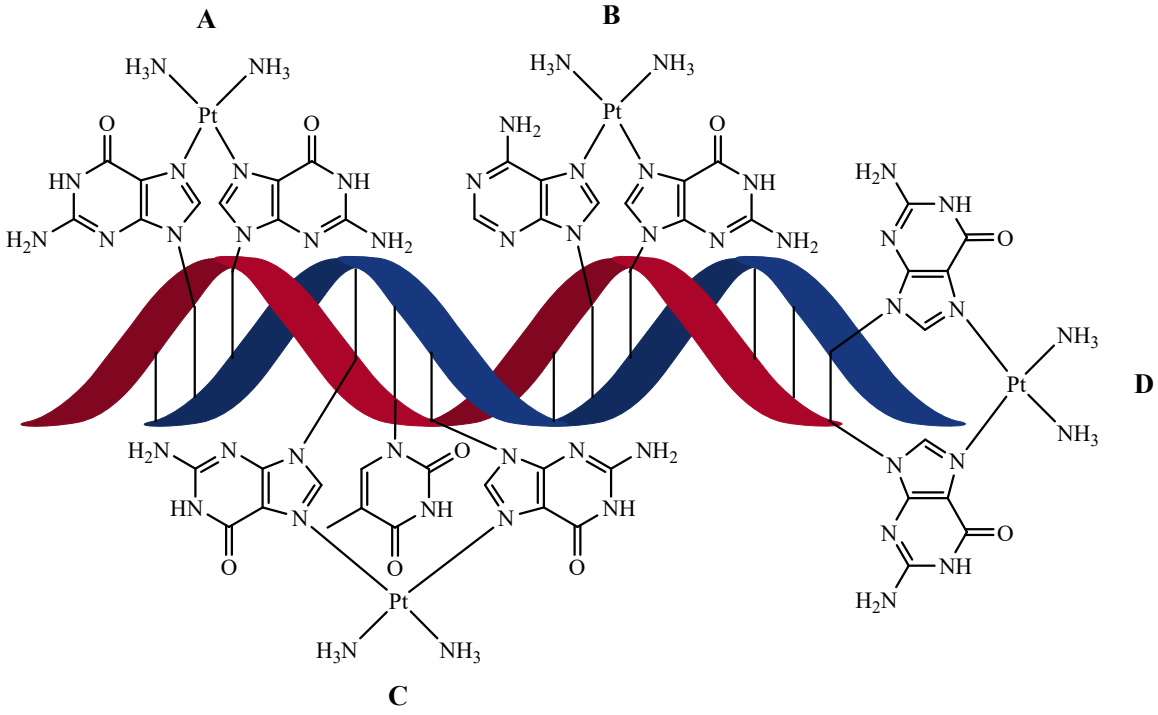

Figure 1.8 Schematic diagram of DNA with the most common Pt cross-links. (A) intrastrand 1,2-d(GpG), (B) intrastrand 1,2-d(ApG), (C) intrastrand 1,3-d(GpTpG), (D) interstrand d(GG).

Despite the success of Pt^{II} anticancer drugs, there are drawbacks. One of these is that there can be severe side-effects associated with taking these drugs, including ototoxicity, neurotoxicity and nephrotoxicity.[38] Due to this, and the targeting of Schwann cells in the peripheral nervous system, dosage has to be limited.[39] Another problem with these drugs is that patients can develop resistance. This means that treatment becomes less effective, and dosage has to be increased to remain potent. This is thought to be due to reduced accumulation of the drugs in tumour tissue, and increased DNA repair, amongst other factors.[40]

1.2.2 Platinum^{IV} prodrugs

In an attempt to overcome the issues associated with Pt^{II} drugs, much research has been done into the use of Pt^{IV} prodrugs (Figure 1.9). Pt^{IV} complexes are generally more kinetically inert, and more thermally stable than Pt^{II} complexes.[18] Terming these compounds prodrugs comes from the fact that they need to be reduced in order to access the active anticancer compound. It is thought that the higher stability of these complexes may reduce the interactions with proteins and healthy tissues within the body, diminishing the unwanted side-effects and potentially opening up the opportunity for oral administration.

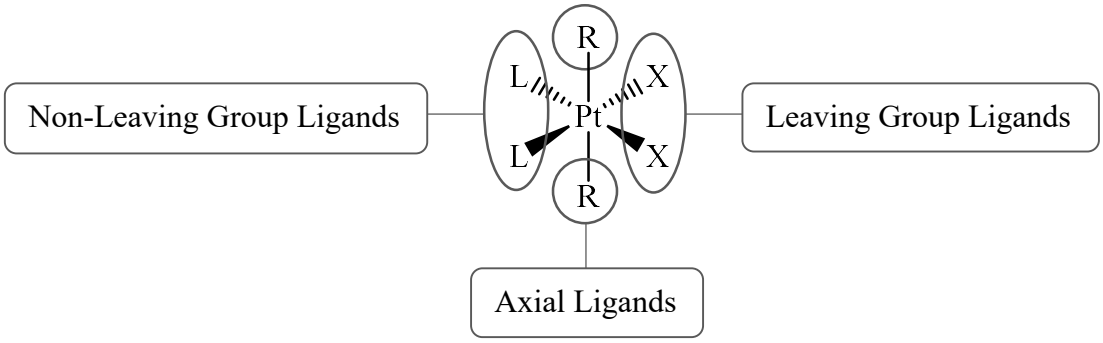

Figure 1.9 General structure of a Pt(IV) prodrug.[41]

The addition of two more ligands, allows for modification of the properties of the drug. Ligands with their own chemotherapeutic actions may give rise to multi-modal Pt based anticancer treatments.[42] By functionalising the axial positions, it may also be a way of improving the tumour targeting on the drugs, leading to a reduction in negative side-effects.[43] For example, estrogens have been bound to cisplatin constructs to improve targeting for breast cancers.[44]

Four Pt^{IV} drugs have entered clinical trials: iproplatin, tetraplatin, satraplatin, and LA-12 (Figure 1.10). Iproplatin was found to be less cytotoxic than cisplatin, and tetraplatin found to have too many side-effects, so both have been abandoned.[38,45] Satraplatin is currently in trials for use in combination with radiotherapy, and LA-12 is in phase I trials.[46,47]

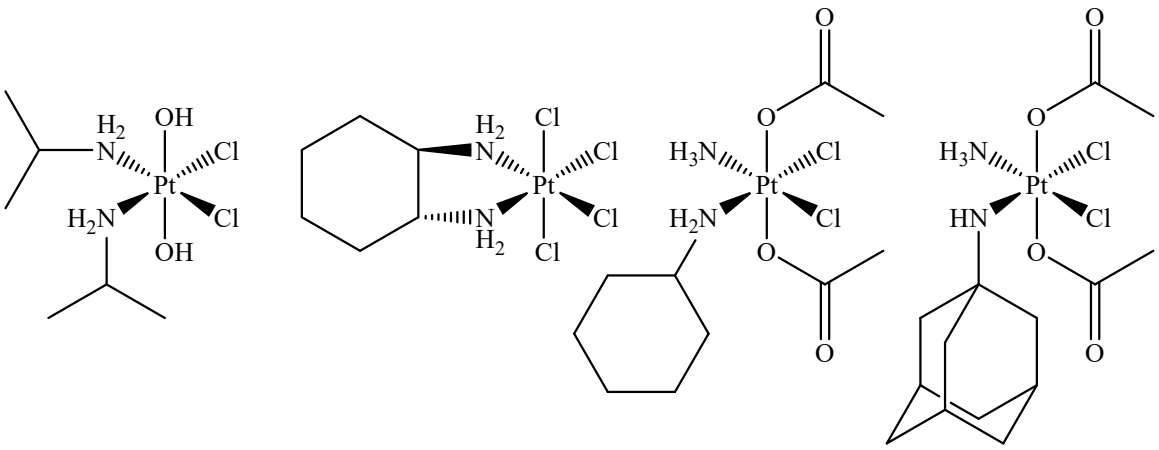

Figure 1.10 Structures of the four Pt^{IV} drugs that have entered clinical trials; iproplatin, tetraplatin, satraplatin, and LA-12.

It is thought that these Pt^{IV} complexes are reduced *in vivo* to the Pt^{II} analogue, and that the mechanism of action is then the same as shown in Figure 1.6. The reduction itself is believed to occur intracellularly by ascorbate and glutathione, as well as by proteins, within the cell.[48] How easily reducable Pt^{IV} prodrugs are depends on the nature of the coordinating ligands. These strongly influence the reduction potential. Generally, the more electronegative the ligands the smaller the reduction potential.[49]

1.2.3 Photoactivatable platinum^{IV} prodrugs

Light has been used as a means of treatment in medicine for centuries, with some of the most common modern examples being the use of blue-green light to treat jaundice, and the use of UVB to treat eczema.[50,51] Photodynamic therapy (PDT), developed by Lipson and Schwartz in the 1960s, advances on phototherapy by involving the administration of a photosensitizer[52,53]

Photosensitizers are molecules than can be activated by light.[54] In the presence of molecular oxygen, light activated photosensitizers will transfer energy to the oxygen, causing production of reactive oxygen species (ROS). In therapeutic application, the photosensitizer is allowed to build up within a tumour tissue, and it is the ROS that interact biochemically to cause damage and death to the surrounding tissue.[55]

Due to the rapid growth and poor vasculature of some tumours, the environment can be hypoxic, meaning that PDT can have limited efficacy.[56] One potential alternative to PDT is photoactivated chemotherapy (PACT). This is where photoactivatable complexes, that are stable in the dark, are irradiated in clinical conditions to obtain an active chemotherapeutic counterpart without the need for molecular oxygen.[57] There are several d-block metals which have been explored for photochemotherapy, including rhodium, gold and iron, however this thesis will focus on the use of platinum.[58,59]

The two common oxidation states of platinum both show photochemical properties.[60] Pt^{II} complexes frequently show luminescence following irradiation, whilst Pt^{IV} complexes exhibit photoreduction or dissociation.[61] Pt^{IV} complexes containing azide ligands display this behaviour, being able to be reduced to active Pt^{II} compounds by irradiation with short-wavelength light. The reduction is thought to occur due to induction of ligand to metal charge transfer (LMCT), which causes azide radicals to be expelled from the molecule (Figure 1.11).[62] For application in anticancer treatments, an inactive Pt^{IV} prodrug could be administered which may then enter cancerous cells. Irradiation with a clinically viable wavelength of light may then yield an active Pt^{II} drug, which could induce apoptosis in a similar way to cisplatin. Whether or not the azide radicals provide any clinical benefit themselves is not fully understood, but it is thought they quickly convert to produce nitrogen gas. The main benefit of

having photoactivatable drugs is that if they are non-toxic in the dark, there will be less off site activity and in turn reduced side effects from chemotherapy. The need for activation also means specific tumour sites can be targeted, with irradiation only at the necessary locations.

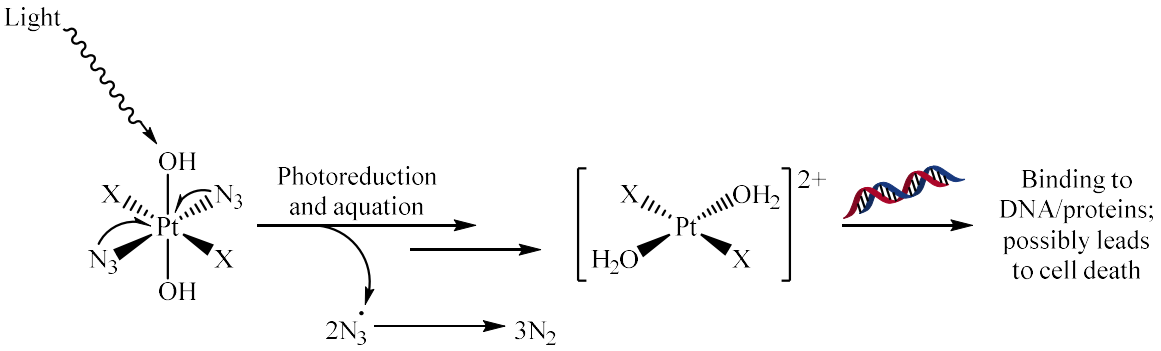

Figure 1.11 Proposed mechanism of photoactivation and anticancer activity of Pt^{IV} azide complexes (adapted from Farrer & Sadler).[63]

It has been shown that if these diazido complexes also contain amine ligands, changing the amines does not significantly alter the reduction potential of the Pt^{IV} compound. These ligands can therefore be varied to improve properties such as solubility or lipophilicity, without affecting the stability of the complexes.[64]

1.3 Liposomes

Liposomes are spherical vesicles formed from lipids which are arranged into bilayers surrounding an aqueous core (Figure 1.12).[65] The ability of these lipids to form bilayers arises from their amphiphilic nature. Liposomes were first discovered by Alec Bangham in 1964 by electron microscopy.[66]

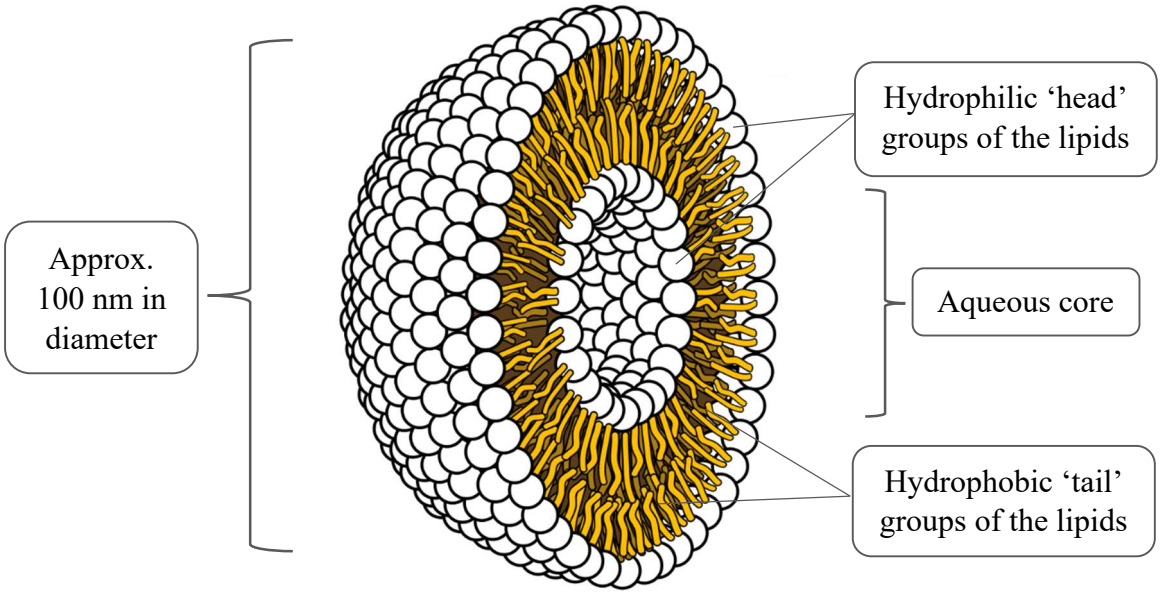

Figure 1.12 Schematic diagram of the cross-section of an unmodified liposome.

The aqueous core provides the possibility for containment of water-soluble drugs, with the volume of this core dictating how much drug can be 'loaded' into the liposomes. This is of interest as it has the potential to increase drug circulation times whilst reducing off target toxicity, and could also allow for targeted release.[67] Properties such as lipid composition and concentration can also be changed in order to alter the loading efficiency.[68] Drug loading can be achieved by active and passive methods (Figure 1.13). Passive loading is where the drug is incorporated into the liposomes during their formation, while active loading is where the drug is incorporated after the liposomes have been formed.[69]

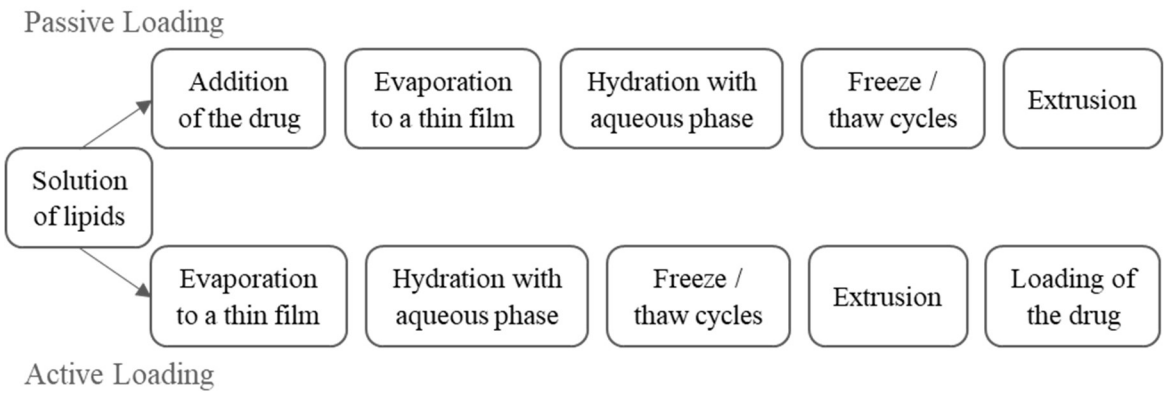

Figure 1.13 Flow diagram comparing active and passive loading of liposomes.

Active loading requires a gradient to be set up between the aqueous core of the liposome and the external medium, and also requires the drug to be ionisable. The drug is dissolved in the external medium in its neutral state, influxes across the liposomal membrane and can then be ionised inside the liposome. The drug becomes trapped due to formation of an insoluble salt with a counter ion.[70] Nichols and Deamer were the first to demonstrate this approach by using a pH gradient to load amphipathic amines into liposomes.[71] Barenholz then improved upon these methods by utilising pH and ion gradients created by salts of weak acids (e.g. acetate) or weak bases (e.g. ammonium).[72–74]

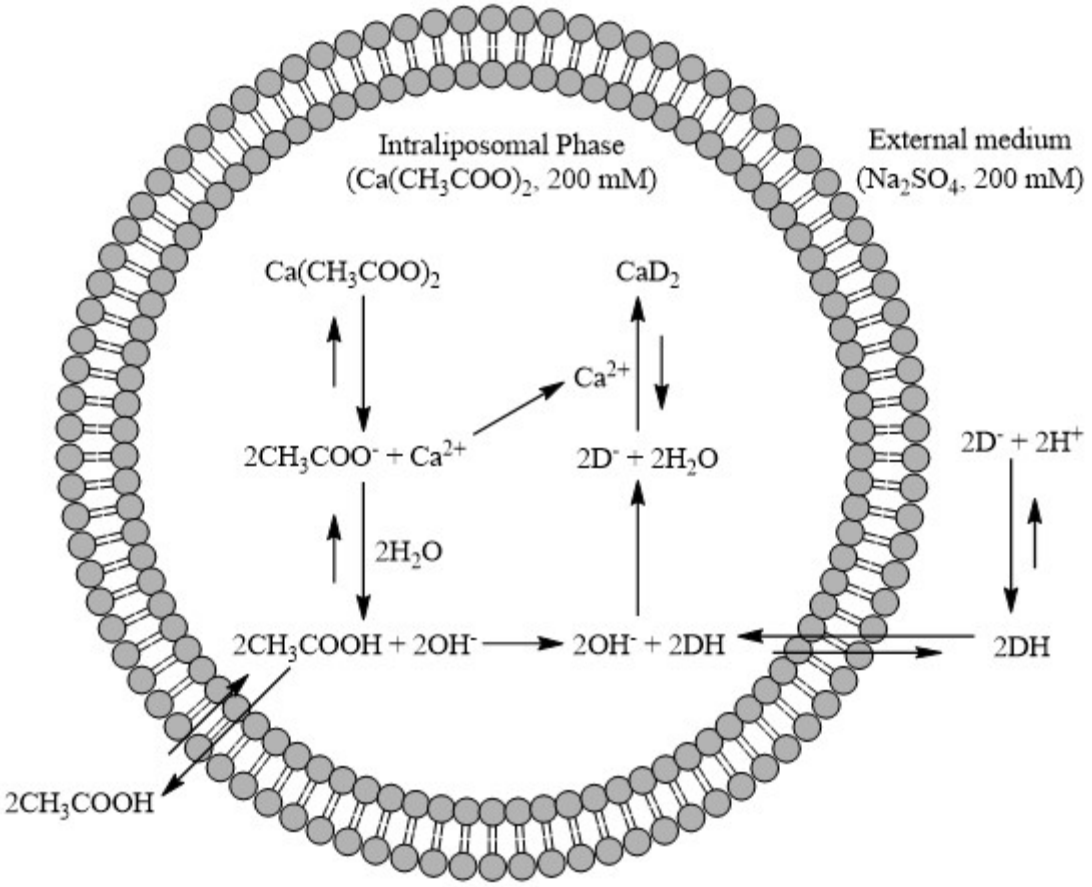

Figure 1.14 Diagram of calcium acetate active loading of a generic drug 'D' (adapted from Zucker et al.).[75]

The loading method used depends on the way in which the drug behaves. This thesis focuses on two gradient systems, a calcium acetate/sodium sulphate system, and an ammonium sulphate/sodium chloride system. These methods are outlined in Figures 1.14 and 1.15. The rationale behind the two methods is that if the drug behaves as an amphipathic weak acid then the calcium acetate method should yield the best loading, as the positively charged calcium ions bond to the negatively charged conjugate base of the drug to form a calcium salt that cannot pass back across the bilayer. This has been successfully demonstrated for nalidixic acid and pyranine.[74] If the drug behaves as an amphipathic weak base then the ammonium sulphate

method should yield the best loading, as the negatively charged sulphate ions interact with the drug to form a salt that becomes trapped in the intraliposomal matrix.[75]

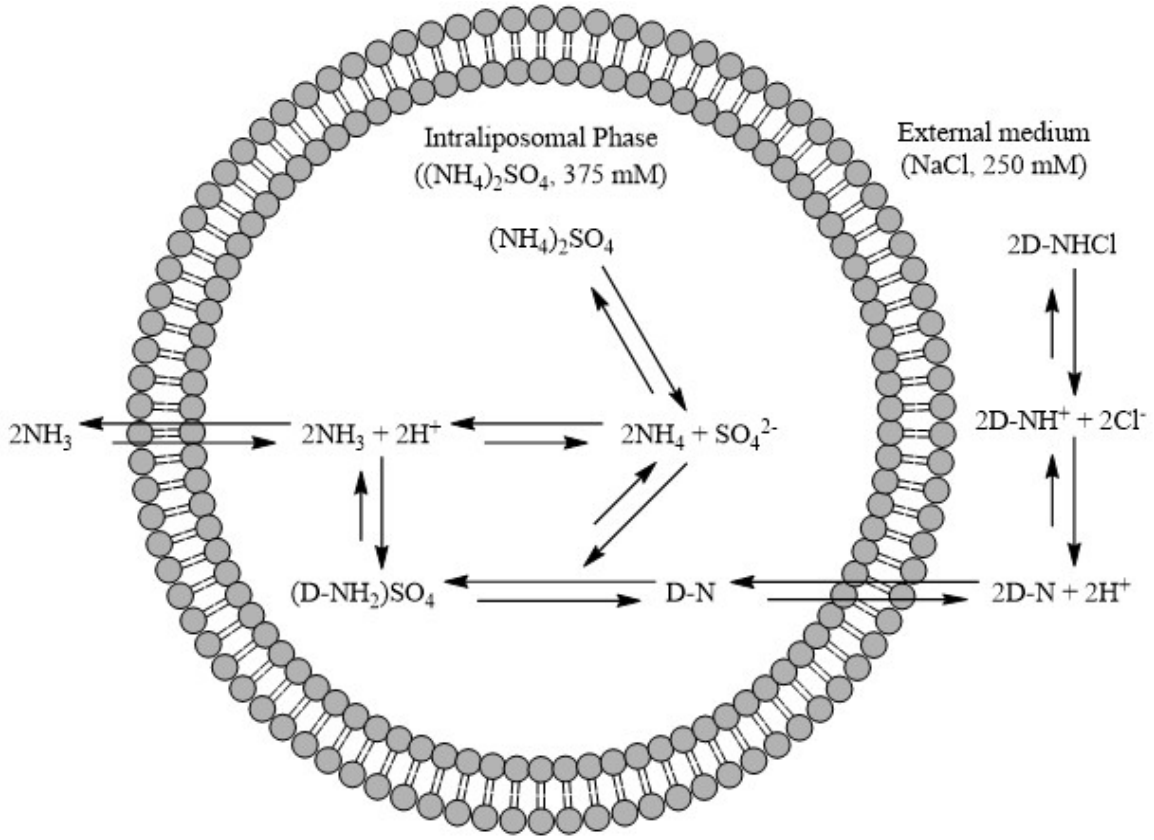

Figure 1.15 Diagram of ammonium sulphate active loading of generic drug 'D' (adapted from Zucker et al.).[75]

Zucker *et al.* developed a model based on analysis of other uptake experiments, which recommends optimised loading conditions based upon features of candidate molecules.[75] Encapsulation efficiencies have been shown to improve when freeze-thaw cycles are included in the liposome production method.[76] Transient holes are formed by the presence of ice crystals, which allow for better drug penetration and an increase in the intraliposomal volume.[77]

1.3.1 Passive and active delivery

The enhanced permeability and retention (EPR) effect describes the build up of nanoparticles smaller than 200 nm within tumour tissue.[78] This is a passive method of delivery that occurs due to the rapid growth of tumour cells, which leads to increased vasculature and poor lymphatic drainage in the surrounding area.[79] These factors should in theory allow leakage from the poorly formed capillaries into the intercellular space. In healthy tissue, the permeability of vasculature is limited to less than 1-2 nm in size, meaning that administered nanoparticles such as liposomes should not be able to leak into the intercellular space. All non-targeted nanocarrier systems rely upon this phenomenom for delivery, however the effect is strongly dependent upon the characteristics of the tumour tissue, and in clinical application limited extravasation is seen in solid tumours.[80,81] Subsequently, more active methods of delivery have been developed to improve tumour uptake.

To aid the targetsuing of treatment, it is preferable for the liposomes to either be targeted or to respond to a trigger in order to release any encapsulated drug at a specific location.[82] Tumour cells and their neighbouring healthy cells tend to show abnormal cell-surface proteins and receptors. Liposomes can be modified to have antibodies corresponding to these targets attached to the surfaces, allowing for improved accumulation at the tumour site.[83] They can also be made responsive to a range of triggers that will induce drug release, depending on the lipid composition.[81] Thermosensitive liposomes have shown successful release of doxorubicin in response to mild hyperthermia.[84] Liposomes responsive to *in vivo* environmental triggers have also been developed, with examples such as lactic acid secretion or glucose uptake of cancer cells causing drug release.[85] Additionally, ultrasound induced release has been investigated.[86]

1.3.2 Liposomes in medicine

Liposomes have many applications in medicine including use as drug delivery vehicles, response enhancers in vaccinations, and signal enhancers and carriers in medical diagnostics.[87] There are currently 15 approved liposomal drug formulations, with many more in clinical trials.[88,89]

Doxil® was the first FDA-approved liposomal cancer therapy, being approved in 1995.[90] It consists of liposomally encapsulated doxorubicin that is released by the EPR effect, passively targeting tumours. Doxorubicin is loaded into the liposomes using the active ammonium sulphate method, resulting in an intraliposomal drug concentration of 100 fold higher than the extraliposomal loading matrix. Once inside the liposomes the planar nature of the drug allows it to aggregate by stacking, however, it remains bioavailable.[91] Doxil® was developed to overcome the dose-limiting cardiotoxicity of doxorubicin, as when liposomally encapsulated the drug is no longer available in cardiac muscle cells.[92] More recently a liposomal formulation of vincristine has been approved for use in the US for treatment of acute lymphoblastic leukemia.[93]

Liposomes have already been used to encapsulate Pt^{II} drugs. Cisplatin was encapsulated in liposomes of the Doxil® formulation to produce STEALTH cisplatin (also called SPI-77). Although it showed increased accumulation in tumours compared to normal tissue, the cisplatin release was insufficient.[94,95] More recently, a different stealth liposomal cisplatin formulation (lipoplatin) has passed Phase II and III clinical trials in nonsmall lung cell carcinomas and pancreatic cancer. It shows 10-50 times greater accumulation in tumour tissues compared to healthy tissue, and exhibited a therapeutic effect similar to or greater than cisplatin when used in conjunction with paclitaxel.[96] It also shows negligible toxicity in healthy tissue.[97]

Lipoplatin has a drug to lipid ratio of 1:10 (w/w), and a cisplatin concentration of 3 mg mL^{-1}.[98] Oxaliplatin has also been encapsulated in liposomes in a formulation called Lipoxal. This has shown success, with lower toxicity and equivalent efficacy when compared to free oxaliplatin.[99]

Limitations of liposomal drug formulations have been observed in clinical trials, with a liposomal doxorubicin system (OLV-DOX) showing high leakage rates and removal by the reticuloendothelial system.[90] Reproducibility in the production of these formulations is also a complication, with batch-to-batch variability as high as 30%, thought to be a result of variation in nanoparticle size.[100]

1.3.3 Cross-linking

One of the main drawbacks of liposomal encapsulation for small-molecule drugs, is the poor drug retention. Research has shown that water soluble drugs loaded into the liposome core have a tendency to leak back out across the bilayer.[90] This leakage is undesirable as it would mean that, *in vivo*, not all of the loaded dose of drug is reaching the target site. The benefits of more targeted delivery include being able to keep dosages at a minimum, and reducing off-target activation which can cause detrimental side-effects. One possible method for improving the retention could be the inclusion of cross-linking within the lipid bilayer. This can be achieved by incorporating a diyne-containing lipid into the liposome composition.[101] Upon irradiation with UV-light (254 nm) the alkyne groups undergo photoinduced polymerization to form interstrand bonds. This cross-linking increases the rigidity of the liposome bilayer and has been shown to reduce leakage of various loaded compounds.[102,103]

1.4 Microbubbles

Microbubbles are gas filled spheres with a shell formed from lipids, polymers or proteins (Figure 1.16).[104] The diameter of the bubbles can range from 0.5 µm to 10 µm, similar to the size of red blood cells, which allows them to exhibit comparable rheology in the vasculature of the human body.[105]

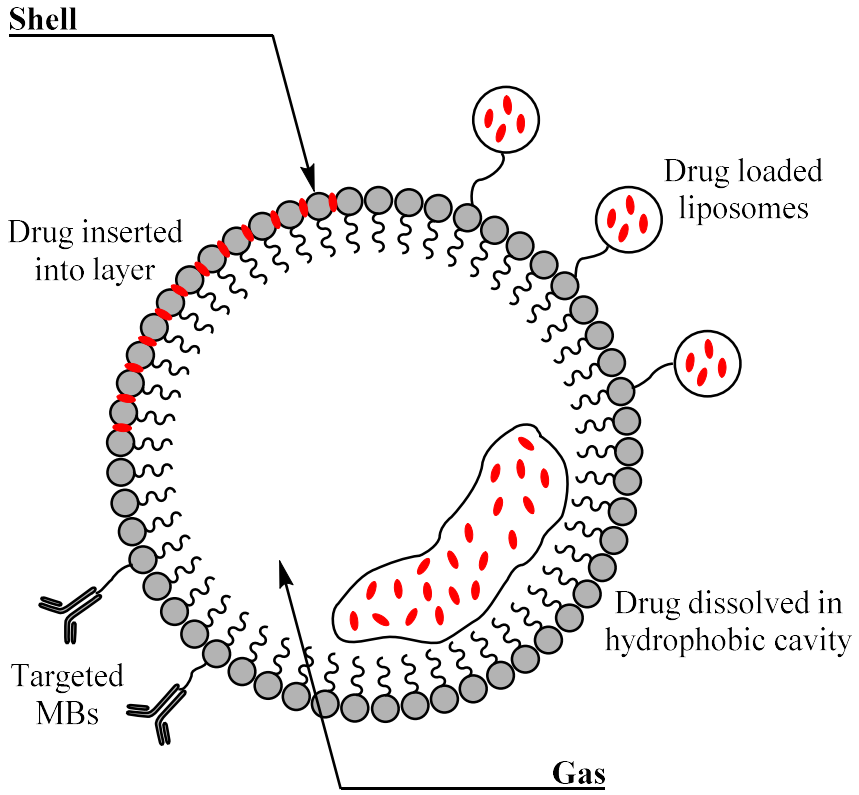

Figure 1.16 The various loading and targeting methods of microbubbles (adapted from Lammertink et al.).[106]

The gas core is utilised in the mechansm of drug delivery and drugs can be contained here, however because it is a poor solvent for carrying drugs, loading is generally achieved either within the shell or on the shell's surface. The gas core would also be naturally unstable in any aqueous media, so the shell is necessary in order to stabilise the core.[107] Microbubbles have been used clinically as contrast agents in medical imaging for several decades.[108]

1.4.1 Microbubbles and ultrasound

The use of ultrasound in medicine is already commonplace, with low level ultrasound applied for imaging and high level ultrasound used in procedures such as lithotripsy.[109] When microbubbles are exposed to ultrasound they exhibit oscillation (Figure 1.17). This is due to the gas core contracting during the compression phase of the pressure wave, and expanding during the rarefaction phase.[104] At low levels this ultrasound exposure will cause the bubbles to continually oscillate at or around their critical size, this is known as stable (non-intertial) cavitation. If the ultrasound exposure is high enough, the bubbles will oscillate until they reach their critical size, become unstable and violently collapse. This phenomenom is called inertial (transient) cavitation.[110]

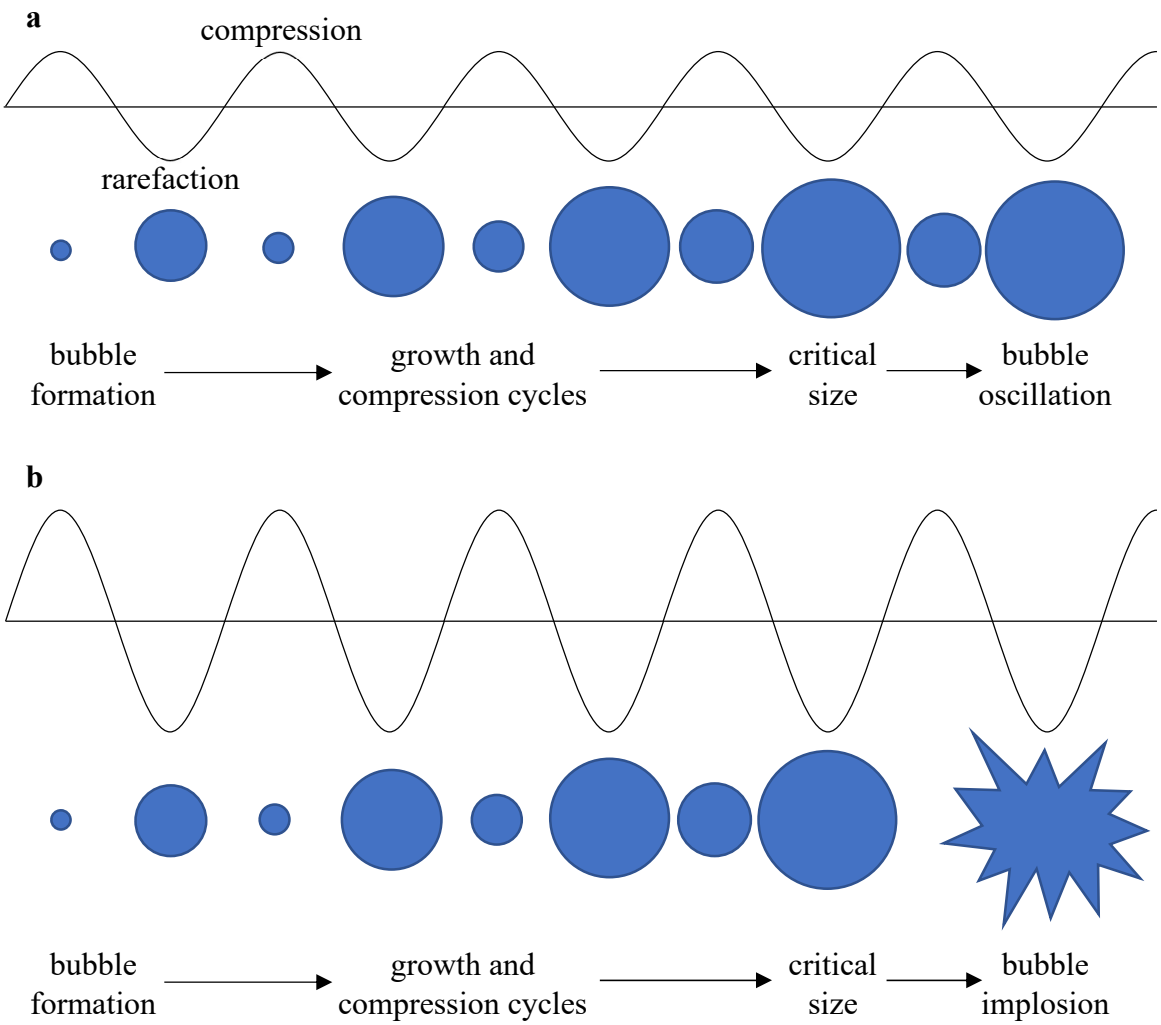

Figure 1.17 Schematic diagram showing microbubble cavitation; a – stable cavitation, b – inertial cavitation (adapted from Izadifar et al.).[110]

Inertial cavitation releases energy, which can present in the form of acoustic shock waves, temperature, pressure, and visible light.[111] Ultrasound induced caviation can assist in the delivery of drugs through a phenomenon known as sonoporation. This is when the oscillating or collapsing bubbles cause a temporary increase in the permeability of the surrounding tissues, such as blood vessel walls, cell membranes, or biological barries such as the BBB.[106] This can enhance the delivery of coadministered therapeutic molecules across these barriers and into the target location.[112] There are several methods via which sonoporation can occur in relation to biological membranes and barriers, such as vasculature walls or the BBB. These are outlined

in Figure 1.18.[113] Stable cavitation can lead to the formation of pores in an adjacent membrane via the push and pull effects felt from the expansion and contraction of microbubbles (b). Microstreaming can also occur from stable cavitation, in which circulatory motion is established in the liquid surrounding a vibrating bubble, and any cells in close viscinity experience shear stress (a).[82] This is thought to be the most influential factor involved in enhancing drug uptake. Inertial cavitation can cause sonoporation in two ways. Firstly, shock waves produced from collapsing bubbles exert high stress on cell membranes, which in turn causes membrane disruption and the formation of pores (c). Secondly, because the collapse of a bubble is asymmetrical, a jet of liquid directed towards a nearby surface can puncture the membrane and create pores (d).[114] Evidence for improved efficacy, when using microbubble-mediated ultrasound delivery, has been shown in the treatment of head and neck squamous cell carcinomas.[115]

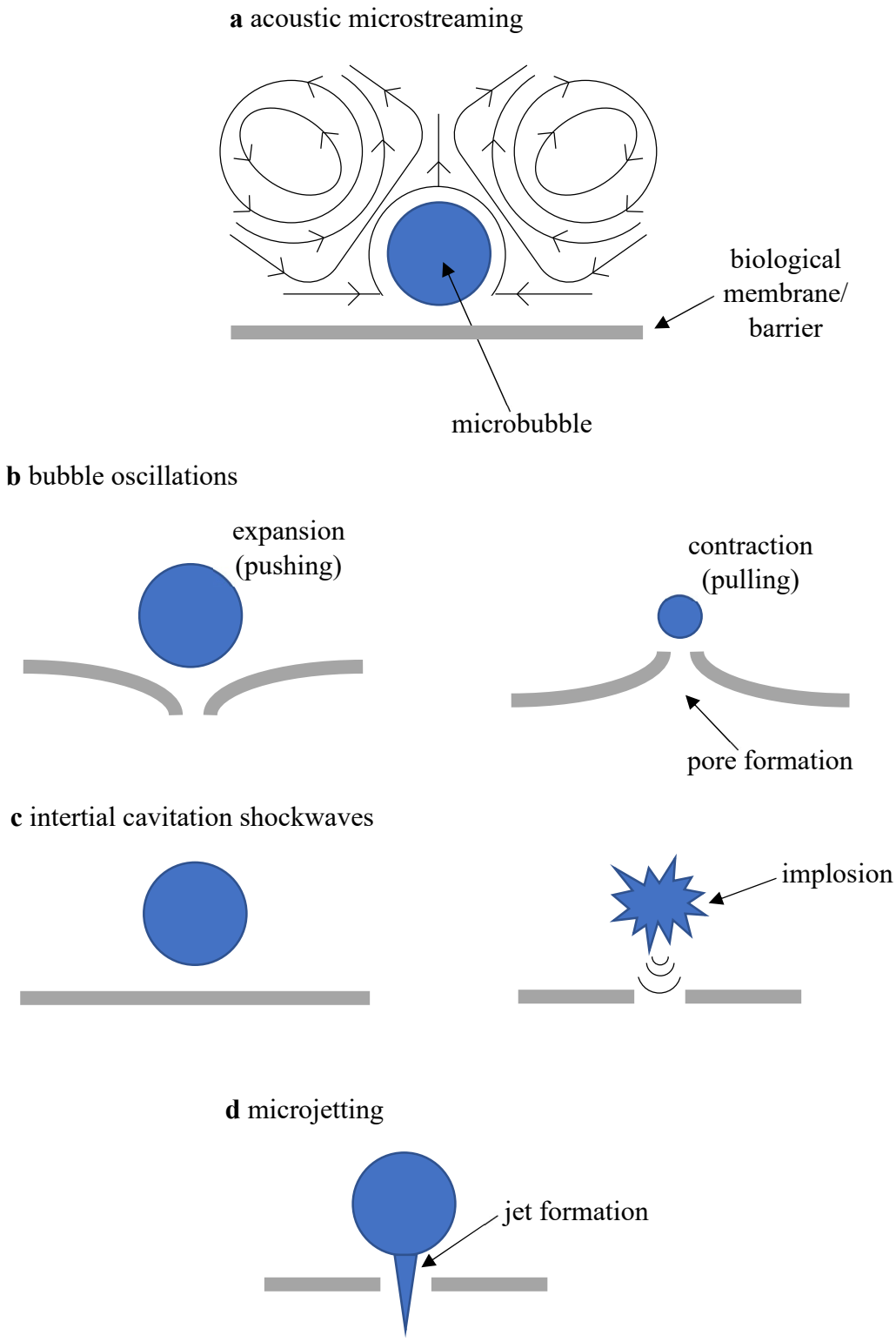

Figure 1.18 Methods of sonoporation; a – microstreaming, b – push and pull effects, c – shockwaves, d – microjet formation (adapted from Delalande et al.).[116]

As previously stated, inertial cavitation of microbubbles can release energy in the form of visible light. This is known as sonoluminescence.[117] This occurrence may be of interest as a method of activation for photosensitive drugs. Much research into this phenomenon has employed conditions that are not relevant to practical clinical application.[118–120] However, more recent studies have shown direct evidence for activation of a photosensitive drug by sonoluminescence under clinically viable conditions.[121]

1.4.2 Liposome conjugated systems

Microbubbles can be used as a carrier system for drug loaded liposomes (Figure 1.16). These conjugated systems can be exploited for ultrasound targeted release by focusing the ultrasound field at the target site, destroying the bubbles in the vicinity, and releasing the drug primarily to the desired destination.[122] It is thought that microbubble cavitation may be crucial in optimising the ultrasound mediated activity of liposomes, and improving cellular uptake.[109] Although microbubbles and liposomes could be coadministered without conjugation, it is unlikely to yield the proximity and concentrations required for high membrane disruption and dose delivery.[123] Doxorubicin loaded liposomes conjugated to microbubbles have also shown drug release when exposed to ultrasound.[124] *In vitro* studies of this microbubble-liposome system found an increase in cell death compared to use of only the liposomes with ultrasound.[125]

The ability to functionalise the outer shells of both liposomes and microbubbles means they can easily be bound together. There are several methods available for the conjugation, with previous research investigating biotin-avidin and malemide-thiol linkages. Although biotin-avidin coupling forms strong bonds, this system cannot be clinically applied due to the immune

response it invokes in humans.[126,127] The malemide-thiol bond has been explored separately for targeted immunoliposomes and microbubbles.[128,129] However, due to the presence of several reactive functionalities in the malemide-thiol system, it shows poor selectivity. More recently, conjugating microbubbles containing a dibenzocyclooctyne (DBCO) functionalized lipid to azide functionalised liposomes using strain promoted azide-alkyne cycloaddition (SPAAC), has been explored.[130,131] This method of click chemistry was developed by Agard *et al*. as an alternative to copper catalysed click reactions, which are incompatible with biological application due to the cytotoxicity of copper.[132,133] In this example the benzene rings on the cyclooctyne are electron-withdrawing, and therefore destabilize the alkyne. This is the driving force behind the reaction, as the ring strain is high in the cycloalkyne, and so reacts with the azide via a [3+2] cycloaddition to produce a less strained product.

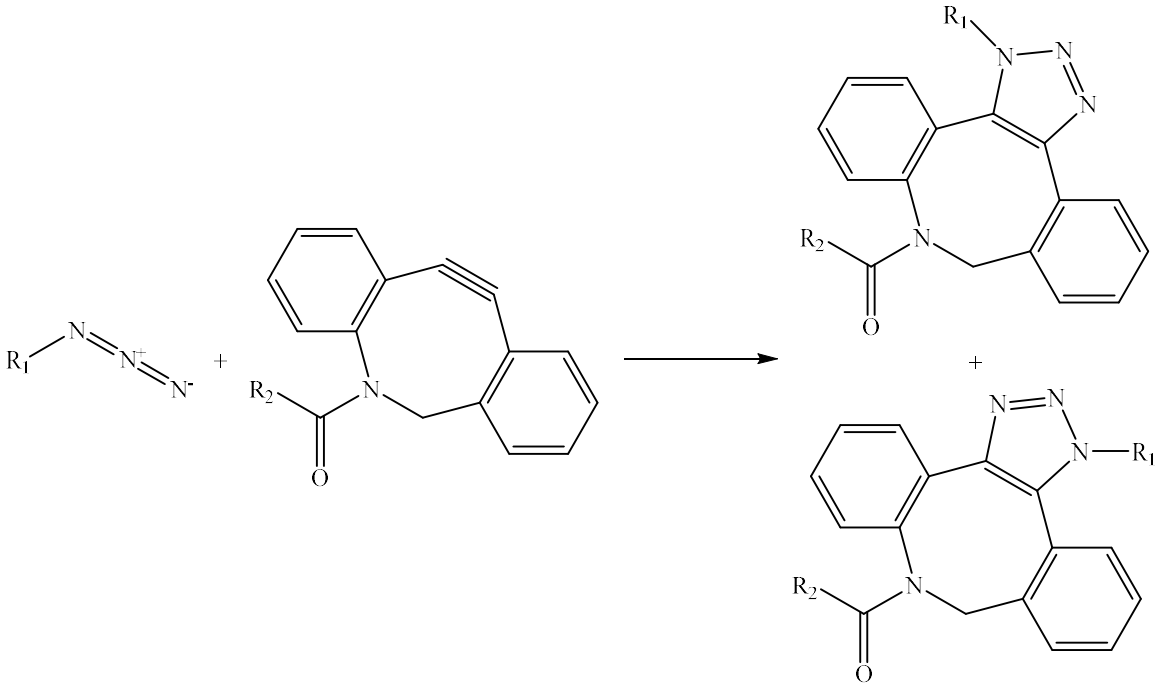

Figure 1.19 Diagram showing the regioisomer products of a SPAAC reaction between an azide functional group and a DBCO functional group.

1.5 Project aims

This work explores the synthesis of novel azide-containing photoactivatable Pt^{IV} prodrugs, and how varying the nitrogen coordinating ligands in the other equtorial positions alters the pK_a and photochemical properties of the complexes. The use of liposomes as a method of drug encapsulation for delivery will also be investigated, with a focus on identifying the best loading method for a given compound, and improving the retention time for small molecule Pt-containing drugs. Finally, this work will look at how microbubbles could be used in conjunction with drug loaded liposomes to improve uptake in tumours, and whether sonoluminescence is viable for the reduction of photoactivatable Pt^{IV} prodrugs.

The rationale for this work is to assess the individual components of a potential treatment sytsem for DIPG. The proposed model would involve administering a photoactivatable Pt^{IV} drug, encapsulated in liposomes which are themselves conjugated to the surface of microbubbles. Ultrasound focused at the BBB would lead to cavitation of any microbubbles in the region, which would in turn temporarily disrupt the barrier by sonoporation and activate the drug by sonoluminescence. This would allow for the chemotherapeutic Pt^{II} counterpart to enter tumour cells within the pons to exert cytotoxic effects.

1.6 References

1 E. Panditharatna, K. Yaeger, L. B. Kilburn, R. J. Packer and J. Nazarian, *Cancer Genet.*, 2015, **208**, 367–373.

2 K. M. Schroeder, C. M. Hoeman and O. J. Becher, *Pediatr. Res.*, 2014, **75**, 205–209.

3 K. E. Warren, *Front. Oncol.*, 2012, **2**, 1–9.

4 R. Kebudi and F. B. Cakir, *Pediatr. Drugs*, 2013, **15**, 351–362.

5 N. J. Robison and M. W. Kieran, *J. Neurooncol.*, 2014, **119**, 7–15.

6 M. H. A. Jansen, D. G. van Vuurden, W. P. Vandertop and G. J. L. Kaspers, *Cancer Treat. Rev.*, 2012, **38**, 27–35.

7 M. Filbin and M. Monje, *Nat. Med.*, 2019, **25**, 367–376.

8 C. Jones, M. A. Karajannis, D. T. W. Jones, M. W. Kieran, M. Monje, S. J. Baker, O. J. Becher, Y. J. Cho, N. Gupta, C. Hawkins, D. Hargrave, D. A. Haas-Kogan, N. Jabado, X. N. Li, S. Mueller, T. Nicolaides, R. J. Packer, A. I. Persson, J. J. Phillips, E. F. Simonds, J. M. Stafford, Y. Tang, S. M. Pfister and W. A. Weiss, *Neuro. Oncol.*, 2017, **19**, 153–161.

9 R. K. Mathew and J. T. Rutka, *J. Korean Neurosurg. Soc.*, 2018, **61**, 343–351.

10 H. Kadry, B. Noorani and L. Cucullo, *Fluids Barriers CNS*.

11 E. E. Konofagou, Y. S. Tung, J. Choi, T. Deffieux, B. Baseri and F. Vlachos, *Curr. Pharm. Biotechnol.*, 2012, **13**, 1332–1345.

12 B. M. Still, P. G. A. Kumar, J. R. Aldrich-Wright and W. S. Price, *Chem. Soc. Rev.*, 2007, **36**, 665–686.

13 N. N. Greenwood and A. Earnshaw, *Chemistry of the Elements*, Oxford, UK, 2nd edn., 1997.

14 I. M. Ismail, S. J. S. Kerrison and P. J. Sadler, *Polyhedron*, 1982, **1**, 57–59.

15 J. Y. Lallemand, J. Soulié and J. C. Chottard, *J. Chem. Soc. Chem. Commun.*, 1980, **1352**, 436–438.

16 S. Dasari and P. Bernard Tchounwou, *Eur. J. Pharmacol.*, 2014, **740**, 364–378.

17 B. Rosenberg, L. Van Camp and T. Krigas, *Nature*, 1965, **205**, 698–699.

18 T. C. Johnstone, K. Suntharalingam and S. J. Lippard, *Phil. Trans. R. Soc. A*, 2015, **373**, 1–12.

19 D. Gibson, *Dalt. Trans.*, 2016, **45**, 12983–12991.

20 M. J. Cleare and J. D. Hoeschele, *Bioinorg. Chem.*, 1973, **2**, 187–210.

21 Y. Zhao, J. P. May, I. W. Chen, E. Undzys and S. D. Li, *Pharm. Res.*, 2015, **32**, 3261–3268.

22 C. A. Puckett, R. J. Ernst and J. K. Barton, *Dalt. Trans.*, 2010, **39**, 1159–1170.

23 D. P. Gately and S. B. Howell, *Br. J. Cancer*, 1993, 1171–1176.

24 D. Wang and S. J. Lippard, *Nat. Rev. Drug Discov.*, 2005, **4**, 307–320.

25 J. W. Reishus and D. S. MartinJr, *J. Am. Chem. Soc.*, 1961, **83**, 2457–2462.

26 G. L. Cohen, W. R. Bauer, J. K. Barton and S. J. Lippard, *Science (80-.).*, 1979, **203**, 1014–1016.

27 E. R. Jamieson and S. J. Lippard, *Chem. Rev.*, 1999, **99**, 2467–2498.

28 A. M. Fichtinger-Schepman, J. L. van der Veer, J. H. den Hartog, P. H. Lohman and J. Reedijk, *Biochemistry*, 1985, **24**, 707–713.

29 D. P. Bancroft, C. A. Lepre and S. J. Lippard, *J. Am. Chem. Soc.*, 1990, **112**, 6860–6871.

30 L. Kelland, *Nat. Rev. Cancer*, 2007, **7**, 573–584.

31 J. M. Malinge, M. J. Giraud-Panis and M. Leng, *J. Inorg. Biochem.*, 1999, **77**, 23–29.

32 M. Kartalou and J. M. Essigmann, *Mutat. Res. - Fundam. Mol. Mech. Mutagen.*, 2001, **478**, 1–21.

33 M. Frezza, S. Hindo, D. Chen, A. Davenport, S. Schmitt, D. Tomco and Q. Ping Dou, *Curr. Pharm. Des.*, 2010, **16**, 1813–1825.

34 U. Jungwirth, C. R. Kowol, B. K. Keppler, C. G. Hartinger, W. Berger and P. Heffeter, *Antioxid Redox Signal*, 2011, **15**, 1085–1127.

35 L. A. Rashed, R. M. Hashem and H. M. Soliman, *Biomed. Pharmacother.*, 2011, **65**, 474–480.

36 K. J. Cullen, Z. Yang, L. Schumaker and Z. Guo, *J. Bioenerg. Biomembr.*, 2007, **39**, 43–50.

37 Z. Yang, L. M. Schumaker, M. J. Egorin, E. G. Zuhowski, Z. Quo and K. J. Cullen, *Clin. Cancer Res.*, 2006, **12**, 5817–5825.

38 N. J. Wheate, S. Walker, G. E. Craig and R. Oun, *Dalt. Trans.*, 2010, **39**, 8113–8127.

39 S. Imai, M. Koyanagi, Z. Azimi, Y. Nakazato, M. Matsumoto, T. Ogihara, A. Yonezawa, T. Omura, S. Nakagawa, S. Wakatsuki, T. Araki, S. Kaneko, T. Nakagawa and K. Matsubara, *Sci. Rep.*, 2017, **7**, 1–14.

40 D. W. Shen, L. M. Pouliot, M. D. Hall and M. M. Gottesman, *Pharmacol. Rev.*, 2012, **64**, 706–721.

41 A. M. Breglio, A. E. Rusheen, E. D. Shide, K. A. Fernandez, K. K. Spielbauer, K. M. McLachlin, M. D. Hall, L. Amable and L. L. Cunningham, *Nat. Commun.*, , DOI:10.1038/s41467-017-01837-1.

42 Justin J. Wilson and Stephen J. Lippard, *Chem. Rev.*, 2014, **114**, 4470–4495.

43 S. Dilruba and G. V. Kalayda, *Cancer Chemother. Pharmacol.*, 2016, **77**, 1103–1124.

44 I. Ott and R. Gust, *Anticancer. Agents Med. Chem.*, 2007, **7**, 95–110.

45 R. J. Schilder, F. P. LaCreta, R. P. Perez, S. W. Johnson, J. M. Brennan, A. Rogatko, S. Nash, C. McAleer, T. C. Hamilton, D. Roby, R. C. Young, R. F. Ozols and P. J. O'Dwyer, *Cancer Res.*, 1994, **54**, 709–717.

46 Q. Mi, S. Shu, C. Yang, C. Gao, X. Zhang, X. Luo, C. Bao, X. Zhang and J. Niu, *Int. J. Med. Physics, Clin. Eng. Radiat. Oncol.*, 2018, **07**, 231–247.

47 A. M. Pizarro and P. J. Sadler, *Biochimie*, 2009, **91**, 1198–1211.

48 E. Wexselblatt and D. Gibson, *J. Inorg. Biochem.*, 2012, **117**, 220–229.

49 N. A. Kratochwil and P. J. Bednarski, *Arch. Pharm. (Weinheim).*, 1999, **332**, 279–285.

50 P. Woodgate and L. A. Jardine, *BMJ Clin. Evid.*

51 A. Patrizi, B. Raone and G. M. Ravaioli, *Adv. Exp. Med. Biol.*, 2017, **996**, 319–331.

52 R. L. Lipson, E. J. Baldes and A. M. Olsen, *J. Thorac. Cardiovasc. Surg.*, 1961, **42**, 623–629.

53 R. L. Lipson, E. J. Baldes and A. M. Olsen, *J. Natl. Cancer Inst.*, 1961, **26**, 1–11.

54 L. F. de Freitas and M. R. Hamblin, in *Nanomaterials in Antimicrobial Therapy*, ed. A. M. Grumezescu, William Andrew Publishing, 2016, pp. 1–27.

55 J. H. Correia, A. Rodrigues, J, S. Pimenta, T. Dong and Z. Yang, *Pharmaceutics*, 2021, **13**, 1332.

56 N. J. Farrer, L. Salassa and P. J. Sadler, *Dalt. Trans.*, 2009, 10660–10669.

57 S. Bonnet, *Dalt. Trans.*, 2018, **47**, 10330–10343.

58 B. Desoize, *Anticancer Res.*, 2004, **24**, 1529–1544.

59 V. Balzani and S. Campagna, *Photochemistry and Photophysics of Coordination Compound I & II*, Springer-Verlag, Berlin Heidelberg, 1st edn., 2007.

60 P. J. Bednarski, F. S. Mackay and P. J. Sadler, *Anticancer. Agents Med. Chem.*, 2008, **7**, 75–93.

61 C. J. Adams, N. Fey, Z. A. Harrison, I. V. Sazanovish, M. Towrie and J. A. Weinstein, *Inorg. Chem.*, 2008, **47**, 8242–8257.

62 M. D. Hall, R. Dolman and T. W. Hambley, *Met. Ions Biol. Syst.*, 2004, **9**, 297–322.

63 N. J. Farrer and P. J. Sadler, *Aust. J. Chem.*, 2008, **61**, 669–674.

64 M. D. Hall and T. W. Hambley, *Coord. Chem. Rev.*, 2002, **232**, 49–67.

65 B. S. Pattni, V. V. Chupin and V. P. Torchilin, *Chem. Rev.*, 2015, **115**, 10938–10966.

66 A. D. Bangham and R. W. Horne, *J. Mol. Biol.*, 1964, **8**, 660–668.

67 T. M. Allen and P. R. Cullis, *Adv. Drug Deliv. Rev.*, 2013, **65**, 36–48.

68 J. O. Eloy, M. Claro de Souza, R. Petrilli, J. P. A. Barcellos, R. J. Lee and J. M. Marchetti, *Colloids Surfaces B Biointerfaces*, 2014, **123**, 345–363.

69 A. Akbarzadeh, R. Rezaei-sadabady, S. Davaran, S. W. Joo and N. Zarghami, *Nano. Rev.*, 2013, **8**, 1–9.

70 K. Parak, *J. Control. Release*, 2017, **252**, 125.

71 J. W. Nichols and D. W. Deamer, *BBA - Biomembr.*, 1976, **455**, 269–271.

72 Y. Barenholz, *Curr. Opin. Colloid Interface Sci.*, 2001, **6**, 66–77.

73 D. D. Lasic, B. Čeh, M. C. A. Stuart, L. Guo, P. M. Frederik and Y. Barenholz, *BBA - Biomembr.*, 1995, **1239**, 145–156.

74 S. Clerc and Y. Barenholz, *BBA - Biomembr.*, 1995, **1240**, 257–265.

75 D. Zucker, D. Marcus, Y. Barenholz and A. Goldblum, *J. Control. Release*, 2009, **139**, 73–80.

76 J. Gubernator, *Expert Opin. Drug Deliv.*, 2011, **8**, 565–580.

77 L. D. Mayer, M. J. Hope, P. R. Cullis and A. S. Janoff, *Biochim. Biophys. Acta*, 1985, **817**, 193–196.

78 J. Wu, *J. Pers. Med.*, 2021, **11**, 1–8.

79 G. T. Noble, J. F. Stefanick, J. D. Ashley, T. Kiziltepe and B. Bilgicer, *Trends Biotechnol.*, 2014, **32**, 32–45.

80 K. J. Harrington, S. Mohammadtaghi, P. S. Uster, D. Glass, A. M. Peters, R. G. Vile and J. S. Stewart, *Clin. Cancer Res.*, 2001, **7**, 243–254.

81 R. J. Browning, P. J. T. Reardon, M. Parhizkar, R. B. Pedley, M. Edirisinghe, J. C. Knowles and E. Stride, *ACS Nano*, 2017, **11**, 8560–8578.

82 S. Mo, C. C. Coussios, L. Seymour and R. Carlisle, *Expert Opin. Drug Deliv.*, 2012, **9**, 1525–1538.

83 H. Nanoparticles, X. Peng, Y. Wang, D. Huang, Y. Wang, H. Juc, Z. Chen, M. B. Spewak, H. Mao, X. Wang, Y. Wang, G. Chen, S. Nie and D. M. Shin, *ACS Nano.*, 2011, **5**, 9480–9493.

84 L. Li, T. L. M. Ten Hagen, M. Hossann, R. Süss, G. C. Van Rhoon, A. M. M.

Eggermont, D. Haemmerich and G. A. Koning, *J. Control. Release*, 2013, **168**, 142–150.

85 B. Jiang, *Genes Dis.*, 2017, **4**, 25–27.

86 P. C. Lyon, L. F. Griffiths, J. Lee, D. Chung, R. Carlisle, F. Wu, M. R. Middleton, F. V. Gleeson and C. C. Coussios, *J. Ther. Ultrasound*, 2017, **5**, 1–8.

87 H. Daraee, A. Etemadi, M. Kouhi, S. Alimirzalu and A. Akbarzadeh, *Artif. Cells, Nanomedicine Biotechnol.*, 2016, **44**, 381–391.

88 U. Bulbake, S. Doppalapudi, N. Kommineni and W. Khan, *Pharmaceutics*, 2017, **9**, 1–33.

89 E. Beltrán-Gracia, A. López-Camacho, I. Higuera-Ciapara, J. B. Velázquez-Fernández and A. A. Vallejo-Cardona, *Nanomedicine review: Clinical developments in liposomal applications*, Springer Vienna, 2019, vol. 10.

90 Y. Barenholz, *J. Control. Release*, 2012, **160**, 117–134.

91 E. M. Bolotin, R. Cohen, L. K. Bar, N. Emanuel, S. Ninio, Y. Barenholz and D. D. Lasic, *J. Liposome Res.*, 1994, **4**, 455–479.

92 B. Overmoyer, P. Silverman, L. W. Holder, D. Tripathy and I. C. Henderson, *Clin. Breast Cancer*, 2005, **6**, 150–157.

93 P. Pathak, R. Hess and M. A. Weiss, *Ther. Adv. Hematol.*, 2014, **5**, 18–24.

94 E. S. Kim, C. Lu, F. R. Khuri, M. Tonda, B. S. Glisson, D. Liu, M. Jung, W. K. Hong and R. S. Herbst, *Lung Cancer*, 2001, **34**, 427–432.

95 T. Peleg-Shulman, D. Gibson, R. Cohen, R. Abra and Y. Barenholz, *Biochim. Biophys. Acta - Biomembr.*, 2001, **1510**, 278–291.

96 G. P. Stathopoulos, D. Antoniou, J. Dimitroulis, J. Stathopoulos, K. Marosis and P. Michalopoulou, *Cancer Chemother. Pharmacol.*, 2011, **68**, 945–950.

97 G. P. Stathopoulos, *Anticancer. Drugs*, 2010, **21**, 732–736.

98 T. Boulikas, *Expert Opin. Investig. Drugs*, 2009, **18**, 1–22.

99 G. P. Stathopoulos, T. Boulikas, A. Kourvetaris and J. Stathopoulos, *Anticancer Res.*, 2006, **26**, 1489–1493.

100 N. J. Wheate, *Nanomedicine*, 2012, **7**, 1285–1287.

101 C. E. Smith and H. Kong, *Langmuir*, 2014, **30**, 3697–3704.

102 K.-I. Joo, L. Xiao, S. Liu, Y. Liu, C.-L. Lee, P. S. Conti, M. K. Wong, Z. Li and P.

Wang, *Biomaterials*, 2013, **34**, 3098–3109.

103 N. T. Thet, W. D. Jamieson, M. Laabei, J. D. Mercer-Chalmers and A. T. A. Jenkins, *J. Phys. Chem. B*, 2014, **118**, 5418–5427.

104 S. Shashank and M. Borden, *Bubble Sci. Eng. Technol.*, 2009, **1**, 3–17.

105 J. R. Lindner, J. Song, A. R. Jayaweera, J. Sklenar and S. Kaul, *J. Am. Soc. Echocardiogr.*, 2002, **15**, 396–403.

106 B. H. A. Lammertink, C. Bos, R. Deckers, G. Storm, C. T. W. Moonen and J. M. Escoffre, *Front. Pharmacol.*, 2015, **6**, 1–17.

107 P. S. Epstein and M. S. Plesset, *J. Chem. Phys.*, 1950, **18**, 1505–1509.

108 P. Frinking, T. Segers, Y. Luan and F. Tranquart, *Ultrasound Med. Biol.*, 2020, **46**, 892–908.

109 A. Schroeder, J. Kost and Y. Barenholz, *Chem. Phys. Lipids*, 2009, **162**, 1–16.

110 Z. Izadifar, P. Babyn and D. Chapman, *J. Med. Biol. Eng.*, 2019, **39**, 259–276.

111 Y. S. Tung, J. J. Choi, B. Baseri and E. E. Konofagou, *Ultrasound Med. Biol.*, 2010, **36**, 840–852.

112 I. Lentacker, I. De Cock, R. Deckers, S. C. De Smedt and C. T. W. Moonen, *Adv. Drug Deliv. Rev.*, 2014, **72**, 49–64.

113 E. Stride and C. Coussios, *Nat. Rev. Phys.*, 2019, **1**, 495–509.

114 Z. Fan, R. E. Kumon and C. X. Deng, *Ther. Deliv.*, 2014, **5**, 467–486.

115 C. H. Heath, A. Sorace, J. Knowles, E. Rosenthal and K. Hoyt, *Otolaryngol. - Head Neck Surg. (United States)*, 2012, **146**, 938–945.

116 A. Delalande, S. Kotopoulis, T. Rovers, C. Pichon and M. Postema, *Bubble Sci. Eng. Technol.*, 2011, **3**, 3–12.

117 K. S. Suslick, S. J. Doktycz and E. B. Flint, *Ultrasonics*, 1990, **28**, 280–290.

118 W. B. McNamara, Y. T. Didenko and K. S. Suslick, *Nature*, 1999, **401**, 772–775.

119 M. P. Brenner, S. Hilgenfeldt and D. Lohse, *Rev. Mod. Phys.*, 2002, **74**, 425–460.

120 D. L. Miller, N. B. Smith, M. R. Bailey, G. J. Czarnota, K. Hynynen and I. R. S. Makin, *J. Ultrasound Med.*, 2012, **31**, 623–634.

121 E. Beguin, S. Shrivastava, N. V. Dezhkunov, A. P. Mchale, J. F. Callan and E. Stride, *ACS Appl. Mater. Interfaces*, 2019, **11**, 19913–19919.

122 A. L. Klibanov, T. I. Shevchenko, B. I. Raju, R. Seip and C. T. Chin, *J. Control Release*, 2010, **148**, 13–17.

123 S. Ibsen, M. Benchimol, D. Simberg, C. Schutt, J. Steiner and S. Esener, *J. Chem. Soc., Dalt. Trans.*, 2011, **155**, 358–366.

124 B. Geers, I. Lentacker, N. N. Sanders, J. Demeester, S. Meairs and S. C. De Smedt, *J. Control. Release*, 2011, **152**, 249–256.

125 I. Lentacker, B. Geers, J. Demeester, S. C. De Smedt and N. N. Sanders, *Mol. Ther.*, 2010, **18**, 101–108.

126 B. Geers, H. Dewitte, S. C. De Smedt and I. Lentacker, *J. Control. Release*, 2012, **164**, 248–255.

127 S. Bozzini, S. Gratton, A. Lisini and A. Risaliti, *Tetrahedron*, 1983, **39**, 3409–3413.

128 C. Chuit, H. Feltun, C. Frajerman, G. Roussi and G. Swierczewski, *J. Organomet. Chem.*, 1977, **127**, 371–384.

129 J. S. M. Yeh, C. A. Sennoga, E. McConnell, R. Eckersley, M. X. Tang, S. Nourshargh, J. M. Seddon, D. O. Haskard and P. Nihoyannopoulos, *PLoS One*, 2015, **10**, 1–23.

130 S. Alam, D. S. Alves, S. A. Whitehead, A. M. Bayer, C. D. McNitt, V. V. Popik, F. N. Barrera and M. D. Best, *Bioconjug. Chem.*, 2015, **26**, 1021–1031.

131 R. Browning, N. Thomas, L. K. Marsh, L. R. Tear, J. Owen, E. Stride and N. J. Farrer, *ChemistryOpen*, 2021, 1170–1176.

132 N. J. Agard, J. A. Prescher and C. R. Bertozzi, *J. Am. Chem. Soc.*, 2004, **126**, 15046–15047.

133 R. Huisgen, *Angew. Chemie Int.*, 1963, **2**, 565–632.

Chapter 2 Photoactivatable Platinum Complexes

2.1 Introduction

Various platinum complexes with different functionalisations were synthesised, either as precursors for further reactions or as the final products themselves. All syntheses followed the general route of formulating a Pt^{II} complex from K_2PtCl_4, with subsequent oxidation to the respective Pt^{IV} complexes using H_2O_2.

The ability of Pt^{II} complexes to undergo associative ligand substitution reactions was used to preferentially produce either the *cis*- or *trans*-isomers of the synthesised complexes. During this associative ligand substitution, the incoming ligand bonds to the Pt centre in an equatorial position to form a transient five-coordinate intermediate. This is the rate determining step of the reaction, meaning the product formation depends on the concentration of both the Pt^{II} starting complex, and the incoming ligand. The *trans* effect, in which a ligand can labilize the group in the *trans* position to it, is the deciding factor in which ligand will be removed. Ligands with a high *trans* effect can be influential through σ-bonding and π-bonding (Figure 2.1).[1] Strong σ-donor groups weaken the bond to the ligand in the *trans* position. Strong π-acceptors draw electron density from the metal centre, making the *trans* ligand electron-deficient and therefore susceptible to nucleophilic attack. The *trans* effect can be used to predict which product will be obtained based on the order in which the reagents are added, however substitution reactions of square-planar platinum complexes do not always yield the more thermodynamically preferred product. In the case of cisplatin, by starting with potassium tetrachloroplatinate and adding the amine ligands, the strong *trans* directing chloride groups dictate the formation of the *cis* diamine product.

$$CO, CN^-, C_2H_4 > PR_3, H^- > CH_3^- > R_2S > C_6H_5^-, NO_2^-, I^- > SCN^- > Br^- > Cl^- > pyridine > NH_3 > OH^- > H_2O$$

Figure 2.1 The empirical series comparing the trans-effect of ligands based on the kinetics of substitution reactions.[2]

The novel complexes produced in this project were based upon the design of previously established Pt^{IV} prodrugs, primarily *trans,trans,trans*-[Pt(*py*)$_2$(N$_3$)$_2$(OH)$_2$] which was synthesised by Farrer *et al*.[3] This compound in particular is easily synthesised with a good yield, has high aqueous solubility (ca. 34 mM), is non-toxic towards cells in the absence of irradiation and shows potent phototoxicity towards several human immortalised cell lines. The ability of Pt^{II} complexes to undergo associative ligand substitution reactions is used to preferentially produce either the *cis*- or *trans*-isomers of the synthesised complexes.

All UV-Vis irradiation studies on complexes in this chapter were carried out in water at a concentration of 100 μM, using a Thorlabs high-power mounted LED (model M405L4 (405 nm)).

2.2 Known compounds

2.2.1 Iproplatin

Iproplatin (*cis,cis,trans*-[Pt(NH$_2$^{i}Pr)$_2$Cl$_2$(OH)$_2$]) is a Pt^{IV} drug that was developed by Johnson Matthey and Bristol Myers Squibb, and which is believed to be reduced *in vivo* to give a Pt^{II} species that then acts via the same mechanism as cisplatin.[4] The detection of the Pt^{II} metabolite *cis,cis*-[Pt(NH$_2$^{i}Pr)$_2$Cl$_2$] in the urine and blood plasma of patients treated with the drug supports the proposed reduction mechanism.[5] It has been extensively studied in human clinical trials, with five Phase I, twenty-two Phase II and one Phase III trials involving more than 1000 patients.[6] Phase I trials found that doseage had to be limited due to myelosuppression, and so

a recommended maximum dose of 300 mg m^{-2} was carried through to Phase II trials.[7] Phase II trials have been conducted in a variety of different cancers including; ovarian, breast, squamous cell carcinomas, cervical, testicular, paediatric neuroblastomas and paediatric malignant solid tumours.[8–14] In most of these cancers iproplatin was found to be largely inactive, and where it was active it was often less effective than both cisplatin and carboplatin.[11,15,16] Progression of the drug was also impeded by toxic deaths and occurrence of dose limiting platelet deficiency.[9,12,17] The only Phase III trial involved coadministration of the drug with cyclophosphamide for the treatment of ovarian cancer, however it was concluded that there was no improvement compared to cisplatin.[18] Improving the selectivity and targetting of iproplatin may be beneficial in better exploiting its anticancer properties *in vivo*.

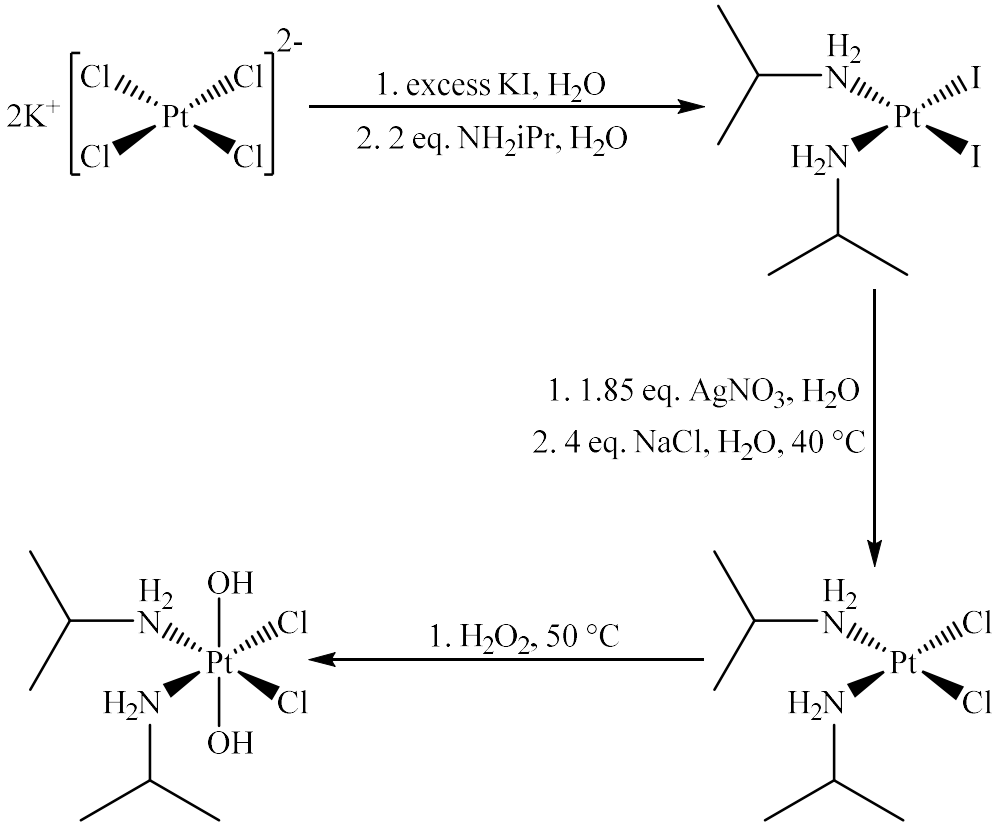

Figure 2.2 Schematic diagram showing the multistep synthesis used to produce Iproplatin.

In this research, synthesis of the Pt^{II} intermediates, *cis,cis*-[$Pt(NH_2{}^iPr)_2I_2$] and *cis,cis*-[$Pt(NH_2{}^iPr)_2Cl_2$], was achieved using the method reported by Pantoja *et al.*, which was adapted from the original cisplatin synthesis described by S. C. Dhara in 1970 (Figure 2.2).[19–21] Subsequent oxidation to the final compound was achieved by following the method reported by Barnard *et al.*[22,23] The final complex and all intermediates were characterised by ^1H, ^{13}C and ^{195}Pt NMR spectroscopy, and ES^+ mass spectrometry. The ^{195}Pt NMR spectra are particularly useful for characterisation, as the single resonance for the Pt^{II} precursor to iproplatin appears in the Pt^{II} region and the resonance for iproplatin appears in the significantly downfield shifted Pt^{IV} region (Figure 2.3).

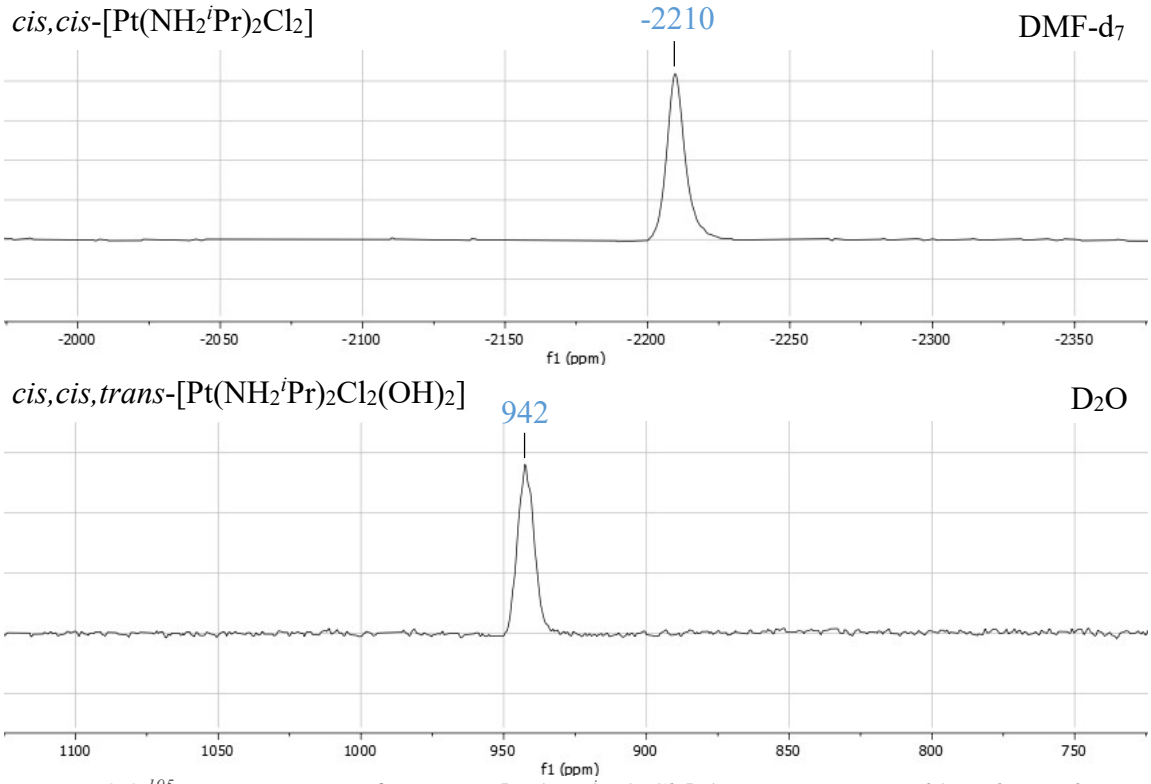

Figure 2.3 ^{195}Pt NMR spectra for cis,cis-[$Pt(NH_2{}^iPr)_2Cl_2$] (top, run in DMF-d_7) and iproplatin (bottom, run in D_2O).

One of the main properties that makes iproplatin interesting from a clinical application perspective is its high aqueous solubility. Replicate experiments conducted for this research found iproplatin to have an average water solubility of 58.2 mg mL^{-1} (139.3 mM), which is the

highest of all the compounds discussed in this work. In order to better understand how this compound could be encapsulated into liposomes, ^{1}H NMR spectroscopy titration experiments were undertaken to calculate the pK_a of the complex. The results of these experiments are detailed in Chapter 3.

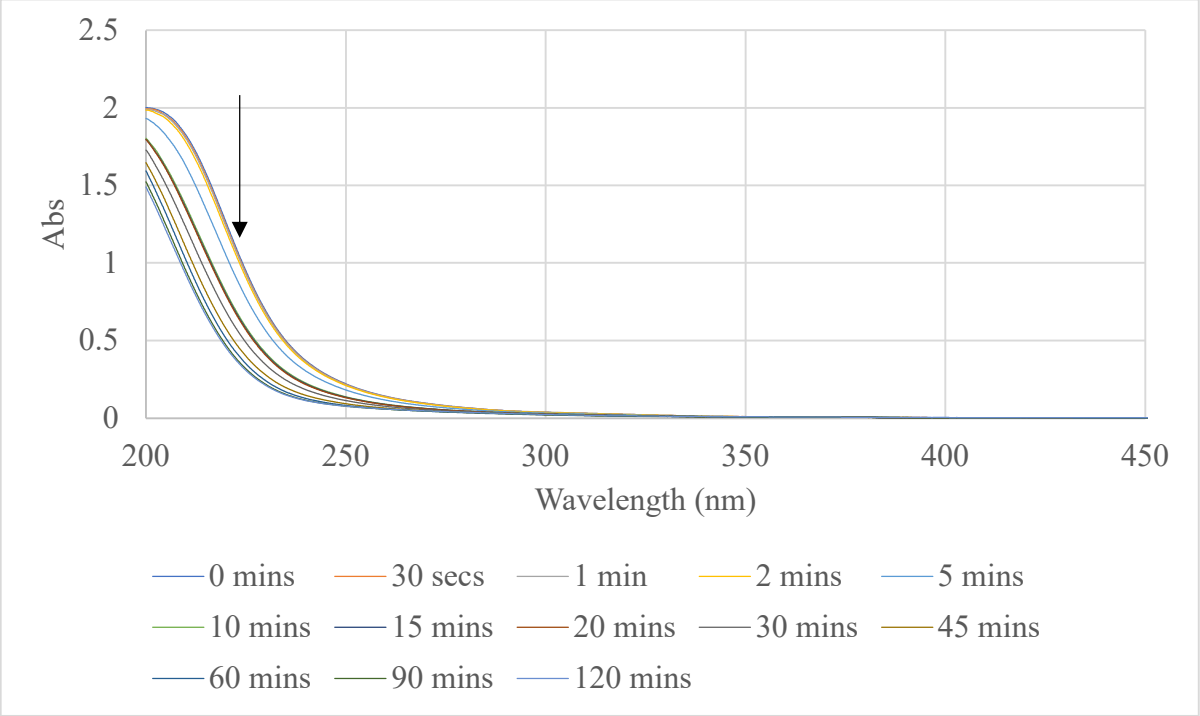

Figure 2.4 UV-Vis absorption spectrum for iproplatin after irradiation with visible light (405 nm).

The UV-Vis spectrum of iproplatin (100 µM in H_2O) doesn't show any significant characteristic peaks, suggesting it is only weakly absorbing in the visible region (Figure 2.4). However, it is possible to see a decrease in the absorption curve, between 200-350 nm, as the length of time the sample was irradiated for increases. This suggests that the drug is either being reduced or decomposed by irradiation with 405 nm light. Irradiation also induced a small amount of yellow precipitate to form, which agrees with the idea that decomposition is occurring, however the quantity of the solid isolated was too small to analyse. ^{1}H NMR spectra taken of the solution before and after irradiation don't show any difference in the peaks present,

however there is approximately a 50% reduction in the intensity of the peaks, indicating that the concentration of the iproplatin has reduced. The same is true for mass spectra taken before and after irradiation. The peaks present do not change, but the intensity has reduced by approximately half.

2.2.2 *trans,trans,trans*-[Pt(*py*)$_2$(N$_3$)$_2$(OH)$_2$]

trans,trans,trans-[Pt(*py*)$_2$(N$_3$)$_2$(OH)$_2$] is a Pt^{IV} complex that was first synthesised by Farrer *et al.* in 2010.[3] It was developed in an attempt to improve upon the properties of the mono and bis amine complexes, *trans,trans,trans*-[Pt(*py*)(NH$_3$)(N$_3$)$_2$(OH)$_2$] and *trans,trans,trans*-[Pt(NH$_3$)$_2$(N$_3$)$_2$(OH)$_2$].[24,25] It is photoactivatable by UVA, blue and green light, which is an improvement upon complexes that are only UV activatable as short wavelength activation has limited clinical applications.[26] It was also found to be potently photocytotoxic towards several cell lines; HaCaT (keratinocytes), A2780 (and its cisplatin resistance variant, A2780CIS), OE19, and HepG2. ^{1}H NMR spectroscopy studies showed that there was no loss of the pyridine ligands upon irradiation, which may be a factor in the increased cytotoxicity.

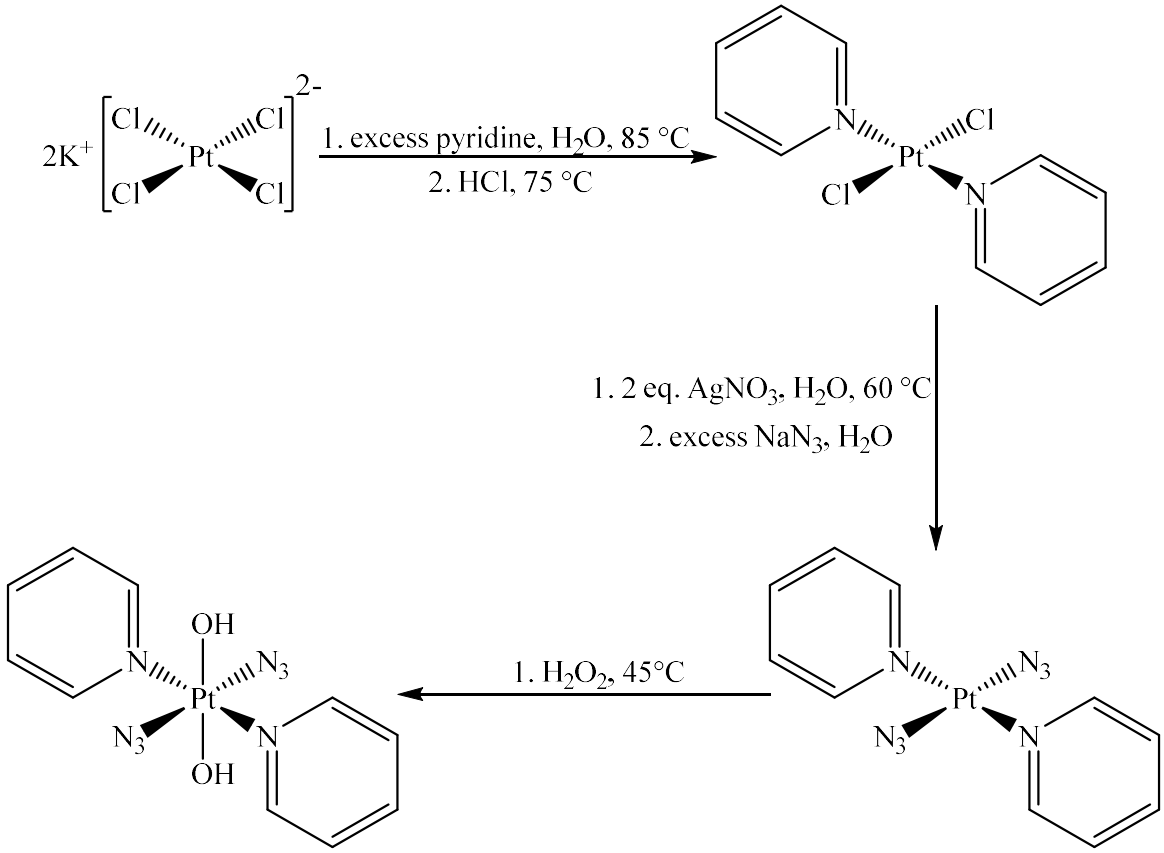

Figure 2.5 Schematic diagram showing the multistep synthesis used to produce t,t,t-[Pt(py)$_2$(N$_3$)$_2$(OH)$_2$].

The final complex and all intermediates were synthesised following the procedure first described by Farrer *et al* (Figure 2.5).[3] The complex is known to have good aqueous solubility (reported at 34 mM), which was corroborated by replicate experiments that found a solubility of 16.7 mg mL^{-1} (35.4 mM). As for iproplatin, ^{1}H NMR spectroscopy titration experiments were undertaken to calculate the pK_a of the complex and the results of these experiments are detailed in Chapter 3.

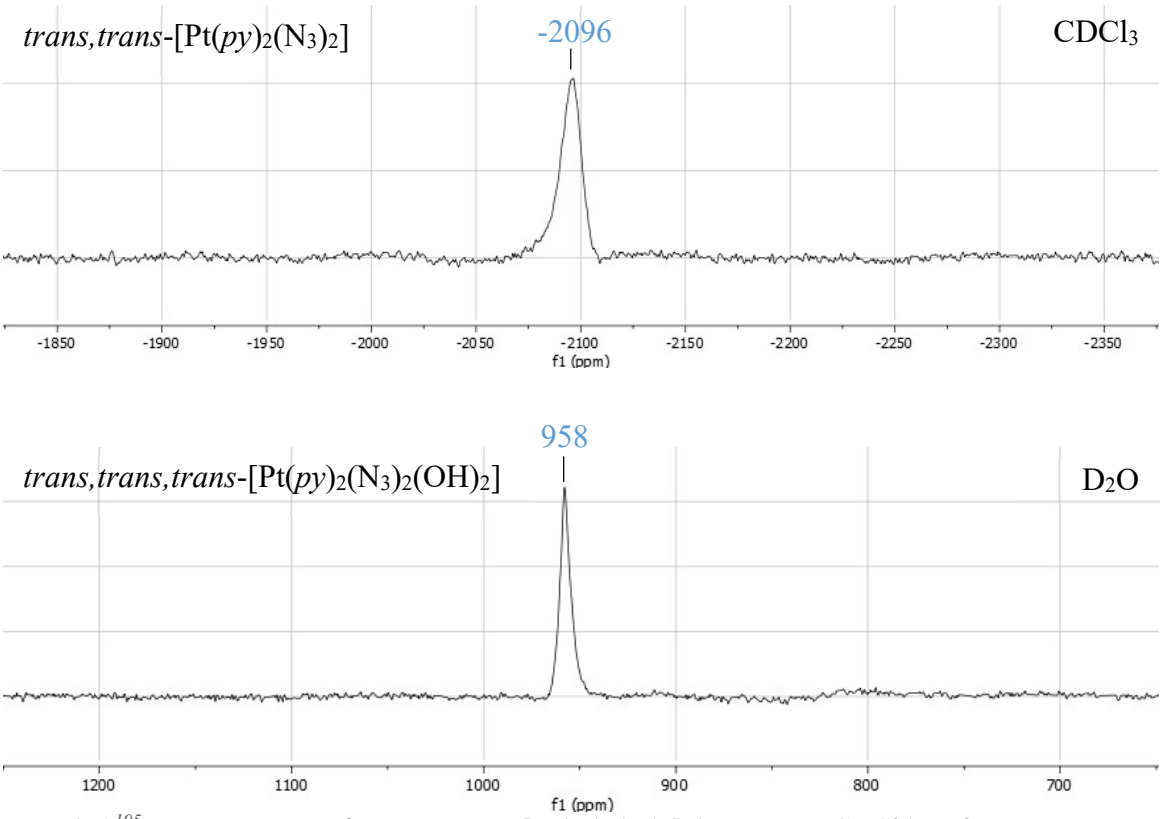

Figure 2.6 ^{195}Pt NMR spectra for trans,trans-[Pt(py)$_2$(N$_3$)$_2$] (top, run in CDCl$_3$) and trans,trans,trans-[Pt(py)$_2$(N$_3$)$_2$(OH)$_2$] (bottom, run in D$_2$O).

The ^{195}Pt NMR spectra show a significant downfield shift from the Pt^{II} precursor, to the oxidised Pt^{IV} product (Figure 2.6). This is expected, as the resonances appear in the characteristic regions corresponding to the oxidation state of the Pt centre.

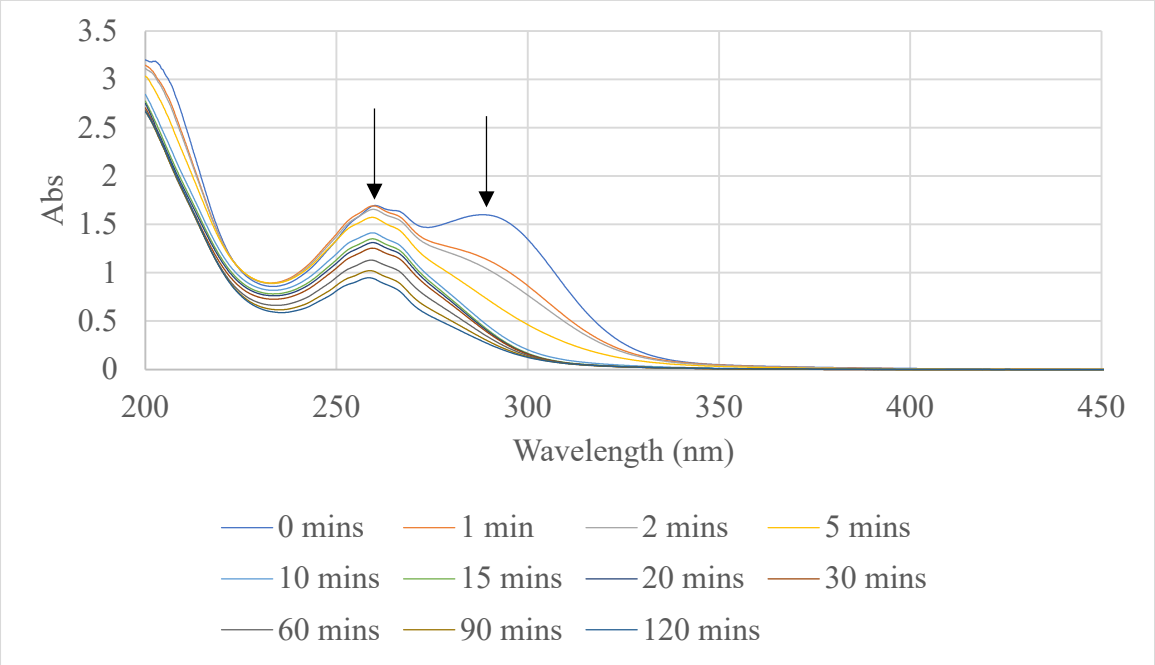

Figure 2.7 UV-Vis absorption spectrum for t,t,t-[Pt(py)$_2$(N$_3$)$_2$(OH)$_2$] after irradiation with visible light (405 nm).

The UV-Vis spectrum of *trans,trans,trans*-[Pt(*py*)$_2$(N$_3$)$_2$(OH)$_2$] has characteristic peaks at 260 nm and 288 nm (Figure 2.7). According to time-dependent density function theory (TDDFT) calculations, these can be assigned as dissociative ^{1}LMCT(N$_3$→Pt) and mixed ^{1}LMCT/^{1}IL (OH→Pt,N$_3$; IL = interligand) transitions.[3] There is a significant reduction in the intensity of both peaks as the time of irradiation increases, which corresponds with the suggested photodecomposition method by loss of either the hydroxyl or azide ligands. The UV-Vis spectrum for free pyridine shows an absorbtion peak at approximately 260 nm which has the same fine structure as the above spectra.[27] If loss of the pyridine ligands was occurring during irradiation, absorbances in this region would still be expected.

Irradiation induced significant precipitation from solution, lightening of the yellow colour of the solution, and bubbles could be seen. This is concordant with the observations reported in the original paper. The formation of bubbles could be evidence for the loss of the azide radicals,

which rapidly convert to nitrogen gas. ^{1}H NMR spectra taken of the solution before and after irradiation show an increase in the intensity of the residual water peak. This could be related to loss of the hydroxyl groups from the compound during irradiation. There is also a reduction in the intensity of the peaks corresponding to the compound protons of approximately 72%, indicating that the concentration of the drug has reduced.

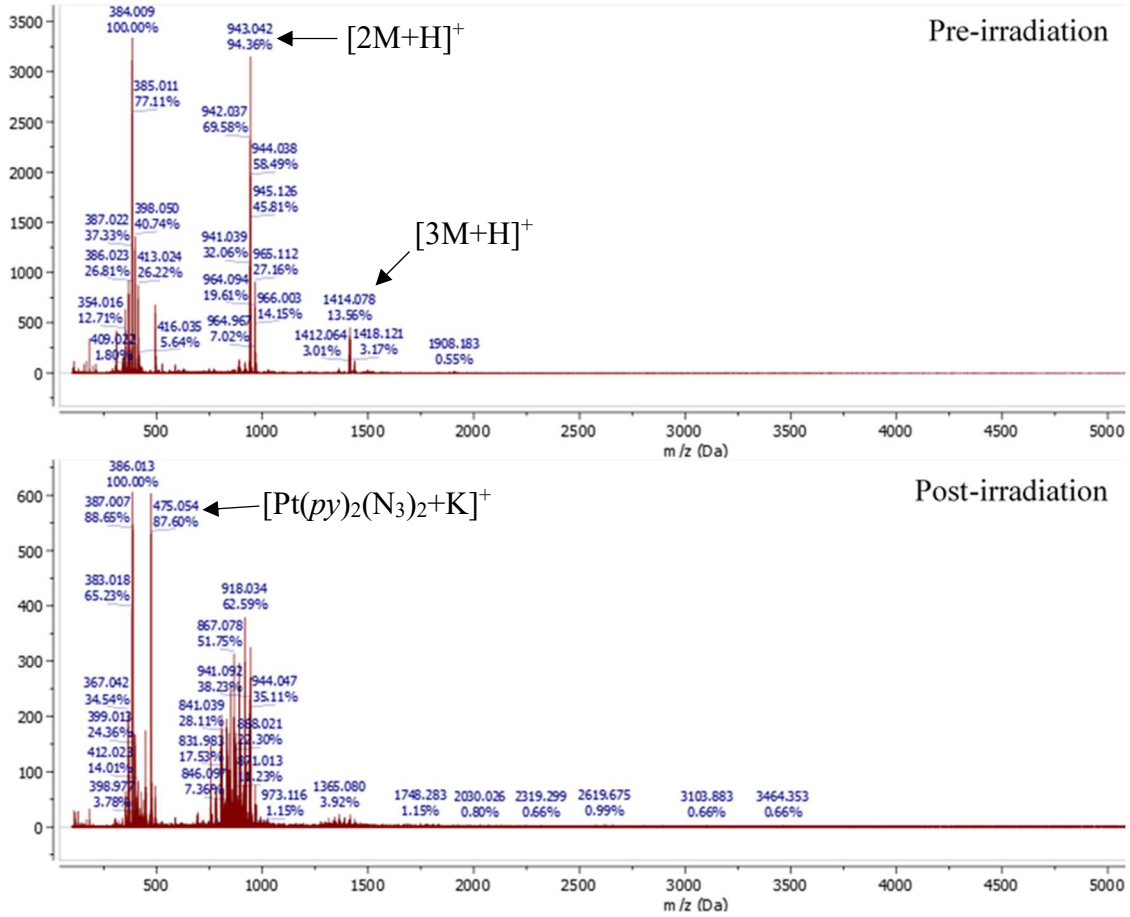

Figure 2.8 Mass spectra for t,t,t-[Pt(py)$_2$(N$_3$)$_2$(OH)$_2$] pre- and post-irradiation (405 nm, 120 minutes).

Mass spectra taken before and after irradiation show quite obvious differences, such as the significant reduction in intensity of the peak at 943 *m/z* which correlates to the $[2M+H]^+$ fragment, and disappearance of the peak at 1414 *m/z* with correlates to the $[3M+H]^+$ fragment (Figure 2.8). The post-irradiation spectrum has several new resonances arising between 750 and 1000 *m/z*, however the identity of these has not been identified. The resonance at 475 *m/z* can be assigned to $[Pt(py)_2(N_3)_2+K]^+$, suggesting photoinduced loss of the hydroxyl groups.

2.3 Novel compounds

Based upon the established methods used in the discovery of previous photoactivatable Pt^{IV} complexes, two novel diazido compounds have been developed. The use of two nitrogen coordinating ligands, thiazole and pyrazine, was explored to see if comparisons could be drawn to the pre-existing pyridine and thiazole containing compounds. Their synthesis, characterisation, and photochemical properties are discussed in the following section.

2.3.1 *cis,cis,trans*-[Pt(*tz*)$_2$(N$_3$)$_2$(OH)$_2$]

Thiazole (C_3H_3NS) has previously been explored as a possible ligand for platinum complexes due to its planar structure, and chemical similarity to pyridine. The antibiotic bleomycin, which contains a diathiazole unit, has also been shown to bind to DNA.[28,29] Van Beusichem and Farrell originally synthesised both the *cis*- and *trans*-isomers of [Pt(*tz*)$_2$Cl$_2$] in 1992, characterising the compounds by NMR spectroscopy and X-ray crystallography.[30] They demonstrated that the thiazole ligands were conjugating to the platinum via the nitrogen, rather than the sulphur. Further research by both Bierbach and McGowan yielded both the *cis*- and *trans*-isomers of the mixed thiazole-amine product [Pt(*tz*)(NH$_3$)Cl$_2$].[31,32] More recently, Peter Sadler's group have focused on developing both Pt^{II} and Pt^{IV} trans-thiazole complexes, with the inclusion of azide ligands in order to make the complexes photoactivatable (Figure 2.9).[25,33–35]

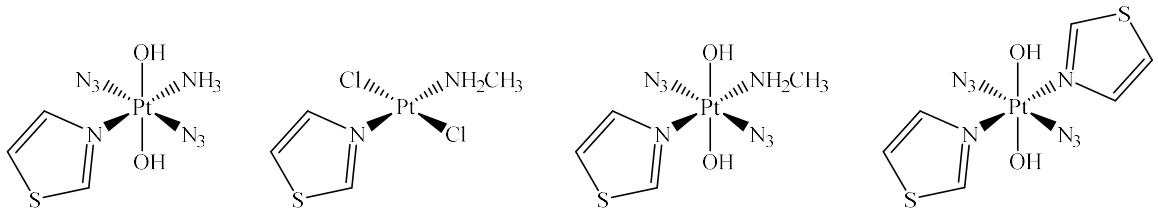

Figure 2.9 Structures of the thiazole containing platinum compounds produced by Peter Sadler's group.[25,33–35]

The trans-isomers have been explored in more detail due to the improved cytotoxicity they show against cisplatin resistant cells.[36] This thesis will look at the synthesis and characteristics of the Pt^{IV} photoactivatable *cis*-thiazole complex, as this has not previously been made and the comparison to the *trans* isomer is of interest.

Figure 2.10 shows the multistep synthesis used to obtain *cis,cis,trans*-[Pt(*tz*)$_2$(N$_3$)$_2$(OH)$_2$]. By starting with potassium tetrachloroplatinate and substituting the chlorides for iodides, the strong *trans* directing iodide groups dictate the formation of the *cis*-thiazole product. Further substitutions yielded the Pt^{II} dithiazole diazide intermediate, which was oxidised to its Pt^{IV} analogue using hydrogen peroxide to give hydroxyl groups in the axial positions.

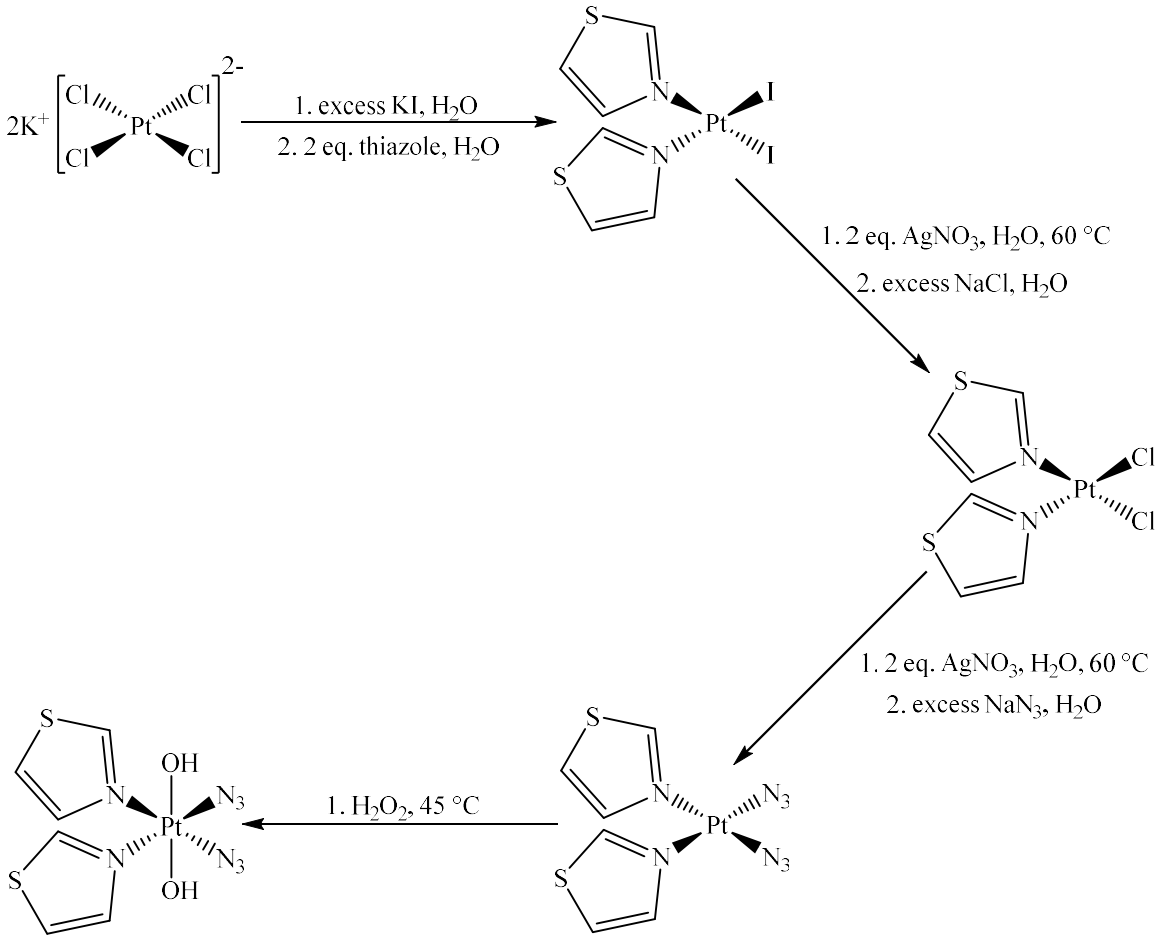

Figure 2.10 Schematic diagram showing the multistep synthesis used to produce c,c,t-[Pt(tz)$_2$(N$_3$)$_2$(OH)$_2$].

The final product was synthesised in a good yield (63%), and characterised by ^{1}H, ^{13}C, and ^{195}Pt NMR spectroscopy and mass spectrometry. It is reasonably soluble in water (ca. 11.3 mg mL^{-1} / 23.4 mM), and does not show decomposition when exposed to ultrasound, which is a desirable property for delivery in conjunction with liposomes and microbubbles. ^{1}H

NMR spectroscopy titration experiments to calculate the pK_a of the complex are detailed in Chapter 3.

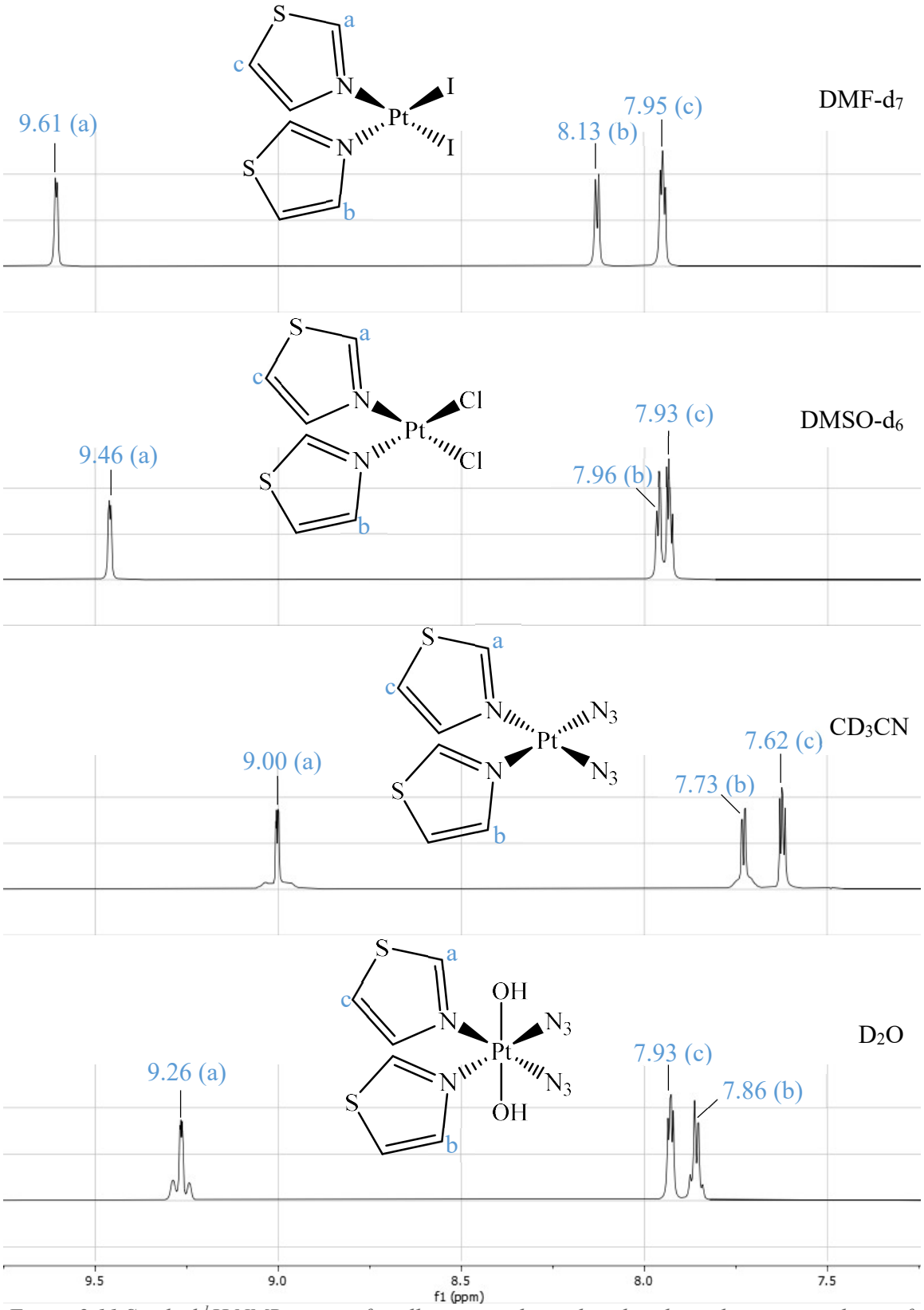

Figure 2.11 Stacked ^{1}H NMR spectra for all compounds produced in the multi-stage synthesis of cis,cis,trans-$[Pt(tz)_2(N_3)_2(OH)_2]$.

Figure 2.11 shows the ^{1}H NMR spectra for the Pt^{II} intermediates, and the final Pt^{IV} product in the synthesis of *cis,cis,trans*-[Pt(*tz*)$_2$(N$_3$)$_2$(OH)$_2$]. Although the analyses were run in different deuterated solvents, there are still some notable changes in shift, such as the change in separation between the b and c proton resonances from *cis,cis*-[Pt(*tz*)$_2$I$_2$] to *cis,cis*-[Pt(*tz*)$_2$Cl$_2$]. The b and c protons are also interesting as in the final product the b proton resonance is upfield of the c proton resonance, whereas for all the Pt^{II} intermediates they appear the other way around. This indicates that the b protons are more shielded in the final product. The spectrum for *cis,cis*-[Pt(*tz*)$_2$(N$_3$)$_2$] shows the appearance of broad Pt satellites on the a and b proton resonances. The linewidth of these satellites indicates that the complex is a Pt^{II} species. Comparatively, the Pt satellites in the spectrum for *cis,cis,trans*-[Pt(*tz*)$_2$(N$_3$)$_2$(OH)$_2$] are much sharper, showing the change from Pt^{II} to Pt^{IV}.

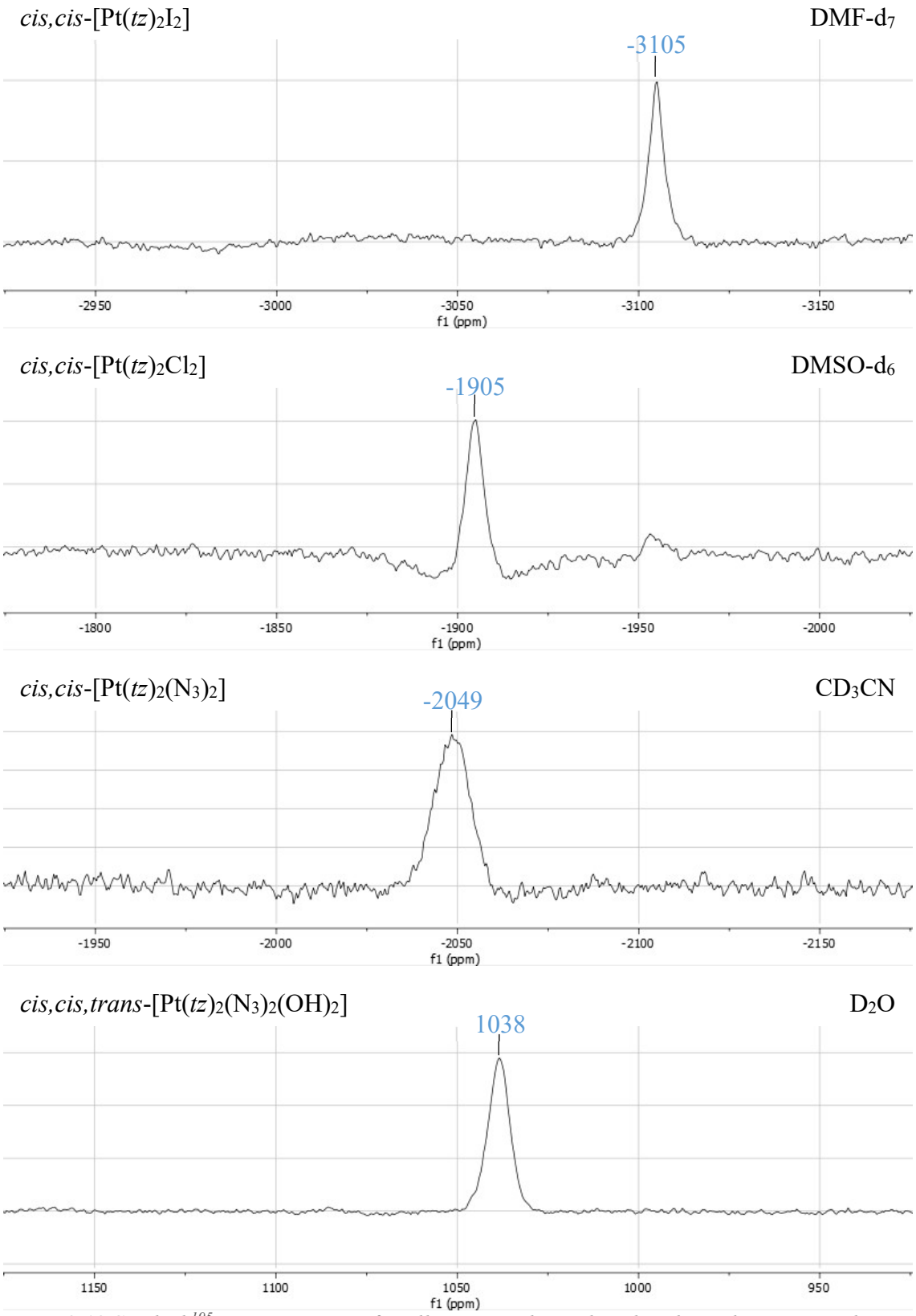

Figure 2.12 Stacked ^{195}Pt NMR spectra for all compounds produced in the multi-stage synthesis of cis,cis,trans-[Pt(tz)$_2$(N$_3$)$_2$(OH)$_2$].

Figure 2.12 shows the ^{195}Pt spectra for the intermediates and final complex produced in the synthesis of *cis,cis,trans*-[Pt(*tz*)$_2$(N$_3$)$_2$(OH)$_2$]. The resonance for the first intermediate, *cis,cis*-[Pt(*tz*)$_2$I$_2$], is significantly upfield compared to the resonances for the other complexes. This suggests that the iodide ligands have a stronger shielding effect compared to the chloride and azide ligands. The spectrum for *cis,cis*-[Pt(*tz*)$_2$Cl$_2$] shows a strong resonance at -1905 ppm corresponding to the named complex, however there is a smaller peak appearing at -1953 ppm. The source of this resonance is unknown, and because the ^{1}H NMR spectrum for the complex was clean, the next synthetic step was proceeded with. The resonances for the three intermediates all appear in the expected Pt^{II} region of the spectrum, with the resonance for the final oxidised complex showing an obvious shift into the Pt^{IV} region.

As mentioned, the *trans*-isomer of the Pt^{IV} product has been previously synthesised by Sadler *et al*.[35] The NMR spectra for *trans,trans,trans*-[Pt(*tz*)$_2$(N$_3$)$_2$(OH)$_2$] were assigned as follows:

^{1}H NMR (D$_2$O, 400 MHz) δ (ppm) 9.58 (2H, doublet of doublets, H$_a$), 8.30 (2H, doublet of doublets, H$_c$), 8.07 (2H, triplet, H$_b$) ppm. ^{13}C NMR (D$_2$O, 150 MHz) δ (ppm) 157.8 (C$_a$), 140.3 (C$_b$), 123.8 (C$_c$). ^{195}Pt NMR (D$_2$O, 129 MHz) δ (ppm) 977 ppm.

The assigned data for the *cis*-isomer, *cis,cis,trans*-[Pt(*tz*)$_2$(N$_3$)$_2$(OH)$_2$], is given below:

^{1}H NMR (D$_2$O, 400 MHz) δ (ppm) 9.26 (2H, doublet of doublets, H$_a$), 7.93 (2H, doublet of doublets, H$_c$), 7.86 (2H, doublet of doublets, H$_b$) ppm. ^{13}C NMR (D$_2$O, 101 MHz) δ (ppm) 157.3 (C$_a$), 139.5 (C$_b$), 123.8 (C$_c$) ppm. ^{195}Pt NMR (D$_2$O, 86 MHz) δ (ppm) 1038 ppm.

Both complexes were analysed in D$_2$O, and as such comparisons can be drawn between the data sets. The ^{1}H NMR spectra resonances for the *cis*-isomer are upfield shifted compared to the resonances for the *trans*-isomer, which indicates higher shielding. The ^{13}C NMR spectra

don't show significant differences in chemical shift between the two complexes. The ^{195}Pt NMR spectra show that the *cis*-isomer resonance appears downfield of the *trans*-isomer resonance, indicating it is deshielded compared to the *trans*-isomer.

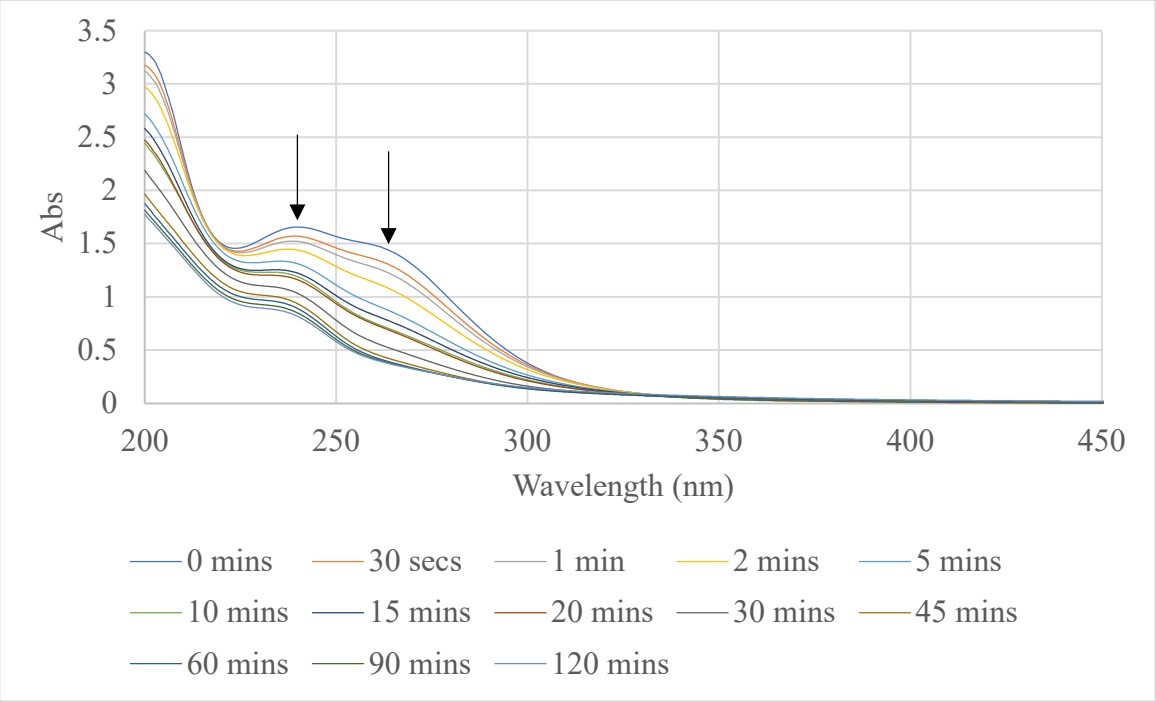

Figure 2.13 UV-Vis absorption spectrum for c,c,t-[Pt(tz)$_2$(N$_3$)$_2$(OH)$_2$] after irradiation with visible light (405 nm).

The UV-Vis spectrum of *cis,cis,trans*-[Pt(*tz*)$_2$(N$_3$)$_2$(OH)$_2$] shows a peak at 240 nm, and a broad shoulder at approximately 265 nm (Figure 2.13). Both of these resonances decrease in intensity with longer durations of irradiation. Free thiazole absorbs between 200-260 nm, and so if loss of the thiazole ligands was occurring absorbances in this region would still be expected.[37] There is a minimal increase in the absorption intensity at approximately 355 nm as the exposure time increases, with an isosbestic point occurring at 335 nm. This could correlate to the increasing concentration of a Pt^{II} photoreduction product, which is weakly absorbing at 355 nm compared to the Pt^{IV} starting compound. Irradiation induced precipitation from solution and bubbles could be seen forming.

^{1}H NMR spectra taken before and after irradiation show the formation of new peaks, which can be assigned as free thiazole. This indicates that the ligands are dissociating as a result of visible light exposure. There is also a 72% decrease in the intensity of the conjugated ligand peaks, which reinforces the concept that the drug is breaking down.

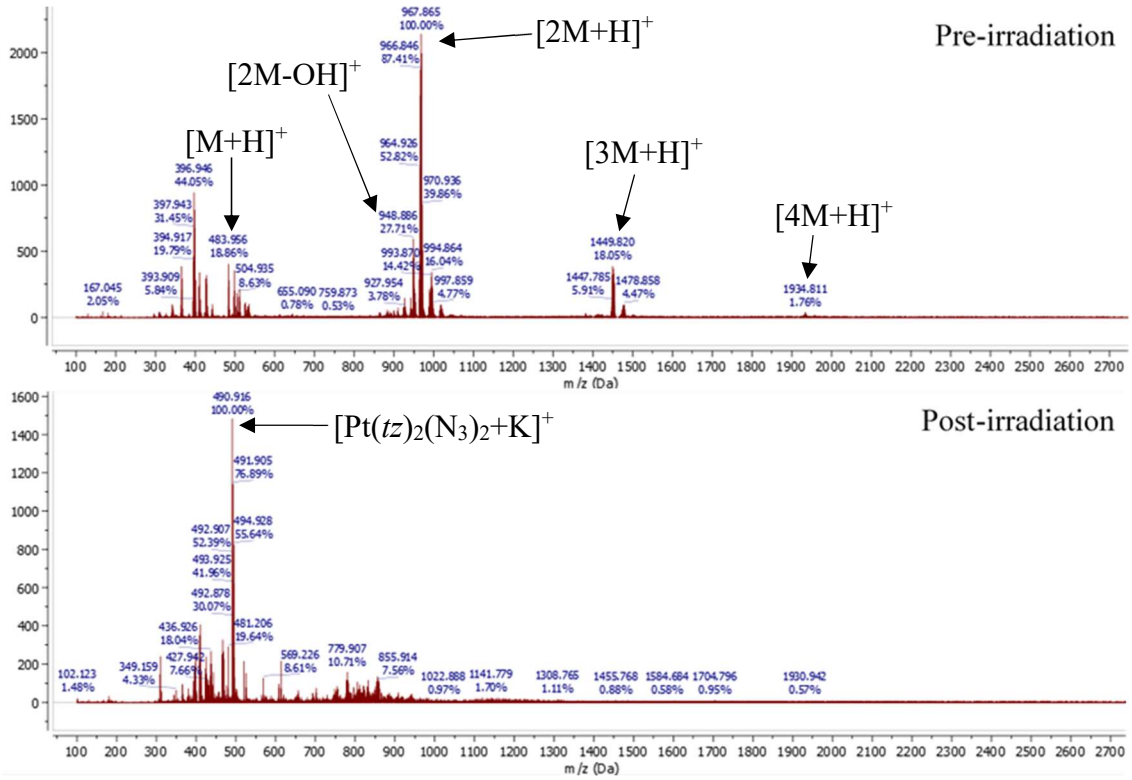

Figure 2.14 Mass spectra of c,c,t-[Pt(tz)$_2$(N$_3$)$_2$(OH)$_2$] pre- and post-irradiation (405 nm, 120 minutes).

Mass spectra taken before and after irradiation show significant changes (Figure 2.14). The pre-irradiation spectrum shows the presence of the compound with the following masses; 484 ([M+H]$^+$), 949 ([2M-OH]$^+$), 967 ([2M+H]$^+$), 1450 ([3M+H]$^+$), and 1935 ([4M+H]$^+$). The post-irradiation spectrum does not contain any of these masses, suggesting a total breakdown of the drug in solution. The peak at 490 *m/z* in the post-irradiation spectra could correlate to the fragment [Pt(*tz*)$_2$(N$_3$)$_2$+K]$^+$, indicating a loss of the hydroxyl groups upon irradiation.

2.3.2 *trans,trans,trans*-[Pt(*pz*)$_2$(N$_3$)$_2$(OH)$_2$]

There are several examples in the literature of pyrazine being used as a bridging ligand in bimetallic complexes. Iengo *et al*. explored its use in Ru^{III} dimers that developed upon previous antimetastatic complexes.[38] It has also been used in mixed bimetallic Pd^{II} and Pt^{II} complexes, which showed cytotoxicity in HeLa (human cervical cancer) and A375 (human melanoma) cell lines.[39] Komeda *et al*. used pyrazine, pyrimidine, and pyridazine bridging ligands in Pt^{II} dimer complexes based on cisplatin, and found increased cytotoxicity in mouse cell lines, but reduced cytotoxicity in human cell lines compared to cisplatin.[40] Finally, further bimetallic complexes using the scaffolds of alternative Pt^{II} complexes (e.g. oxaliplatin) showed significant antitumour effects.[41] There has been little research in to pyrazine containing Pt monomers, so these will be explored in this thesis.[42,43]

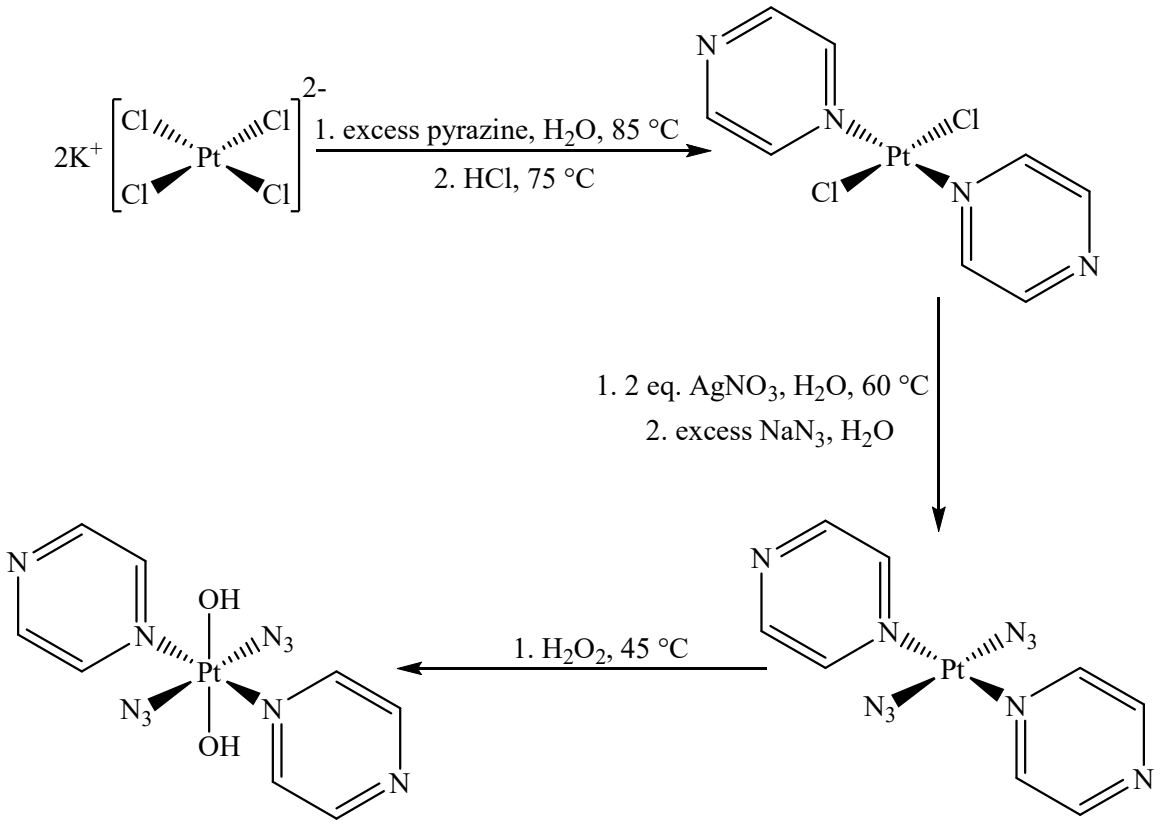

Figure 2.15 Schematic diagram showing the multistep synthesis used to produce t,t,t-[Pt(pz)$_2$(N$_3$)$_2$(OH)$_2$].

The synthesis, shown in Figure 2.15, followed the methods used to produce *trans,trans,trans*-$[Pt(py)_2(N_3)_2(OH)_2]$.[3] The final Pt^{IV} complex was produced in reasonable yield (67%), and was characterised by NMR spectroscopy and mass spectrometry. The compound is stable when exposed to ultrasound, however it is only sparingly soluble in water (ca. 4.0 mg mL^{-1} / 8.5 mM). Determination of the pK_a by ^1H NMR spectroscopy was conducted to assess how this compound could be loaded into liposomes. This is detailed in Chapter 3.

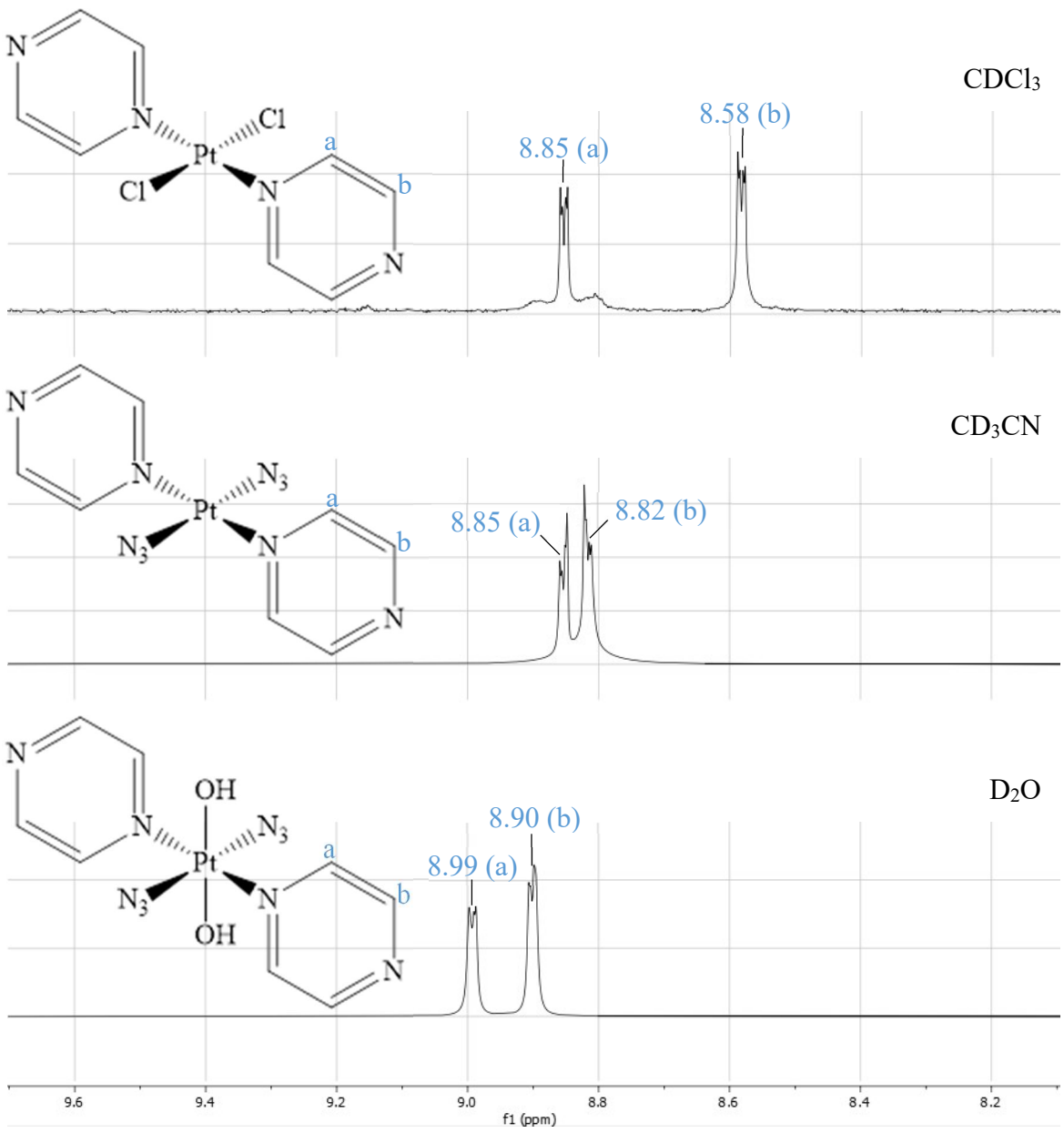

Figure 2.16 Stacked ^{1}H NMR spectra for all compounds produced in the multi-stage synthesis of trans,trans,trans-[Pt(pz)$_2$(N$_3$)$_2$(OH)$_2$].

Figure 2.16 shows the ^{1}H NMR spectra for the Pt^{II} intermediates, and the final Pt^{IV} product in the synthesis of *trans,trans,trans*-[Pt(*pz*)$_2$(N$_3$)$_2$(OH)$_2$]. Although the analyses were run in different deuterated solvents, there are still some notable changes in shift, with both resonances progressively shifting downfield with each successive reaction. The spectrum for *trans,trans*-[Pt(*pz*)$_2$Cl$_2$] shows the appearance of broad Pt satellites on both the a and b proton resonances.

The linewidth of these satellites indicates that the complex is a Pt^{II} species. No Pt satellites can be seen on the spectra for *trans,trans*-[Pt(*pz*)$_2$(N$_3$)$_2$] or *trans,trans,trans*-[Pt(*pz*)$_2$(N$_3$)$_2$(OH)$_2$], however this is likely due to poor resolution resulting from low solubility of the complexes.

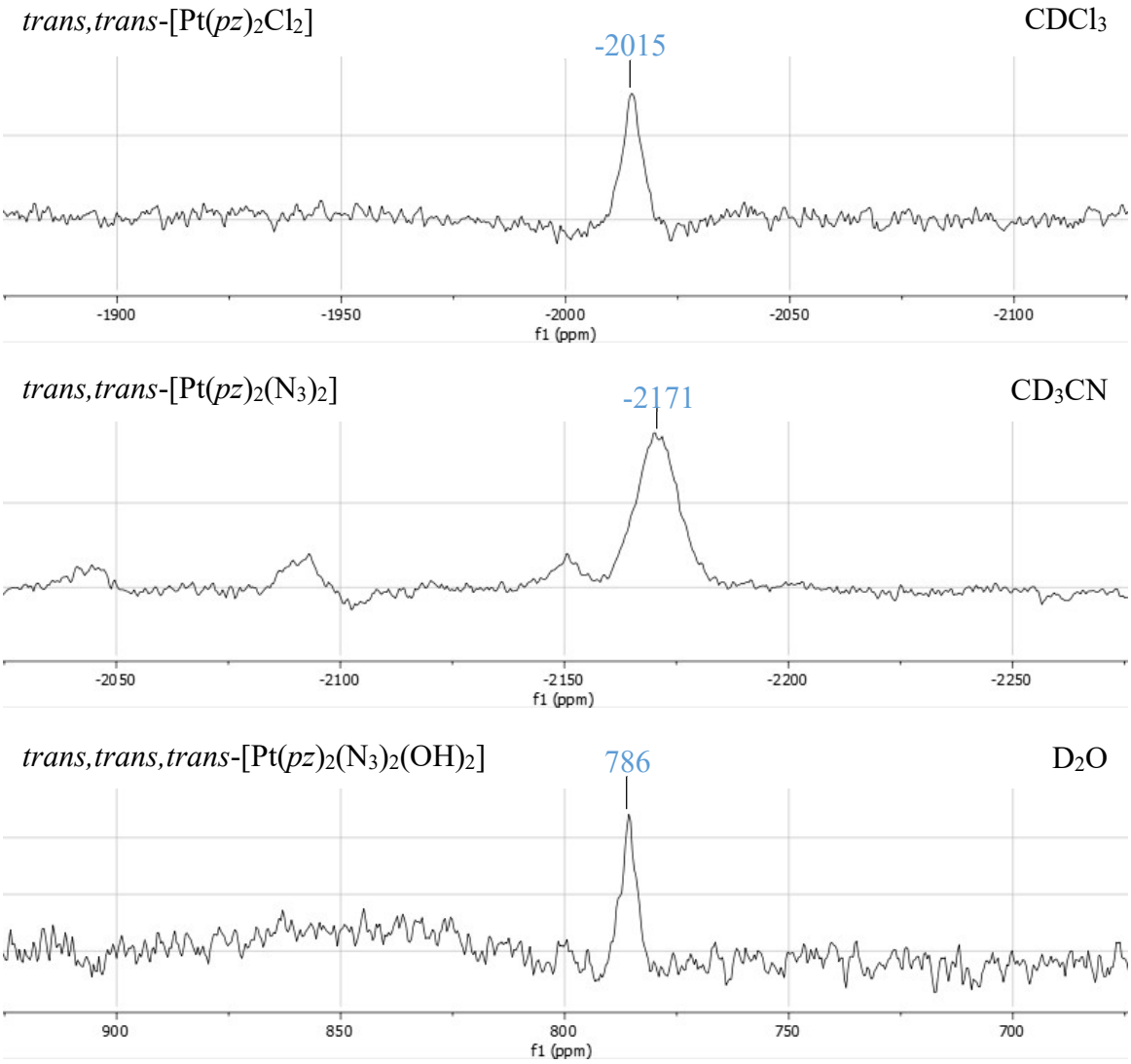

Figure 2.17 Stacked ^{195}Pt NMR spectra for all compounds produced in the multi-stage synthesis of trans,trans,trans-[Pt(pz)$_2$(N$_3$)$_2$(OH)$_2$].

Figure 2.17 shows the ^{195}Pt spectra for the interemediates and final complex produced in the synthesis of *trans,trans,trans*-[Pt(*pz*)$_2$(N$_3$)$_2$(OH)$_2$]. The spectrum for *trans,trans*-[Pt(*pz*)$_2$(N$_3$)$_2$] shows a strong resonance at -2171 ppm corresponding to the named complex, however there are several smaller peaks appearing downfield of this. The source of these resonances is

unknown, and no other resonances were seen in the the ^{1}H NMR or ^{13}C spectra for the complex. The resonances for the two intermediates appear in the expected Pt^{II} region of the spectrum, with the resonance for the final oxidised complex showing an obvious shift into the Pt^{IV} region.

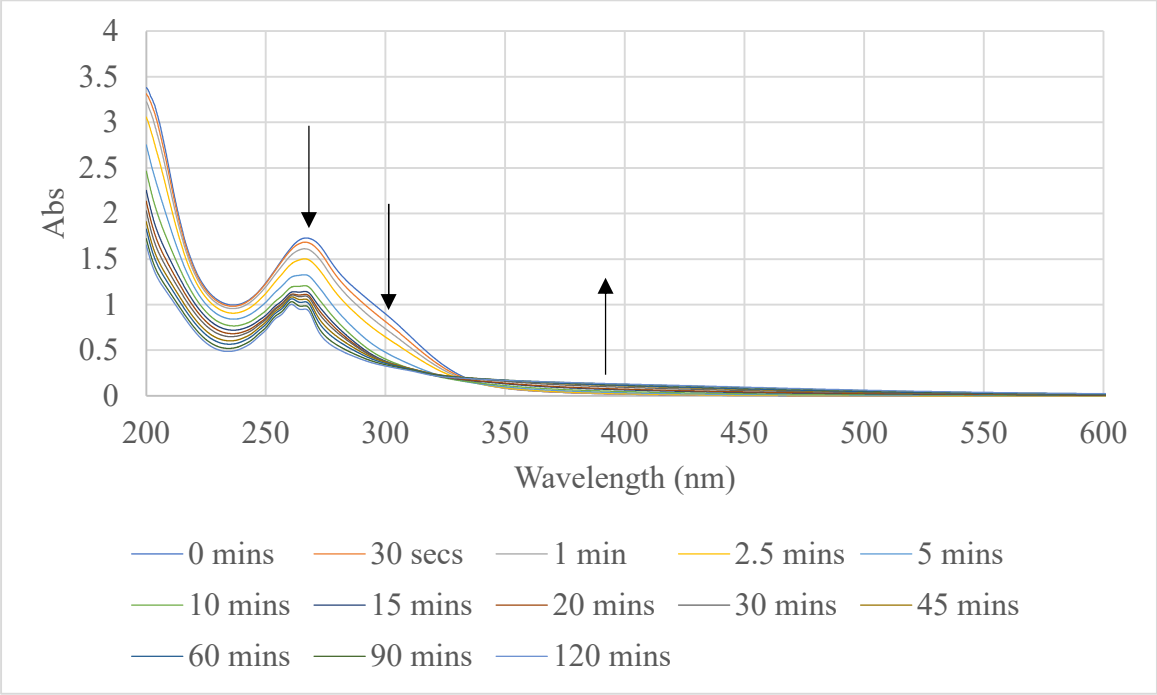

Figure 2.18 UV-Vis absorption spectrum for t,t,t-[Pt(pz)$_2$(N$_3$)$_2$(OH)$_2$] after irradiation with visible light (405 nm).

The UV-Vis spectrum for *trans,trans,trans*-[Pt(*pz*)$_2$(N$_3$)$_2$(OH)$_2$] shows a characteristic peak at 265 nm, that upon irradiation decreases in intensity and starts to show finer detail of a 'triplet' style resonance (Figure 2.18). This absorption pattern correlates with that of free pyrazine, so the appearance of this finer detail could indicate the release of the pyrazine upon photoactivation.[44] There is also a very broad shoulder in the spectrum at approximately 300 nm, which also reduces in intensity with irradiation. There is a small increase in the absorption intensity at approximately 400 nm as the exposure time increases, with an isosbestic point occurring at 330 nm. This could correlate to the increasing concentration of a Pt^{II} photoreduction product, which is weakly absorbing at 400 nm compared to the Pt^{IV} starting

compound. When comparing this data to that of *trans,trans,trans*-[Pt(*py*)$_2$(N$_3$)$_2$(OH)$_2$], similarties can be drawn. Both spectra have a strong absorption with fine detail at around 260 nm, and a broader absorption closer to 300 nm, both of which reduce in intensity with irradiation. This could suggest that the peaks correlate to the same transfers (e.g. 265 nm = N_3->Pt LMCT, and 300 nm = OH->Pt, N_3 LMCT, IL), however TDDFT calculations would need to be done to analyse this fully. Irradiation induced precipitation from solution and bubbles could be seen forming.

^{1}H NMR spectra taken of the solution before and after irradiation show an increase in the intensity of the residual water peak. As with *trans,trans,trans*-[Pt(*py*)$_2$(N$_3$)$_2$(OH)$_2$], this could be related to loss of the hydroxyl groups from the compound during irradiation. There is also a reduction in the intensity of the peaks corresponding to the pyrazine protons of approximately 56%, indicating that the concentration of the drug has reduced. Mass spectra taken before and after irradiation don't show any significant changes in the resonances present, apart from a reduction in intensity. The changes in both NMR spectra and mass spectra suggest that the decomposition products are precipitating, and are therefore not being detected by these analyses as they are filtered out.

2.3.3 *cis,cis,trans*-[Pt(*pz*)$_2$(N$_3$)$_2$(OH)$_2$]

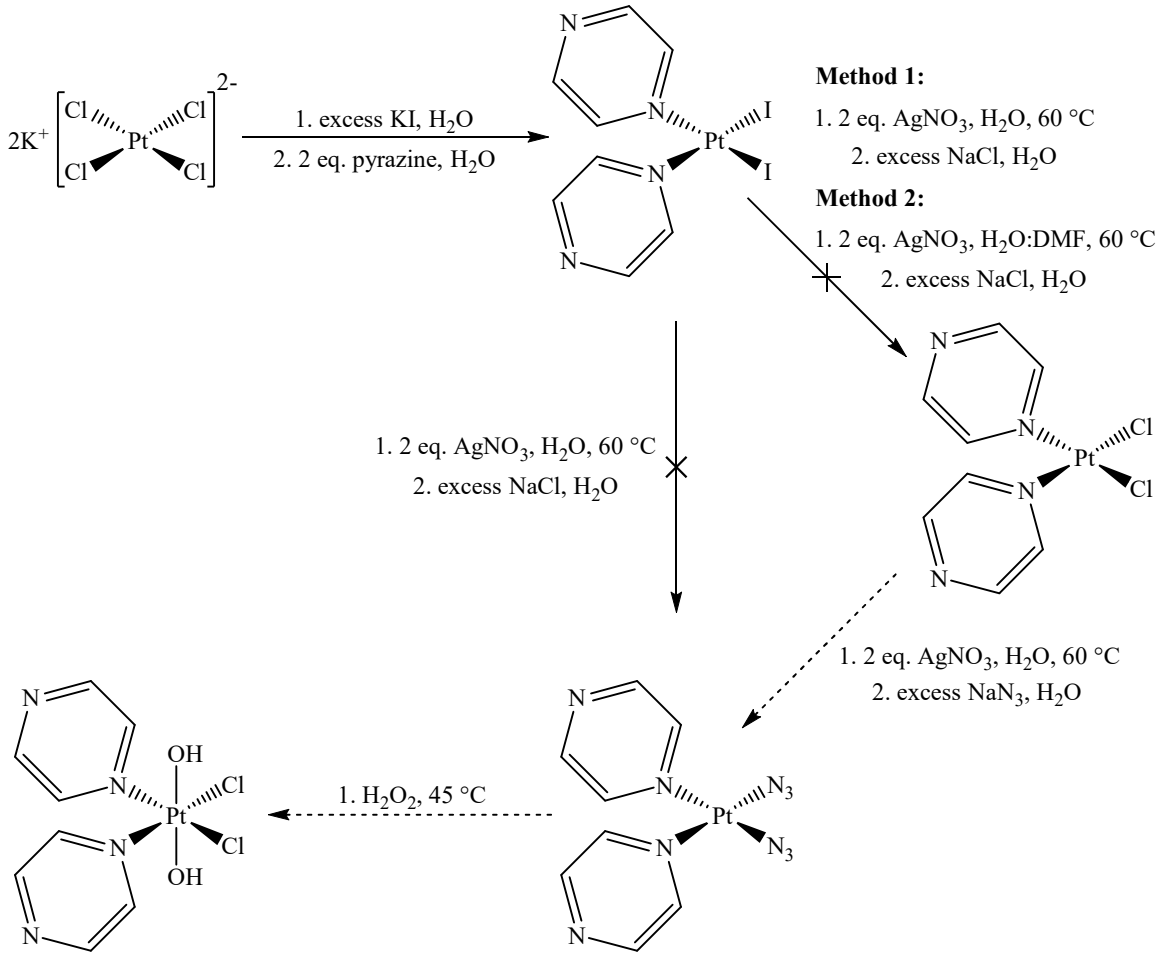

Figure 2.19 Schematic diagram showing the proposed multistep synthesis to produce c,c,t-[Pt(pz)$_2$(N$_3$)$_2$(OH)$_2$].

In order to compare the characteristics of *trans,trans,trans*-[Pt(*pz*)$_2$(N$_3$)$_2$(OH)$_2$] to the *cis*-isomer (*cis,cis,trans*-[Pt(*pz*)$_2$(N$_3$)$_2$(OH)$_2$]), synthesis of the latter was attempted. The synthetic route followed was the same as used to produce *cis,cis,trans*-[Pt(*tz*)$_2$(N$_3$)$_2$(OH)$_2$] (Figure 2.19). The first intermediate, *cis,cis*-[Pt(*pz*)$_2$I$_2$], was thought to have been made as the ^{1}H NMR spectrum showed the presence of two doublet of doublets, one with Pt satellites. The ^{13}C NMR did not show the presence of any compound peaks, with only the solvent references appearing on the spectrum. This may have been due to the NMR sample concentration being too low. No resonances were seen in the ^{195}Pt NMR spectrum. The mass spectrum also showed no relevant fragments, however this is not uncommon for Pt^{II} species. Based on the ^{1}H NMR spectrum, the

next synthetic step was attempted to produce *cis,cis*-[Pt(*tz*)$_2$Cl$_2$]. This was attempted initially in distilled water, and then in a mixture of distilled water and DMF, and just DMF. None of the attempts yielded a precipitate, and analyses of the reaction solution didn't show the presence of any products. An alternative method avoiding the dichloride intermediate and going straight to the Pt^{II} diazido complex was attempted. This was carried out in distilled water, and yielded a small amount of yellow precipitate. On analysis of the solid and the filtrate by NMR spectroscopy and mass spectrometry, no assignable product resonances could be seen. The products may not have been able to be synthesised due to steric hinderance between the two pyrazine ligands in a *cis*-conformation. The complications encountered in attempting to synthesise these Pt^{II} intermediates meant that the Pt^{IV} product, *cis,cis,trans*-[Pt(*pz*)$_2$(N$_3$)$_2$(OH)$_2$], could not be obtained.

2.4 Conclusions

Two novel Pt^{IV} complexes, *cis,cis,trans*-[Pt(*tz*)$_2$(N$_3$)$_2$(OH)$_2$] and *trans,trans,trans*-[Pt(*pz*)$_2$(N$_3$)$_2$(OH)$_2$], were synthesised reproducibly with good yields and showed aqueous solubility. Both complexes could be fully characterised by ^{1}H, ^{13}C and ^{195}Pt-NMR spectroscopy and mass spectrometry. These complexes also showed photoreduction when irradiated with blue light (405 nm), meaning they could potentially be used in photoactivated chemotherapy. Both complexes showed similar absorption and irradiation characteristics to the established compound *trans,trans,trans*-[Pt(*py*)$_2$(N$_3$)$_2$(OH)$_2$]. However, *cis,cis,trans*-[Pt(*tz*)$_2$(N$_3$)$_2$(OH)$_2$] showed the greatest change in λ_{max} with irradiation of all three compounds, indicating it may be the most photosensitive complex. Further investigations would need to be

carried out to better understand the mechanisms by which photoreduction is occurring, and the products it is yielding.

Despite several attempts, *cis,cis,trans*-[Pt(*pz*)$_2$(N$_3$)$_2$(OH)$_2$] could not be synthesised by the attempted methods. Future work would involve attempting this synthesis by alternative methods, varying factors such as; solvent system, temperature, reaction times, or reagent equivalents.

2.5 References

1 S. A. Cotton, *Chemistry of Precious Metals*, Blackie Academic & Professional, 1st edn., 1997.

2 F. R. Hartley, *Chem. Soc. Rev.*, 1973, **2**, 163–179.

3 N. J. Farrer, J. A. Woods, L. Salassa, Y. Zhao, K. S. Robinson, G. Clarkson, F. S. MacKay and P. J. Sadler, *Angew. Chemie - Int. Ed.*, 2010, **49**, 8905–8908.

4 L. Pendyala, J. W. Cowens, G. Chheda, S. P. Dutta and P. J. Creavne, *Cancer Res.*, 1988, **48**, 3533–3536.

5 L. Pendyala, B. S. Krishnan, J. R. Walsh, A. V. Arakali, J. W. Cowens and P. J. Creaven, *Cancer Chemother. Pharmacol.*, 1989, **25**, 10–14.

6 N. J. Wheate, S. Walker, G. E. Craig and R. Oun, *Dalt. Trans.*, 2010, **39**, 8113–8127.

7 V. H. Bramwell, D. Crowther, S. O'Malley, R. Swindell, R. Johnson, E. H. Cooper, N. Thatcher and A. Howell, *Cancer Treat. Rep.*, 1985, **69**, 409–416.

8 C. Sessa, J. Vermorken, J. Renard, S. Kaye, D. Smith, W. ten Bokkel Huinink, F. Cavalli and H. Pinedo, *J. Clin. Oncol.*, 1988, **6**, 98–105.

9 G. N. Hortobagyi, D. Frye, F. A. Holmes, V. Hug, G. Fraschini and A. U. Buzdar, *Cancer Treat. Rep.*, 1987, **71**, 1193–1195.

10 R. Abele, M. Clavel, S. Monfardini, U. Bruntsch, J. Renard, M. van Glabbeke and H. M. Pinedo, *Eur. J. Cancer Clin. Oncol.*, 1987, **23**, 387–389.

11 V. Lira-Puerto, A. Silva, M. Morris, R. Martinez, S. Groshen, F. Morales-Canfield, F. Tenorio and F. Muggia, *Cancer Chemother. Pharmacol.*, 1991, **28**, 391–396.

12 M. Clavel, S. Monfardini, S. Gundersen, S. B. Kaye, P. Siegenthaler, J. Renard, M. van Glabbeke and H. M. Pinedo, *Eur. J. Cancer Clin. Oncol.*, 1988, **24**, 1345–1348.

13 R. P. Castleberry, A. B. Cantor, A. A. Green, V. Joshi, R. L. Berkow, G. R. Buchanan, B. Leventhal, D. H. Mahoney, E. I. Smith and F. A. Hayes, *J. Clin. Oncol.*, 1994, **12**, 1616–1620.

14 R. Nitschke, C. Pratt, M. Harris, J. Krischer, T. J. Vietti, H. Grier, W. Kamps and S. Toledano, *Invest. New Drugs*, 1992, **10**, 93–96.

15 H. S. Friedman, J. P. Krischer, P. Burger, W. J. Oakes, B. Hockenberger, M. D. Weiner, D. Norris, A. H. Ragab and D. H. Mahoney, *J. Clin. Oncol.*, 1992, **10**, 249–256.

16 A. S. Goldenberg, D. Kelsen, J. Dougherty and G. Magill, *Invest. New Drugs*, 1990, **8**, 71–75.

17 R. Asbury, A. Kramer, M. Green, R. Qazi, R. Skeel and D. G. Haller, *Am. J. Clin. Oncol.*, 1988, **11**, 650–651.

18 H. Anderson, J. Wagstaff, D. Crowther, R. Swindell, M. J. Lind, J. McGregor, M. S. Timms, D. Brown and P. Palmer, *Eur. J. Cancer Clin. Oncol.*, 1988, **24**, 1471–1479.

19 E. Pantoja, A. Gallipoli, S. van Zutphen, S. Komeda, D. Reddy, D. Jaganyi, M. Lutz, D. M. Tooke, A. L. Spek, C. Navarro-Ranninger and J. Reedijk, *J. Inorg. Biochem.*, 2006, **100**, 1955–1964.

20 S. C. Dhara, *Indian J. Chem.*, 1970, **8**, 193–194.

21 R. C. Harrison, C. A. McAuliffe and A. M. Zaki, *Inorganica Chim. Acta*, 1980, **46**, 15–16.

22 C. F. J. Barnard, P. C. Hydes, W. P. Griffiths and O. S. Mills, *J. Chem. Res. Synopses*, 1983, **12**, 302–303.

23 G. Ermondi, G. Caron, M. Ravera, E. Gabano, S. Bianco, J. A. Platts and D. Osella, *J. Chem. Soc. Dalt. Trans.*, 2013, **42**, 3482–3489.

24 P. J. Bednarski, F. S. Mackay and P. J. Sadler, *Anticancer. Agents Med. Chem.*, 2008, **7**, 75–93.

25 Y. Zhao, J. A. Woods, N. J. Farrer, K. S. Robinson, J. Pracharova, J. Kasparkova, O. Novakova, H. Li, L. Salassa, A. M. Pizarro, G. J. Clarkson, L. Song, V. Brabec and P. J. Sadler, *Chem. Eur. J.*, 2013, **19**, 9578–9591.

26 R. Bonnett, in *Comprehensive Coordination Chemistry*, eds. J. A. McCleverty and T. J. Meyer, Elsevier Pergamon, Vol. 2., 2004, p. 944.

27 E. B. Hughes, H. H. G. Jellinek and B. A. Ambrose, *J. Phys. Chem.*, 1948, **53**, 410–414.

28 M. Chien, A. P. Grollman and S. B. Horwitz, *Biochemistry*, 1977, **16**, 3641–3647.

29 L. F. Povirk, M. Hogan and N. Dattagupta, *Biochemistry*, 1979, **18**, 96–101.

30 M. Van Beusichem and N. Farrell, *Inorg. Chem.*, 1992, **31**, 634–639.

31 U. Bierbach, Y. Qu, T. W. Hambley, J. Peroutka, H. L. Nguyen, M. Doedee and N. Farrell, *Inorg. Chem.*, 1999, **38**, 3535–3542.

32 G. McGowan, S. Parsons and P. J. Sadler, *Inorg. Chem.*, 2005, **44**, 7459–7467.

33 F. S. Mackay, S. A. Moggach, A. Collins, S. Parsons and P. J. Sadler, *Inorganica Chim. Acta*, 2009, **362**, 811–819.

34 H. Shi, C. Imberti and P. J. Sadler, *Inorg. Chem. Front.*, 2019, **6**, 1623–1638.

35 E. Shaili, L. Salassa, J. A. Woods, G. Clarkson, P. J. Sadler and N. J. Farrer, *Chem. Sci.*, 2019, **10**, 8610–8617.

36 N. Farrell, *Met. Ions Biol. Syst.*, 1996, **32**, 603–639.

37 B. Ellis and P. J. F. Griffiths, *Spectrochim. Acta*, 1965, **21**, 1881–1892.

38 E. Iengo, G. Mestroni, S. Geremia, M. Calligaris and E. Alessio, *J. Chem. Soc., Dalt. Trans.*, 1999, **4**, 3361–3371.

39 S. Jovanović, K. Obrenčević, Ž. D. Bugarčić, I. Popović, J. Žakula and B. Petrović, *Dalt. Trans.*, 2016, **45**, 12444–12457.

40 S. Komeda, G. V. Kalayda, M. Lutz, A. L. Spek, Y. Yamanaka, T. Sato, M. Chikuma and J. Reedijk, *J. Med. Chem.*, 2003, **46**, 1210–1219.

41 I. Vasić, S. Rajković, A. Arsenijević, M. Milovanović, N. Arsenijević, J. Milovanović and M. D. Živković, *J. Inorg. Biochem.*, , DOI:10.1016/j.jinorgbio.2021.111619.

42 M. Willermann, C. Mulcahy, R. K. O. Sigel, M. M. Cerdà, E. Freisinger, P. J. Sanz Miguel, M. Roitzsch and B. Lippert, *Inorg. Chem.*, 2006, **45**, 2093–2099.

43 G. A. Foulds and D. A. Thornton, *Spectrochim. Acta*, 1981, **37**, 917–921.

44 B. Samir, C. Kalalian, E. Roth, R. Salghi and A. Chakir, *Chem. Phys. Lett.*, 2020, **751**, 137469.

Chapter 3 Liposomes

3.1 Introduction

The following chapter discusses the use of dynamic light scattering (DLS) to ascertain which phosphatidylcholine lipid, and which method of liposome formation, yields the most monodisperse liposomal suspensions. The potential application of differential scanning calorimetry (DSC) for liposome analysis is also outlined. In depth experiments into optimising the liposomal encapsulation of the Pt^{IV} drug iproplatin are explored, and finally the use of cross-linkable lipids for improving drug retention in liposome formulations is considered.

The composition of liposomes used in this research was defined by previous studies conducted by Geers *et al,* and also by previous work undertaken within the Farrer group.[1,2] The composition consists of a phosphatidylcholine (PC), cholesterol, and 1,2-distearoyl-sn-glycero-3-phosphoethanolamine-N-[methoxy(polyethyleneglycol)-2000] (DSPE-mPEG(2000)) in the molar ratio 54:36:10 was used. The phosphatidylcholine was the variable component, with either 1,2-dipalmitoyl-sn-glycero-3-phosphocholine (DPPC), or 1,2-dibehenoyl-sn-glycero-3-phosphocholine (DBPC) being used. The inclusion of cholesterol increases rigidity, which decreases leakage, however it may also affect loading capacities.[3] DSPE-mPEG(2000) was used as the pegylated group is believed to help with 'stealthing' the liposomes in the blood stream, increasing the circulation time and also the probability of permeating the tumour tissue.[4,5] This formulation was also selected due its suitability for ultrasound triggered release, which was the intended application for this work.[1]

The structures of all lipids used in this work are included in appendix section A.1, and experimental methods for the liposome formulations are detailed in the experimental section.

3.2 Composition and characterisation

3.2.1 DBPC *vs.* DPPC

DLS allows for determination of the size distribution of molecules and particles in a suspension. It has been used in order to measure the size of the liposomes being produced. Figure 3.1 shows a plot of the data collected by DLS.

DLS was carried out on standard liposomes made using DPPC, cholesterol and DSPE-mPEG(2000) in the molar ratio 54:36:10 was tested. The same tests were also conducted on liposomes which had the same lipid ratio, but that used DBPC in place of DPPC. It was proposed that the longer chain of DBPC could reduce leakage of drugs from the liposomes, and therefore these experiments were conducted to test how this lipid may alter the properties of the liposomes. These suspensions were tested at 1 in 10 and 1 in 100 dilutions, diluting with calcium acetate (200 mM), as the sizing and distribution results can be skewed if the solution is too concentrated. This is due to the multiple scattering effect, in which light scattered from a single particle is re-scattered by neighbouring particles in the solution, leading to artificially low particle size results.[6]

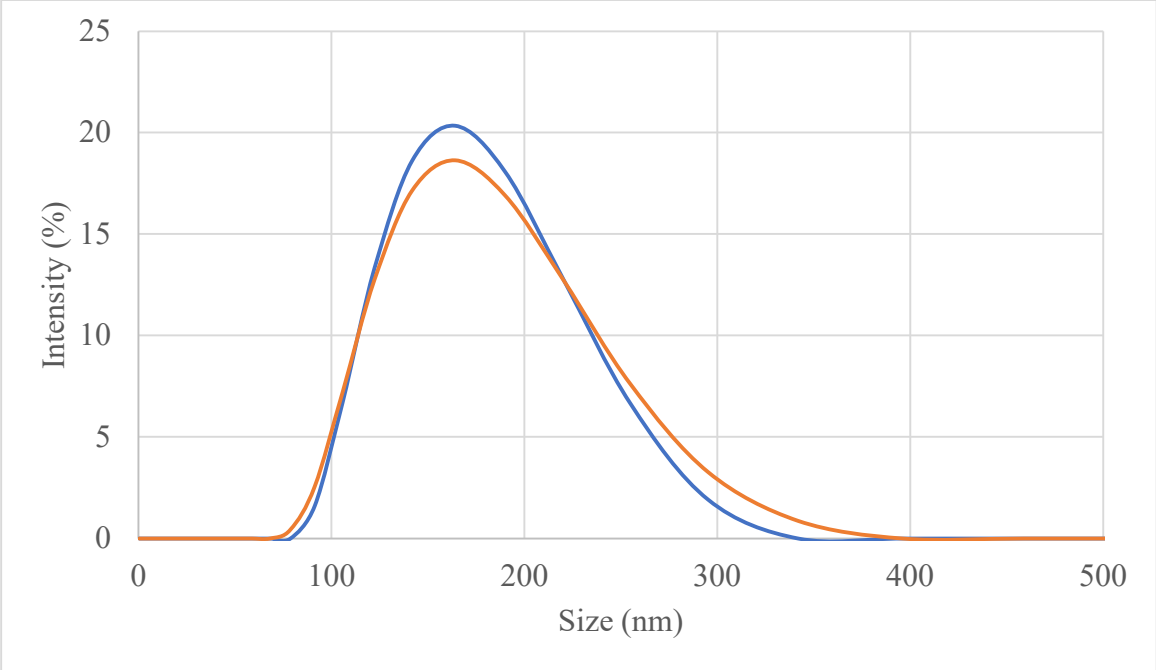

Figure 3.1 DLS size distribution for extruded DPPC containing liposomes; 1 in 10 dilution (blue), 1 in 100 dilution (orange).

The Z-Average value represents the average size of all species in each sample, and the PdI (polydispersity index) is a dimensionless value that measures the heterogeneity of a sample based on size. PdI can be calculated from DLS by Equation 1, where σ is the standard deviation and d is the mean diameter.[7]

$$PdI = \left(\frac{\sigma}{d}\right)^2 \qquad (1)$$

For a perfectly monodisperse suspension the PdI would be 0. A PdI value below 0.05 indicates a close to monodisperse suspension, whereas a value above 0.7 suggests the sample is highly polydisperse.[8]

DPPC			DBPC		
Dilution	Z-Average (nm)	PdI	Dilution	Z-Average (nm)	PdI
1 in 10	158.8	0.057	1 in 10	169.4	0.129
1 in 100	158.7	0.078	1 in 100	163.7	0.129

Figure 3.2 Comparing DLS results of DPPC and DBPC containing liposomes, formed by extrusion, at 1 in 10 and 1 in 100 dilutions with calcium acetate (200 mM).

The data collected (Figures 3.2 and 3.3) shows that the liposomes containing DPPC are slightly smaller in size than those containing DBPC, and that the suspension is also more monodisperse. It can therefore be concluded from the data that the DBPC containing liposomes exist in a broader range of sizes, and are therefore less uniform.

Difficulties were encountered in forming the DBPC containing liposomes by extrusion, as a higher extrusion temperature was needed because DBPC has a higher transition temperature (T_m). This is the temperature required to change the state of a lipid from the ordered gel phase, to the disordered liquid crystalline phase.[9] To counter this problem, an attempt was made to form the DBPC containing liposomes by sonication using a probe sonicator. Conditions used were 6 secs on, 4 secs off for 10 minutes at 30% amplitude. DLS was used in order to compare the DBPC samples formed by the different methods.

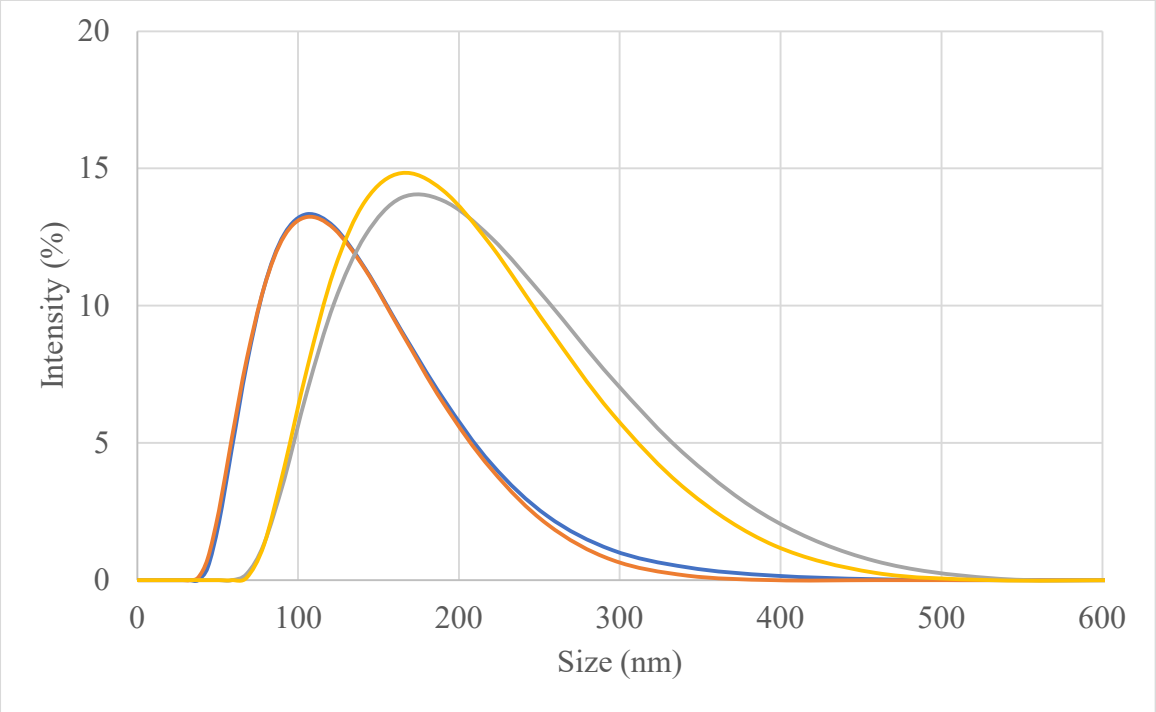

Figure 3.3 DLS size distribution for DBPC containing liposomes formulated by sonication (1 in 10 dilution - blue, 1 in 100 dilution - orange), and extrusion (1 in 10 dilution - grey, 1 in 100 dilution - yellow).

The data in Figure 3.4 shows that the sonication method forms significantly smaller liposomes than the extrusion method. As well as being smaller, the sonicated liposomes also have a slightly higher PdI, and therefore have a broader range of sizes than the extruded liposomes.

DBPC – sonicated			DBPC - extruded		
Dilution	Z-Average (nm)	PdI	Dilution	Z-Average (nm)	PdI
1 in 10	105.4	0.145	1 in 10	169.4	0.129
1 in 100	103.3	0.156	1 in 100	163.7	0.129

Figure 3.4 Comparing DLS results of DBPC containing liposomes, formed by sonication and extrusion, at 1 in 10 and 1 in 100 dilutions with calcium acetate (200 mM).

DPPC was easier to work with as the DBPC containing composition required an extrusion temperature of 75 °C, compared to 65 °C for DPPC containing liposomes. The extrusion block and syringes have to be manually handled, which would be difficult to manipulate with heat

proof gloves, and too hot to use without gloves (Figure 3.5). Based on the PdI results, and also on the ease of synthesis, a decision was made to continue producing the DPPC, DSPE-mPEG(2000) and cholesterol containing liposomes. The extrusion method was also selected, as the results suggest it provides a better uniformity of suspension.

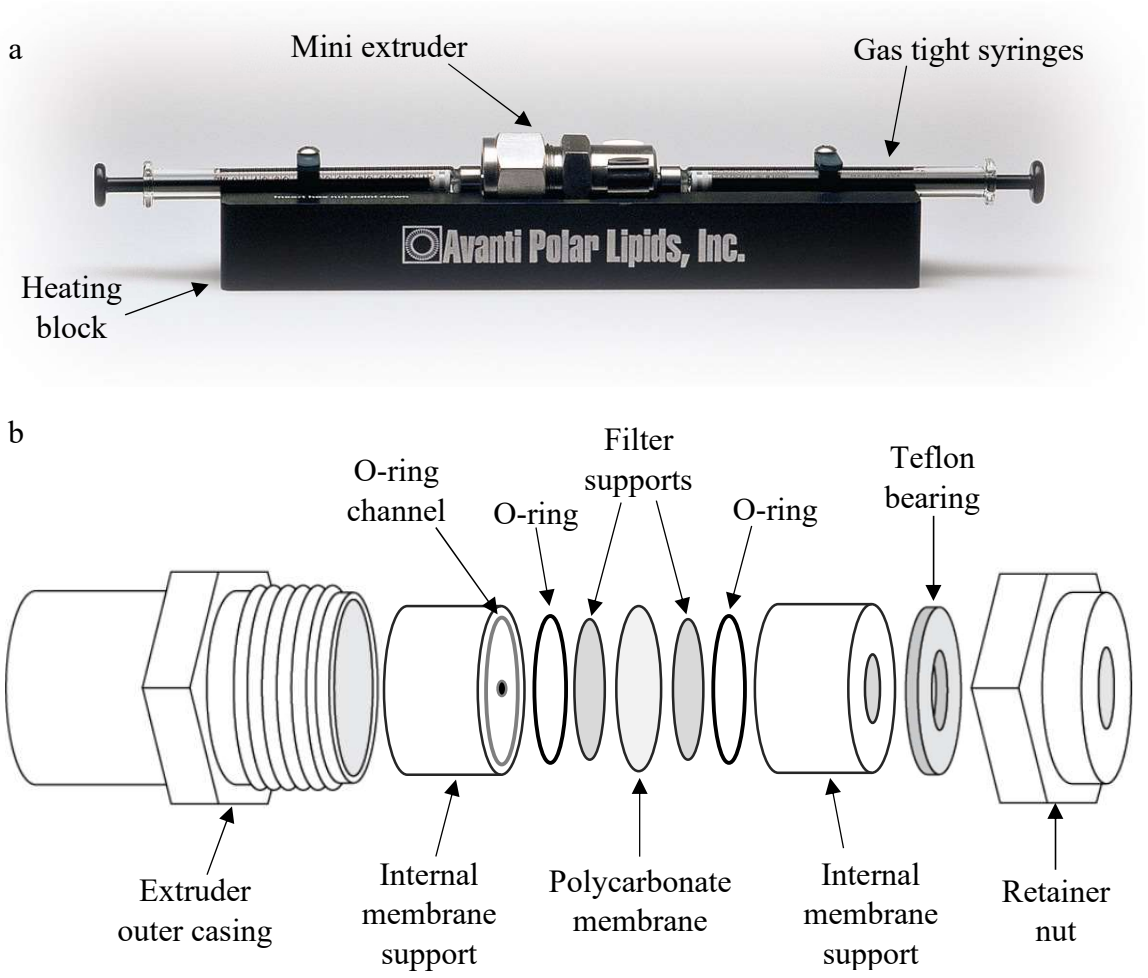

Figure 3.5 a) Image showing the Avanti Mini Extruder set up with heating block and gas tight syringes, b) Diagram showing the internal structure of the Avanti Mini Extruder.[10]

3.2.2 DSC for liposome characterisation

Differential scanning calorimetry (DSC) is used to determine the thermal properties of materials, and can therefore show the transition temperatures of phospholipid bilayers.[11]

DSC was investigated to see if it could be used as a method of analysis to prove that the intended liposomes were being formed. Assuming all lipids have individual thermal profiles, on formation of liposomes consisting of several different lipids, the transition profile of the liposomes should correlate to an average of the lipids present.

Initially, an attempt was made to measure the thermal profile of our standard liposomes which consist of DPPC, cholesterol and DSPE-mPEG(2000) in the molar ratio 54:36:10. The liposomes were tested in sodium sulphate solution (200 mM), but no thermal transitions were observed (Figure A4.1).

It was proposed that solvent effects from the surrounding medium could be interfering with the liposomes. To test this theory, DSC was carried out on the standard liposomes in calcium acetate (200 mM), as this is the suspension they are in before dialysis with sodium sulphate in order to set up the drug loading gradient. There were still no transitions seen in this second medium (Figure A4.2). It was decided that the individual solid lipids used in the liposome composition should be tested separately to measure their thermal profiles without interactions to each other, or to the intra- and extraliposomal mediums.

When the solid lipids were tested, transitions were seen for both cholesterol and DSPE-PEG2000, but not for DPPC. The traces for these tests are shown in Figure A4.3. For cholesterol, weak transitions are seen at 36 °C upon heating and 24 °C on cooling. For DSPE-PEG2000, strong transitions are seen at 49 °C on heating and 45 °C during cooling.

Liposomes were then formulated from the individual lipids, to assess whether the results were due to the solution and bilayers interfering (Figure A4.4). Only DPPC and DSPE-mPEG(2000) were tested in this manner, as it was not possible to formulate liposomes made purely from cholesterol. The results showed no transitions for the DSPE-mPEG(2000) liposomes, despite transitions having been observed when the lipid was in it's solid state. For the DPPC liposomes peaks were seen, however these were later identified as showing the melting point of DPPC rather than a phase transition.

3.3 Active loading and leakage

3.3.1 Iproplatin versus *trans,trans,trans*-[Pt(*py*)$_2$(N$_3$)$_2$(OH)$_2$]

Due to the therapeutically desirable properties of *trans,trans,trans*-[Pt(*py*)$_2$(N$_3$)$_2$(OH)$_2$], liposomal encapsulation of this compound was attempted in a preliminary investigation to see if it would be a viable drug to use in this system. The calcium acetate loading method was used, as this had been previously explored for iproplatin loading.[12] The initial loading for this drug in the formulated volume of liposomes (approx. 1.25 mL) was found to be 0.43 mg (2.9% efficiency from 15 mg incubation), in comparison to the average initial loading for iproplatin of 1.58 mg (10.5% efficiency). Because of the significantly higher loading efficiency of iproplatin, it was decided that further liposome studies would focus on iproplatin.

3.3.2 Comparing loading methods for iproplatin encapsulation

In previous work conducted by the group, passive and active loading methods were compared for the encapsulation of the anti-cancer drugs gemcitabine and iproplatin.[2] For both complexes, it was found that passive loading resulted in significantly lower loading, and was therefore not

a promising option. Active loading was therefore preferentially used for further studies.[12] This previous work only explored the use of the calcium acetate active loading method for iproplatin. An alternative method of active loading uses an ammonium sulphate / sodium chloride gradient. The method selected depends on whether the drug to be loaded behaves as an amphipathic weak acid (calcium acetate) or an amphipathic weak base (ammonium sulphate). Although it was assumed that iproplatin would behave as a weak acid, deprotonating at one of the amine groups, this thesis explores the use of both methods for the loading of iproplatin in order to determine which loading method will give the most optimal results.

Liposomes were formulated using the standard method described in the experimental section of this thesis, either using calcium acetate or sodium sulphate solutions for rehydration. These liposomes were loaded with iproplatin following the relevant method, and subsequently aliquots of these samples were collected daily after loading. Unencapsulated drug was removed from these samples by size exclusion, and the liposomes digested to release any drug that was still present in the intraliposomal matrix. Both loading methods were repeated in quintuplicate to assess the reproducibility of loading, and analysis was carried out by ICP-MS. This method of analysis provides the Pt concentration, which can be back-calculated to give the concentration of the drug. Analytical HPLC was previously used as the method of analysis for these experiments, however due to machine faults it was not possible to collect data for all samples, and so they had to be repeated via this new method.

Figures 3.6 and 3.7 show the average change, excluding anomalous values, in Pt concentration of the intraliposomal matrix plotted against the number of days since the liposomes were loaded. Experiments were run in quintuplicate, and averages of these five batches taken. The anomalies were attributed to contamination during sample preparation, and have been included

in the appendix (A.5). The Pt concentration values are the combined concentrations of the ^{194}Pt and ^{195}Pt isotopes in the test samples, which are dilutions of the original liposome samples due to the need for sample digestion and the testing ranges of the ICP-MS instrument. These isotopes are tested for as they have the highest natural abundances (32.864% and 33.775% respectively). These values can be used to extrapolate the total Pt concentration of all isotopes in the samples, and also the values for the concentrated initial solutions which gives the initial loading value. The blue line graph represents the standard composition liposomes loaded using the calcium acetate method, and the yellow line graph represents the standard composition liposomes loaded using the ammonium sulphate method. Points on the graphs at which the Pt concentration appears to increase with time (calcium acetate days 3 and 10, and ammonium sulphate days 4, 8 and 11) are due to variation in the individual batches, and the range of results from the five batches can be seen from the error bars. Points on the graphs without range bars are due to only one batch having a sample collected on those days.

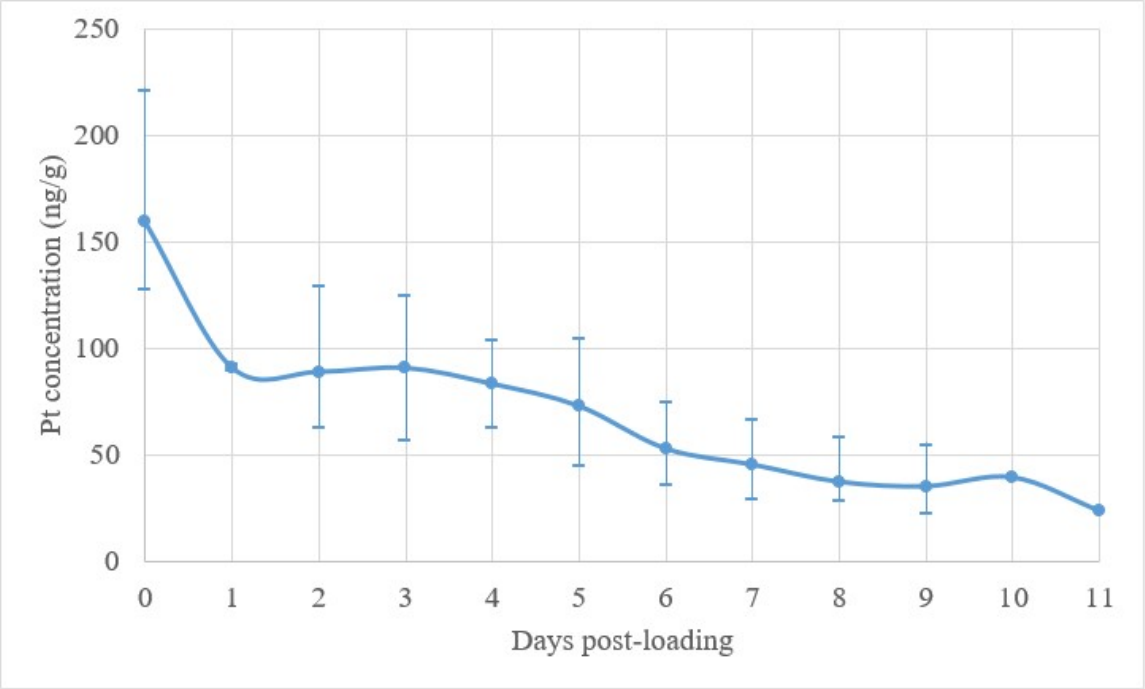

Figure 3.6 Change in Pt concentration of the intraliposomal matrix in the days after loading for standard calcium acetate liposomes.

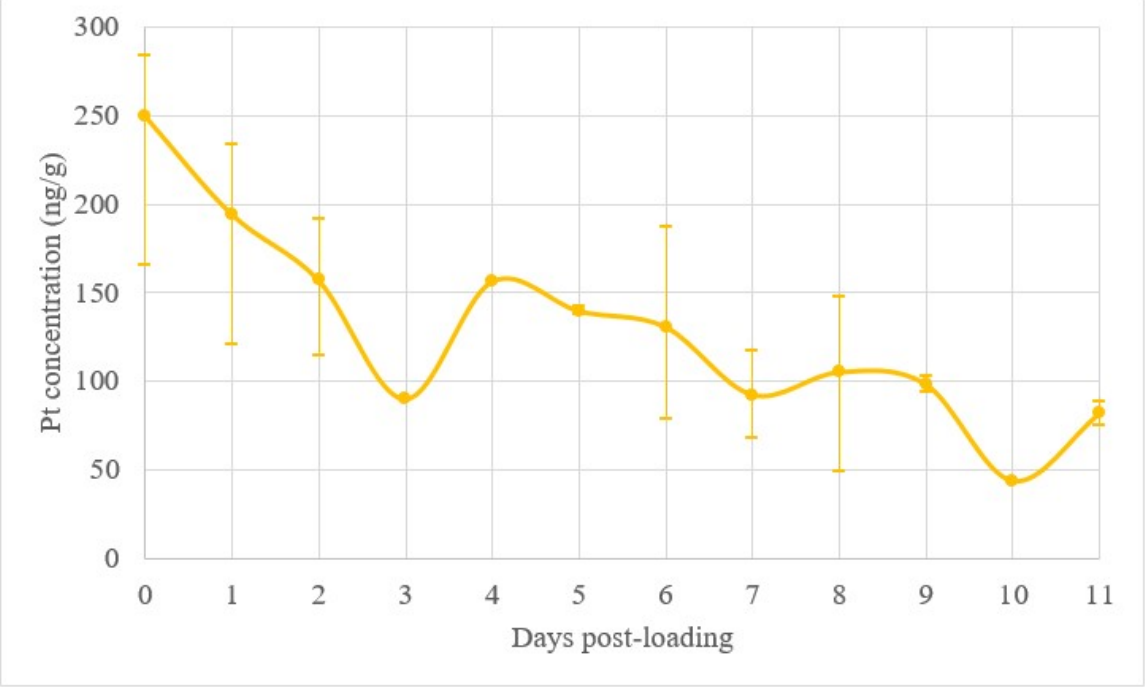

Figure 3.7 Change in Pt concentration of the intraliposomal matrix in the days after loading for standard ammonium sulphate liposomes.

The general trend for both sets of loading methods shows a decrease in the Pt concentration as the time since loading increases. This is concordant with the idea that the drug is passively leaking out of the liposomes, and agrees with previous work conducted. Comparison of the initial loading capacities shows that iproplatin is more successfully loaded using the ammonium sulphate method, with an average Pt concentration at day 0 of 250 ng g^{-1}. The average initial encapsulation calculated from this data for the calcium acetate loading method is 160 ng g^{-1}, approximately 90 ng g^{-1} less. These values, when converted back to the original concentrated samples and accounting for the presence of all isotopes, equate to an initial encapsulation of 1.02 mg mL^{-1} using calcium acetate and 1.61 mg mL^{-1} using ammonium sulphate. As a percentage of the amount of iproplatin used in the incubation step (15 mg), these are 8.5% and 13.4% respectively. The higher encapsulation using the ammonium sulphate method suggests that iproplatin is behaving as a weak base, rather than a weak acid. There is a reasonably large range between batches for the initial loading using both methods. The calcium acetate samples had a minimum initial loading of 128 ng g^{-1} and a maximum initial loading of 221 ng g^{-1}, giving a range of 93 ng g^{-1}. The ammonium sulphate samples had a minimum encapsulation of 165 ng g^{-1} and a maximum encapsulation of 284 ng g^{-1}, giving a range of 118 ng g^{-1}.

After 10 days there was an average of 0.22 mg mL^{-1} (21.5% of the initial encapsulation) remaining in the calcium acetate liposomes, and 0.56 mg mL^{-1} (34.9%) in the ammonium sulphate liposomes. This shows that using the ammonium sulphate method also leads to improved retention of the encapsulated drug. The ICP-MS data for the individual batches, including anomalous values, are included in in appendix A.5.

3.3.3 pK_a values and loading

Based on the idea that if the loaded complex behaves as a weak acid or a weak base, one loading method may be more suitable than the other, it was hypothesised that determining the pK_a of a compound could indicate which method might be more successful. This could mean that replicate loading experiments by boths methods would not need to be carried out to compare their efficiency.

In order to obtain pK_a values for the complexes in Chapter 2, ^{1}H-NMR titrations were carried out. A solution of the compound in D_2O (250 mg in 12 mL) was added to a clean conical flask. The solution was then acidified with 2 mL of a 1 M solution of hydrochloric acid prepared in D_2O. The pH was measured using a Hanna Instruments Pocket Checker pH Tester, and ^{1}H-NMR obtained using a Bruker Avance III HD nanobay NMR equipped with an 9.4 T magnet. The pH was then gradually raised using solutions of potassium hydroxide (1 M and 0.1 M) prepared in D_2O, and ^{1}H-NMR taken at each new pH reading. pK_a experiments were repeated in duplicate to assess the reproducibility of the results. The ^{1}H-NMR spectra were used to monitor the shift in the resonances for each compound. The chemical shift could then be plotted against the corresponding pH to give a titration curve, with a best fit derived from the Henderson-Hasselbalch equation (Equation 2). It is worth noting that the different protons on each compound could shift by varying degrees, with some protons not showing any significant shift.

$$pH = pK_a + log\left[\frac{(y_{max} - y)}{(y - y_{min})}\right] \qquad (2)$$

y is the experimentally measured paramter (chemical shift), with y_{max} representing the highest chemical shift and y_{min} representing the lowest chemical shift, and where $(y_{max} - y) \propto$

$[A^-]$ and $(y - y_{min}) \propto [HA]$. In order to plot the best fit data set, equation 1 must be recast in the form $y = f(x)$ (Equation 3).[13,14]

$$y = y_{min} + \frac{(y_{max} - y_{min})}{(1 + 10^{(pH \quad a)})} \qquad (3)$$

The pK_a value for this equation is found from the equivalence point, where it is equal to the pH value, of the original plotted data set. Data for all complexes was plotted using Microsoft Excel.

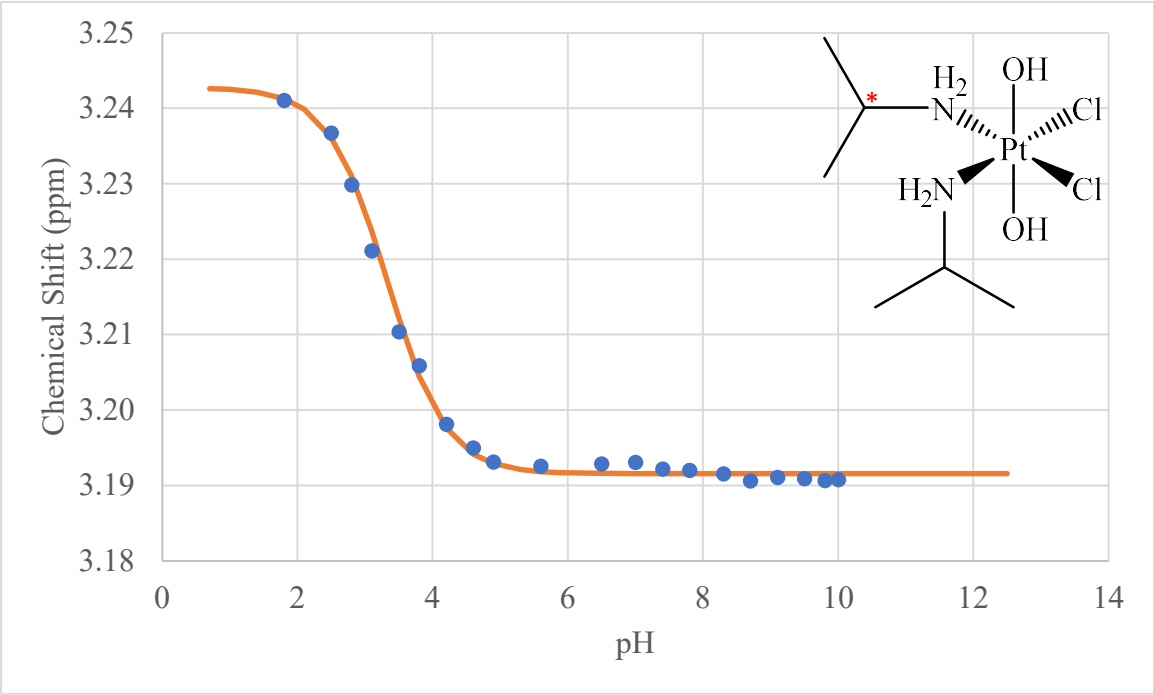

Figure 3.8 Change in chemical shift for the CH resonance (proton marked on compound structure) of iproplatin with changing pH. The blue markers show the measured data, and the orange line shoes the best fit.

Figure 3.8 shows the change in chemical shift of the resonance corresponding to the CH proton in the isopropylamine ligand on iproplatin. The blue marks are the measured data, and the orange line shows the best fit. The plotted data yields a pK_a^* (the pK_a measured in D_2O) of 3.36. The binding affinities of D^+ and H^+ are different and therefore it would result in different acidities. pK_a^* can be converted into the pK_a value using the relationship in Equation 4.[15]

$$pK_a = pK_a^* \times 0.929 + 0.42 \qquad (4)$$

This gives a pK_a for iproplatin of 3.54 in H_2O, which is likely to correspond to protonation of the hydroxyl groups at low pH. The CH_3 protons on the isopropylamine ligands did not show a shift with the changing pH, and the hydroxyl and amine protons were masked by the D_2O solvent peak. It was hypothesised that the mechanism of action for liposomal loading would be proton loss at either the NH_2 group, or the hydroxyl group. These mechanisms correspond to acidic behaviour, which correlates to the pK_a value, but does not fit the improved loading by the ammonium sulphate method. It is therefore likely that the most efficient loading method depends on multiple factors, rather than just the pKa values for the complexes.

These pK_a studies were carried out on the other complexes described in Chapter 2. For *t,t,t*-[Pt(*py*)$_2$(N$_3$)$_2$(OH)$_2$], the chemical shifts for the meta and para protons on the pyridine ligands were mapped. The ortho protons did not show a change in chemical shift, and the hydroxyl proton resonances were masked by the D_2O solvent peak. Averaging the replicate experiment results, the meta and para protons yielded pK_a values in H_2O of 2.45 and 2.44 respectively. This gives an average pK_a value of 2.45, which is again likely to correspond to protonation at the hydroxyl at low pH. Proton exchange at this group is the most likely mechanism involved during active liposomal loading.

Mapping the change in shift of the thiazole ligand protons in the complex *c,c,t*-[Pt(*tz*)$_2$(N$_3$)$_2$(OH)$_2$] yielded slightly different pK_a values depending on the proton. The values calculated for H_2O were 3.01 for the NCS proton, 3.03 for the SCC proton, and 3.10 for the CCN proton. This gives an average pK_a value of 3.05. Again, the hydroxyl group resonance was not seen in the ^{1}H NMR spectra due to the analysis being conducted in D_2O. The

mechanisms occurring during active loading are most likely to involve proton exchange at the hydroxyl groups, however protonation at the thiazole sulphur could be possible.

Finally, for *t,t,t*-[Pt(*pz*)$_2$(N$_3$)$_2$(OH)$_2$] chemical shifts were only seen for the ortho pyrazine protons, with the hydroxyl proton resonances masked by the D_2O solvent peak. This gives a pK_a of 2.21 in H_2O, which at the low pH likely relates to protonation of the hydroxyl group. The proton exchange involved in the liposomal loading is most likely to occur at the hydroxyl groups, however protonation at the para nitrogen is feasible.

3.4 Cross-linked liposomes

One of the main issues encountered with liposomal encapsulation is the retention of the drug. Due to the 'leaky' nature of the bilayer, small molecules such as iproplatin are able to diffuse out of the liposomes, and previous work has shown this process to happen rapidly within a couple of days of loading.[2] One proposed method of improving this retention is to cross-link within the liposomal shell. This can be done by inclusion of a diacetylene containing lipid in the liposome composition, which can be polymerised by irradiation with UV-light (Figure 3.9).[16,17]

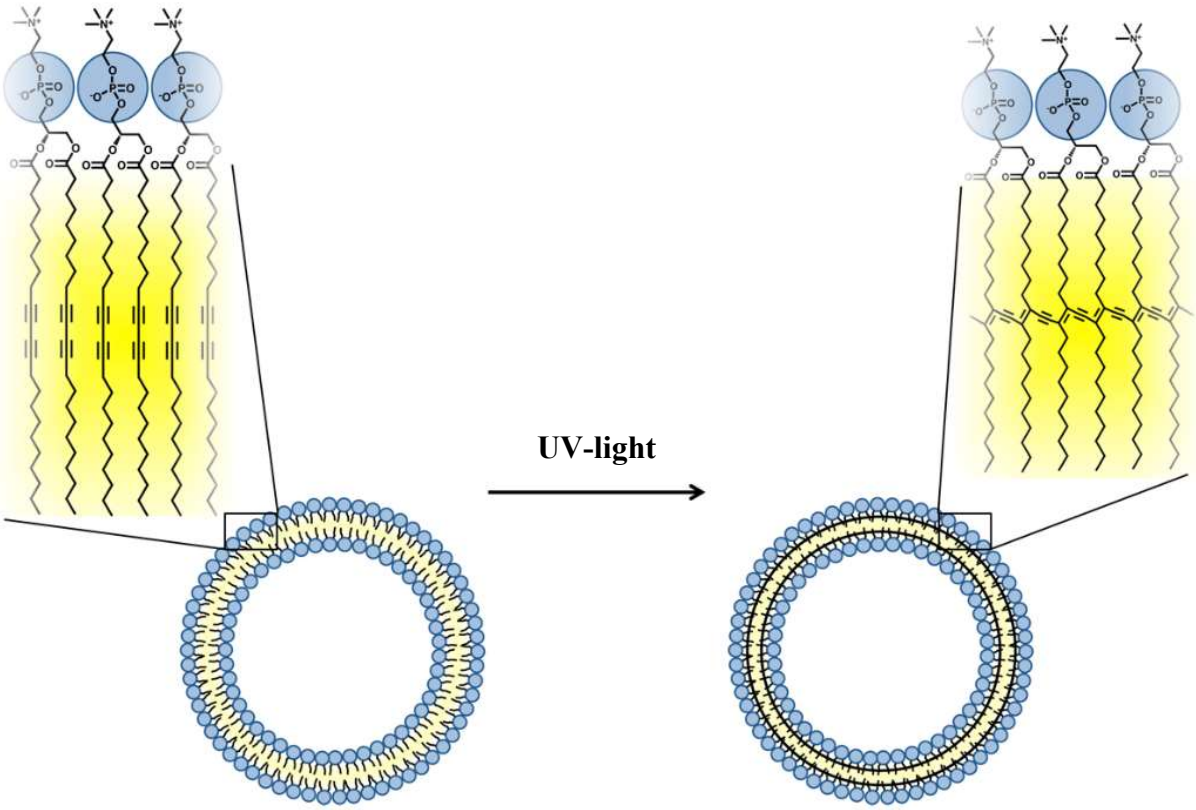

Figure 3.9 Diagram showing the cross-linking of 23:2 Diyne PC within a liposomal shell (adapted from Smith & Kong).[16]

This method was explored for our liposome system in collaboration with Prof. Steve Evans' group at the University of Leeds. Liposomes consisting of DPPC, 1,2-bis(10,12-tricosadiynoyl)-sn-glycero-3-phosphocholine (23:2 Diyne PC), cholesterol, and DSPE-mPEG(2000) in the ratio 27:27:36:10 were formulated. These liposomes were then irradiated with UV light (254 nm, 48 W) for various lengths of time, and monitored by Raman spectroscopy to look at the extent of polymerisation. The experiment was then repeated with drug loaded liposomes to see if this impacted the cross-linking, results of which are shown in Figure 3.10. The literature suggested that as the cross-linking occurred, Raman spectroscopy would show peaks at 1510 cm^{-1} and 2100 cm^{-1} (corresponding to the C=C and C≡C bonds in the polymerised 23:2 Diyne PC).[18] It was also anticipated that excessive irradiation would lead

to the formation of pores in the bilayer, accompanied with a decrease in intensity of the relevant peaks in the Raman spectra.[19]

Raman spectroscopy of polymerisation for both the empty and drug loaded liposomes confirmed the expected trend, with the intensity of the peaks at 1510 cm^{-1} and 2100 cm^{-1} increasing up to 40 minutes before starting to decrease with the formation of pores. All future irradiation studies used this length of irradiation. Iproplatin is highly coloured and absorbs at ca. 250 nm, so an attempt was made to study the encapsulation and leakage of iproplatin from these cross-linked liposomes using quantitative UV-Vis spectroscopy. Unfortunately, due to the presence of several lipids and Triton-X 100 (used in liposome digestion) which absorb in a similar region, this method of analysis was unsuccessful. Further experiments looking at the encapsulation and leakage of iproplatin from this cross-linked system were carried out and analysed using ICP-MS.

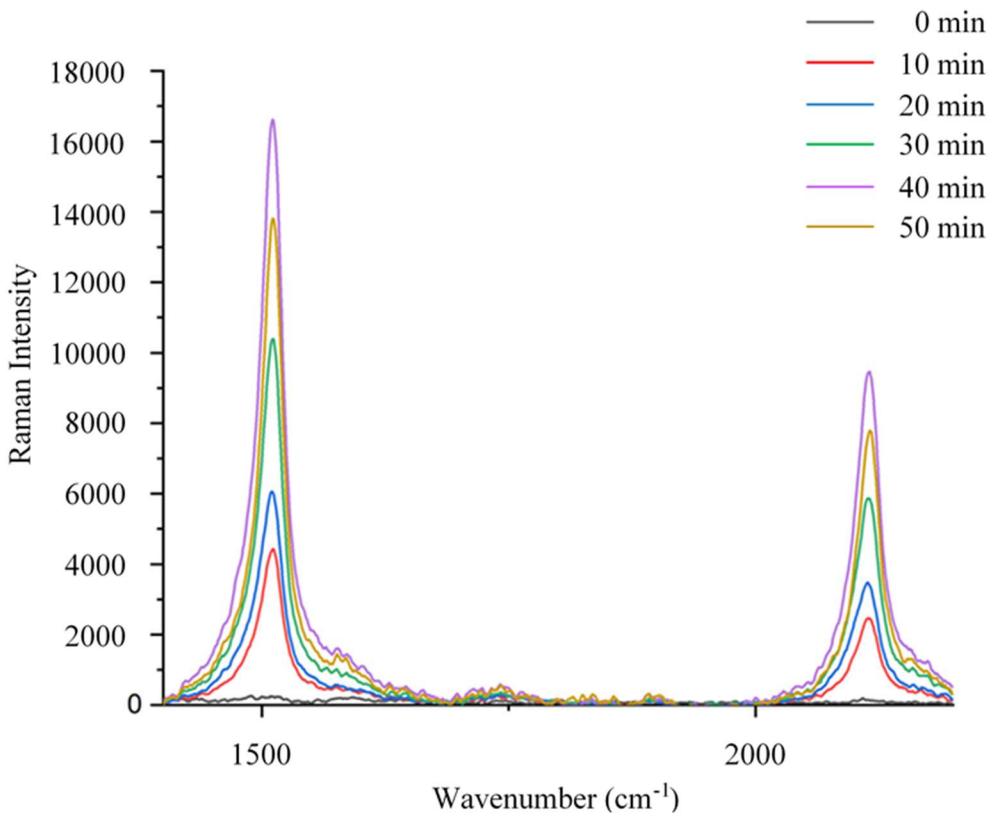

Figure 3.10 Raman spectra of Iproplatin loaded diyne-containing liposomes during UV irradiation.

To assess the loading and leakage of these cross-linkable liposomes, studies were carried out in a similar manner to those used for the standard liposome formulations. Batches of liposomes were formulated in quintuplicate using the previously mentioned 23:2 Diyne PC containing composition, and either the calcium acetate or ammonium sulphate loading methods. The synthesis of the cross-linked liposomes is the same as the standard liposomes up until the drug has been loaded. After incubation, the liposomes were cleaned by sephadex column to remove unencapsulated drug, and then they were irradiated with UV-light. Due to only having access to a lower power UV-lamp (254 nm, 28 W) than the one used for the work in Leeds, the time of irradiation was increased from 40 mins to 70 mins. After irradiation the liposomes were then cleaned again. Samples were taken before and after irradiation to assess whether the exposure to UV would have any immediate impact on the drug encapsulation.

Figures 3.11 and 3.12 show the average change in Pt concentration of the intraliposomal matrix plotted against the number of days since the liposomes were loaded. As before, the Pt concentration values are the combined concentrations of the ^{194}Pt and ^{195}Pt isotopes in the diluted test samples. Experiments were run in quintuplicate, and so the averages are from all five batches, but with anomalous values removed. The individual batches and anomalous values can again be seen in appendix A.5.

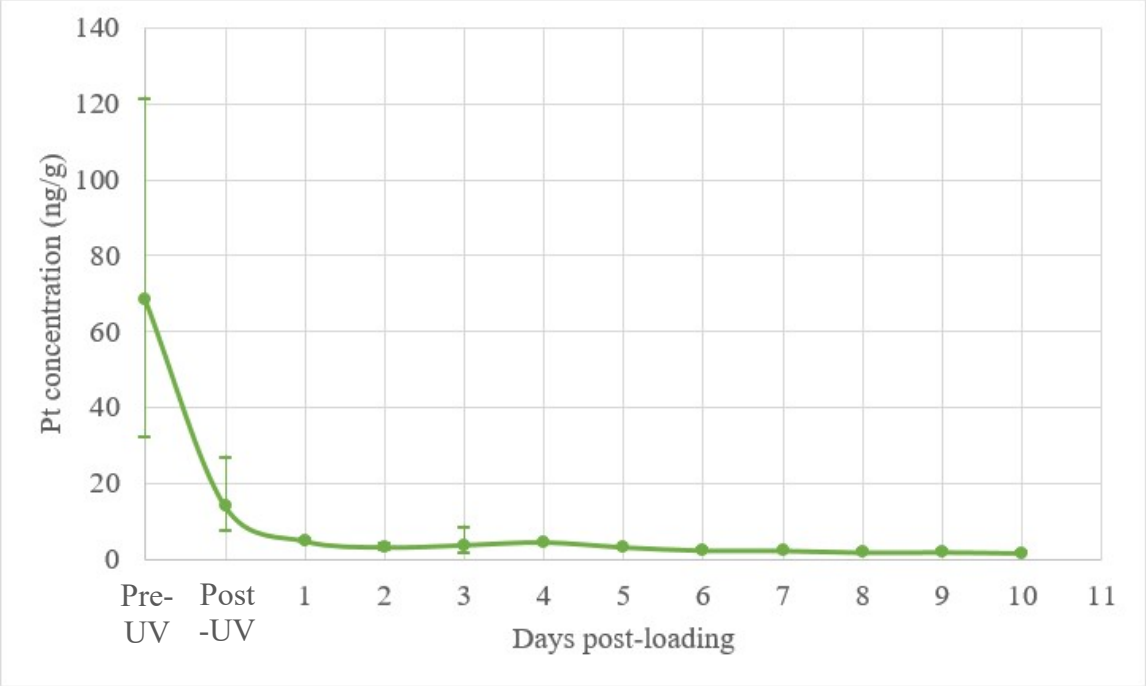

Figure 3.11 Change in Pt concentration of the intraliposomal matrix in the days after loading for cross-linked calcium acetate liposomes.

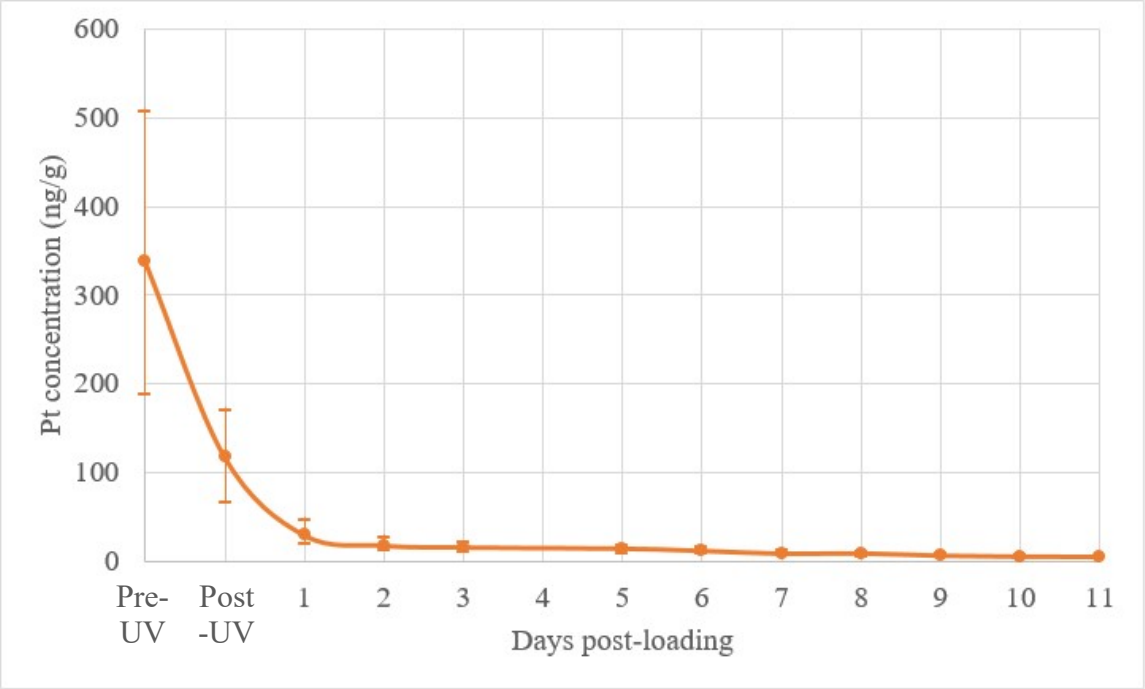

Figure 3.12 Change in Pt concentration of the intraliposomal matrix in the days after loading for cross-linked ammonium sulphate liposomes.

The general trend for all batches from both sets of loading methods again shows a decrease in the Pt concentration as the time since loading increases, however with these cross-linked liposomes it appears that the majority of the drug is being lost during the irradiation process, as the biggest decresase in Pt concentration occurs between the pre- and post-UV points (a 65.2% decrease for the ammonium sulphate liposomes, and a 79.4% decrease for the calcium acetate liposomes). This could suggest that the UV is potentially decomposing the drug, and the products of this decomposition are effluxing. Comparison of the initial loading capacities shows that iproplatin is more successfully loaded using the ammonium sulphate method, with an average Pt concentration before irradiation of 339 ng g^{-1}. The average initial encapsulation calculated from this data for the calcium acetate loading method is 68 ng g^{-1}, approximately 270 ng g^{-1} less. These values, when converted back to the original concentrated samples and accounting for the presence of all isotopes, equate to an initial encapsulation of 0.44 mg mL^{-1}

using calcium acetate and 2.18 mg mL^{-1} using ammonium sulphate. As a percentage of the amount of iproplatin used in the incubation step, these are 3.7% and 18.1% respectively. The higher encapsulation using the ammonium sulphate method reinforces the idea that iproplatin is behaving as a weak base. Again, there is quite a large range for the initial loading for both methods. The calcium acetate samples had a minimum initial loading of 32 ng g^{-1} and a maximum initial loading of 121 ng g^{-1}, giving a range of 89 ng g^{-1}. The ammonium sulphate samples had a minimum encapsulation of 188 ng g^{-1} and a maximum encapsulation of 507 ng g^{-1}, giving a range of 319 ng g^{-1}.

After 10 days there was an average of 0.01 mg mL^{-1} (2.9% of the initial encapsulation) remaining in the calcium acetate liposomes, and 0.03 mg mL^{-1} (1.6%) in the ammonium sulphate liposomes. This shows that the retention by both methods is incredibly poor, with negligible amounts of iproplatin being retained in either formulation. The ICP-MS data for the individual batches, including anomalous values, are included in in appendix A.5

3.5 Conclusions

Based on the results of the DPPC versus DBPC experiments, the composition that used DPPC was selected. This was both due to it being an easier composition to work with, requiring an extrusion temperature of 65 °C rather than 75 °C, and because the liposomes formed were much more monodisperse. Even when using sonication to synthesise the DBPC containing liposomes, which would have been preferable to the high temperature extrusion, the suspensions formed had a higher polydispersity index and the liposomes formed were significantly smaller than those formed by extrusion. The consistency and reproducibility of the DPPC containing liposomes was thought to be a favourable characteristic for being able to

monitor the drug loading and leakage without having too many variables. Although no attempts were made to produce the DPPC containing liposomes by sonication, the extrusion method was reproducable and produced good liposomal suspensions, and so due to the fact previous work had used these liposomes with success they were carried through to this work.

For analysis of liposomes, it was found that using DSC was not a viable method. No transitions were seen during analysis of the complete liposomes, and even if this was due to interference from the matrices, it would not be possible to avoid this interfence during analysis of samples. DLS had previously been successfully used to analyse and characterise the liposomes, and this was therefore kept as the preferred method.

From the analysis of drug loading and leakage from the standard composition liposomes, it can be stated that using an ammonium sulphate loading method leads to better initial encapsulation and better retention of the Pt^{IV} drug iproplatin. This implies that during the loading, iproplatin behaves as a weak base, though it is uncertain at which position on the complex this behaviour is arising from. Analysis of the loading and leakage from cross-linked liposomes also suggests that the ammonium sulphate method results in the highest loading, with the highest initial loading of iproplatin occurring for the ammonium sulphate method in cross-link composition liposomes. UV-Vis analysis for iproplatin carried out prior to this work showed no change in the spectra with varying lengths of UV exposure (254 nm), when measured across 350 to 800 nm wavelength. This is why it was thought that iproplatin would be compatible with the cross-linked liposomes. Repeat experiments, carried out after the liposomal loading work, looked at the absorption from 200 to 800 nm and showed that the absorption intensity between 200 and 300 nm decreased with exposure to blue light (405 nm). This indicates that iproplatin is photoreducible, and had this been known prior the the encapsulation work, a different

method of cross-linking would have been undertaken. The downside of the cross-linked liposomes is that the majority of the encapsulated drug is lost immediately after UV-exposure. This means that the retention is actually inferior than that of the standard composition liposomes. One of the most notable results from all of the different liposome batches formulated, was that the initial loading is not reproducible, despite the synthesis being kept as consistent as possible. This variation could mean that the composition wouldn't be clinically viable, as the amount of drug being delivered might not be the same for the same volume of different batches, however because industrial scale synthesis is carried out by machine this may give better uniformity. The poor retention also means that the liposomes would have to be administered shortly after loading as the solutions would not be usable after the first day. Finally, the amount of iproplatin being encapsulated, even in the most successful method and composition, is modest. This would mean that the volume of the suspension needing to be administered would be incredibly high. Although this might be feasible, clinical trials would need to be done to assess the side effects, and if the drug can be administered in smaller volumes by current methods then this might be preferable.

The experimental pK_a value for iproplatin was found to differ from what was hypothesised, based on liposome loading being more successful by the ammonium sulphate method. It is likely that the efficacy of a loading method for a complex depends on multiple factors, and therefore determination of pK_a cannot be used as the sole predictor.

Although not thoroughly studied, brief experiments suggest that *trans,trans,trans*-$[Pt(py)_2(N_3)_2(OH)_2]$ can not be loaded into our standard composition liposomes with sufficient encapsulation or retention using the calcium acetate method. Further work would need to be done to assess whether other compositions and loading methods were compatible with this

complex. For example, attempting loading using the ammonium sulphate method instead of the calcium acetate method. This compound would not be compatible with the cross-lined liposomes as it is highly photoreducible, and would therefore not withstand the exposure to UV-light.

3.6 References

1 B. Geers, I. Lentacker, N. N. Sanders, J. Demeester, S. Meairs and S. C. De Smedt, *J. Control. Release*, 2011, **152**, 249–256.

2 N. Thomas, University of Oxford, 2018.

3 A. Schroeder, J. Kost and Y. Barenholz, *Chem. Phys. Lipids*, 2009, **162**, 1–16.

4 O. Garbuzenko, S. Zalipsky, M. Qazen and Y. Barenholz, *Langmuir*, 2005, **21**, 2560–2568.

5 D. Papahadjopoulos, *J. Liposome Res.*, 1996, **6**, 3–17.

6 R. Ragheb and U. Nobbmann, *Sci. Rep.*, 2020, **10**, 1–9.

7 NanoComposix, *NanoComposix's Guid. to Dyn. Light Scatt. Meas. Anal.*, 2015.

8 T. Mudalige, H. Qu, D. Van Haute, S. M. Ansar, A. Paredes and T. Ingle, in *Nanomaterials for Food Applications*, Elsevier Inc., 2018, pp. 313–353.

9 W. Chen, F. Dusa, J. Witos, S. K. Ruokonen and S. K. Wiedmer, *Sci. Rep.*

10 Equipment - Avanti Polar Lipids.

11 M. Bastos, *Malvern Instruments Ltd.*, 2016.

12 R. Browning, N. Thomas, L. K. Marsh, L. R. Tear, J. Owen, E. Stride and N. J. Farrer, *Chem. Open*, 2021, **10**, 1–8.

13 M. Wallace, D. J. Adams and J. A. Iggo, *Anal. Chem.*, 2018, **90**, 4160–4166.

14 T. P. Silverstein, *J. Chem. Educ.*, 2012, **89**, 1474–1475.

15 A. Kręzel and W. Bal, *J. Inorg. Biochem.*, 2004, **98**, 161–166.

16 C. E. Smith and H. Kong, *Langmuir*, 2014, **30**, 3697–3704.

17 R. D. Ortuso, U. Cataldi and K. Sugihara, *Soft Matter*, 2017, **13**, 1728–1736.

18 A. Kenaan, J. Cheng, D. Qi, D. Chen, D. Cui and J. Song, *Anal. Chem.*, 2018, **90**, 9487–9494.

19 A. Yavlovich, A. Singh, R. Blumenthal and A. Puri, *Biochim. Biophys. Acta - Biomembr.*, 2011, **1808**, 117–126.

Chapter 4 Microbubbles and Ultrasound

4.1 Introduction

As outlined in Chapter 1, the ability to conjugate drug filled liposomes to the surface of microbubbles has been explored as a method of improving both targeting and efficacy of drug delivery.[1,2] These systems, when used in conjunction with ultrasound exposure, have been shown to improve drug release and cellular uptake, and have already been used in the delivery of doxorubicin.[3–5] Previous work showed the strain promoted azide-alkyne cycloaddition (SPAAC) method of conjugation, involving both preformed liposomes and microbubbles, to be successful in bonding drug filled liposomes to the surface of microbubbles.[6] The method used in this work required incubation times in excess of 18 hours, and therefore a more efficient method might be preferable. This chapter will briefly explore one possible alternative method of conjugation.

Using these systems as a means of delivery for the compounds discussed in Chapter 2, would require ultrasound exposure and therefore it would be preferable for the complexes to be stable under sonication so that they were not prematurely reduced to the active Pt^{II} species or to decomposition products. The stability of these compounds when exposed to relevant ultrasound conditions is discussed in this chapter.

Finally, the exploitation of sonoluminescence as a method of activation for a photoreducable Pt^{IV} prodrug is assessed.

4.2 Conjugated microbubble-liposome systems

One possible alternative to the previously used method involves forming azide-functionalised liposomes, clicking these to a DBCO-functionalised lipid, and then adding this system to the other lipids that make up the microbubbles before forming the bubbles.[7] This method was applied to the liposome-microbubble system used in this research, with the standard DSPE-mPEG(2000) in our liposomes replaced with 1,2-distearoyl-sn-glycero-3-phosphoethanolamine-N-[azido(polyethylene glycol)-2000] (DSPE-mPEG(2000) azide). The azide functionalised liposomes were incubated with 1,2-distearoyl-sn-glycero-3-phosphoethanolamine-N-[dibenzocyclooctyl(polyethyleneglycol)-2000] (DSPE-mPEG(2000)-DBCO) at RT for 2 h for the click reaction to occur. The liposomes were then added to 1 mL of a solution of DSPC and DSPE-mPEG(2000) (molar ratio 9:0.5) in Ungers solution (PBS:propylene glycol:glycerol, 8:1:1). The ratio of liposomes to microbubbles was varied, with a low concentration sample of 1:40 and a high concentration sample of 1:4 (liposomes:microbubbles, v/v), and all samples were made up to 1.5 mL using Ungers solution. The microbubbles were formed by agitation (capsule mixer, 45 s) using perfluorobutane for the heavy gas core, imaged with a Brightfield microscope, and characterised using image analysis software. The inclusion of 3,3'-dioctadecyloxacarbocyanine perchlorate (DiO) in the liposome formulation allowed for analysis by fluorescence microscopy, with a batch of blank microbubbles being used as the control.

For the sample with the higher concentration of liposomes, fluorescence microscopy appeared to show that the liposomes were clicked to the microbubbles surface as circular details could be seen on the fluorescence images corresponding to the DiO-containing liposomes. Figure 4.1 shows the fluoresecence microscopy, confocal microscopy, and overlaid images for an area of

the sample. One of the bubbles has been highlighted with an arrow to show its appearance in the confocal image, and how the circular fluorescence detail can be seen overlapping with its location. There also appeared to be a significant amount of fluorescence not associated with the microbubbles, which could correlate with excess liposomes remaining in the suspension.

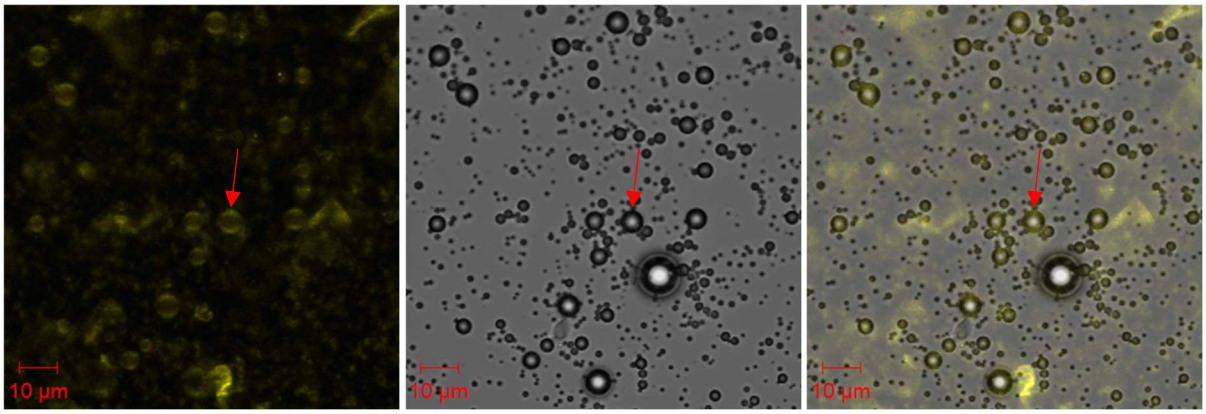

Figure 4.1 Imaging of the 1:4 sample, left to right: fluorescence microscopy, confocal microscopy, overlaid images.

At lower liposome concentrations only very small traces of fluorescence could be seen, with no correlation to the location of the microbubbles (Figure 4.2). A bubble visible in the confocal image has been highlighted with an arrow, however there is no associated fluorescence. This suggests that all the liposomes were removed during the washing phase. If this is the case, at higher concentrations the liposomes may possibly have been adhering to the microbubble surface, without actual integration of the DSPE-PEG(2000)-DBCO in to the microbubble shell. It is also feasible that the concentration of liposomes had been reduced too much, and that the optimum ratio may lay in between the two analysed variations.

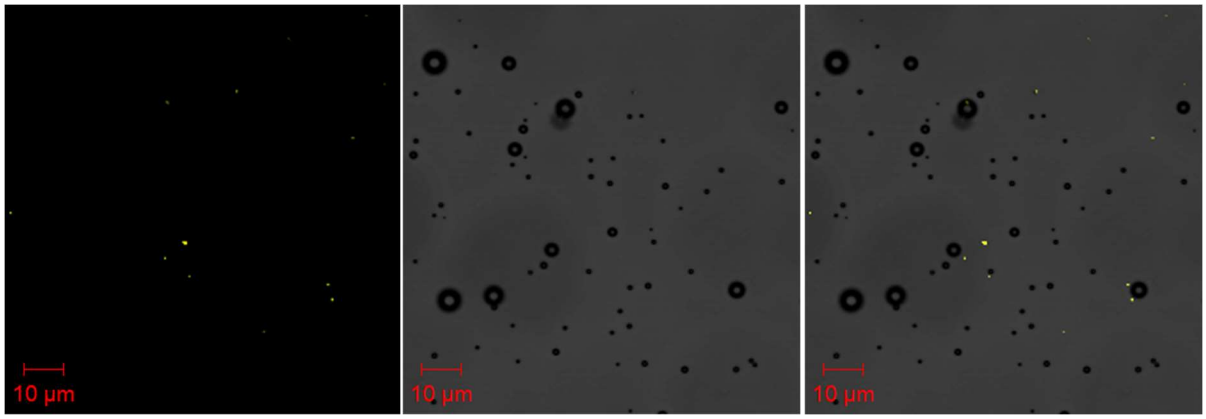

Figure 4.2 Imaging of the 1:40 sample, left to right: fluorescence microscopy, confocal microscopy, overlaid images.

4.3 Platinum^{IV} compound stability

4.3.1 Platinum^{IV} complexes with ultrasound

Delivery using the proposed system, consisting of drug filled liposomes bound to the surface of microbubbles, would require ultrasonic irradiation to cavitate the microbubbles and enhance the drug delivery. The Pt^{IV} prodrugs are intended to be photoactivated, and therefore it is preferable that they don't decompose when exposed to ultrasound. The stability of the compounds was analysed by ^{1}H NMR spectroscopy, monitoring any changes between a control sample and two samples that were sonicated for 3 minutes using a QSonica Probe Sonicator (20 KHz output frequency, 30% amplitude). These conditions correlate to those used in the microbubble cavitation experiments. All samples were made to a concentration of 3 mM in D_2O.

Iproplatin

The ^{1}H NMR spectrum of iproplatin (run in D_2O) has two resonances. A septet at 3.19 ppm and a doublet at 1.27 ppm, respectively correlating to the CH and CH_3 protons on the

isopropylamine ligands. Figure 4.3 shows that there are no changes in the spectra between the control and sonicated samples, indicating that iproplatin is stable when exposed to ultrasound. The resonances for free isopropylamine (in D_2O) appear at 2.96 and 0.97, and so would be visible in the spectra of the sonicated samples if the ligand were being lost.

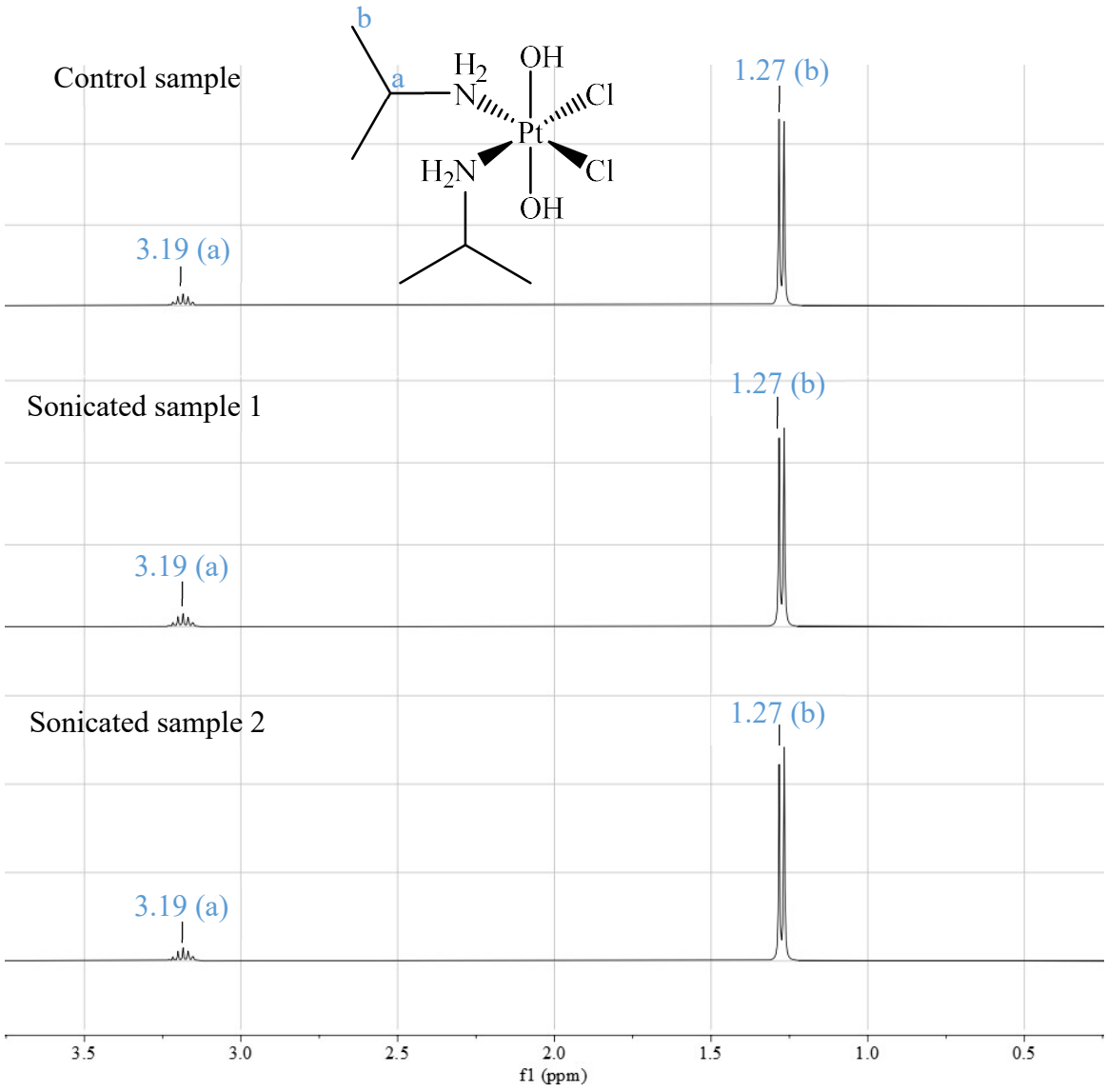

Figure 4.3 Stacked ^{1}H NMR spectra showing the resonances for control and duplicated sonicated samples of iproplatin measured in D_2O.

***trans,trans,trans*-[Pt(*py*)$_2$(N$_3$)$_2$(OH)$_2$]**

The ^{1}H NMR spectrum of *t,t,t*-[Pt(*py*)$_2$(N$_3$)$_2$(OH)$_2$] (run in D_2O) has three resonances, a doublet at 8.73 ppm, a triplet at 8.21 ppm and a triplet at 7.75 ppm. These correlate to the ortho, para and meta protons on the pyridine ligands respectively. The Pt satellites on the ortho proton resonance indicate that the pyridines are bound, and the sharp nature of the satellites shows the Pt centre to be in the +4 oxidation state, as in the +2 oxidation state the satellites are broader. This is due to the chemical shift anisotropy effect. Figure 4.4 shows that there are minimal changes in the spectra between the control and sonicated samples, indicating that the coumpound is mostly stable when exposed to ultrasound. The appearance of very weak resonances adjacent (upfield) to the compound para and meta proton peaks can be seen in the sonicated samples. The resonances for free pyridine (in D_2O) appear upfield at 7.96 ppm, 7.23 ppm, and 6.82 ppm, and as such these weak resonances cannot be from the release of the pyridine. These peaks could be occurring due to formation of a Pt^{II} product, formed through loss of the hydroxyl or azide ligands. Further analysis would need to be carried out to assign these resonances.

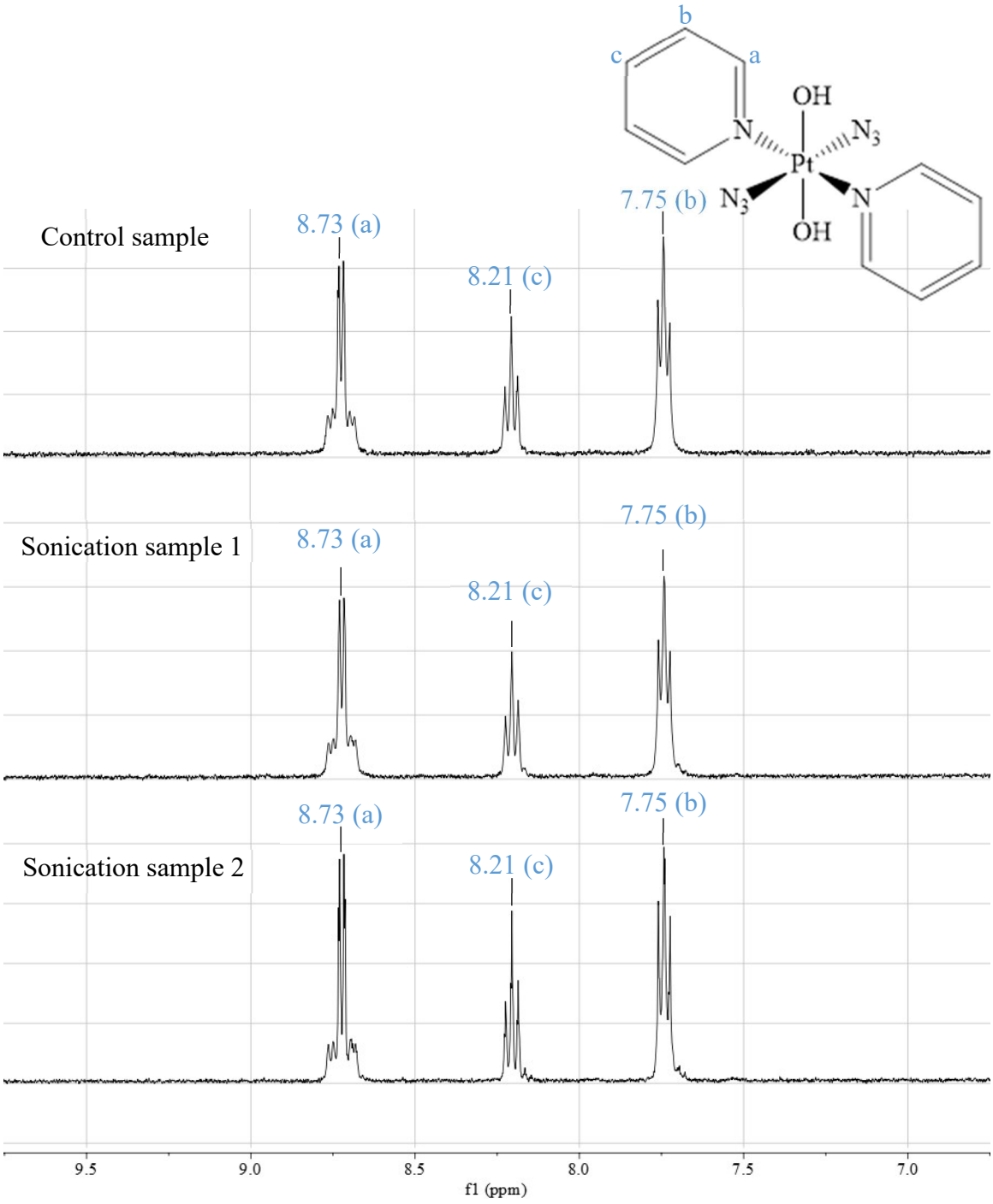

Figure 4.4 Stacked ^{1}H NMR spectra showing the spectra for control and duplicated sonicated samples of t,t,t-$[Pt(py)_2(N_3)_2(OH)_2]$ measure in D_2O.

***cis,cis,trans*-[Pt(*tz*)$_2$(N$_3$)$_2$(OH)$_2$]**

The ^{1}H NMR spectrum of *c,c,t*-[Pt(*tz*)$_2$(N$_3$)$_2$(OH)$_2$] (run in D_2O) has three resonances; a doublet of doublets at 9.27 ppm, a doublet of doublets at 7.93 ppm, and a doublet of doublets at 7.86 ppm. These correlate to the SCN, NCC, and CCS protons on the thiazole ligands respectively. The Pt satellites can be seen on the nitrogen adjacent protons, indicating that the thiazole is bound to a Pt centre. Figure 4.5 shows that there are no changes in the spectra between the control and sonicated samples, indicating that the complex is stable when exposed to ultrasound. The ^{1}H NMR spectrum of free thiazole (in D_2O) also has three resonances; a doublet of doublets at 8.63 ppm, a doublet of doublets at 7.57 ppm, and a doublet of doublets at 7.23 ppm. These correlate to the SCN, NCC, and CCS protons respectively. It would therefore be possible to see the appearance of these resonances if any thiazole were to become disassociated during sonication.

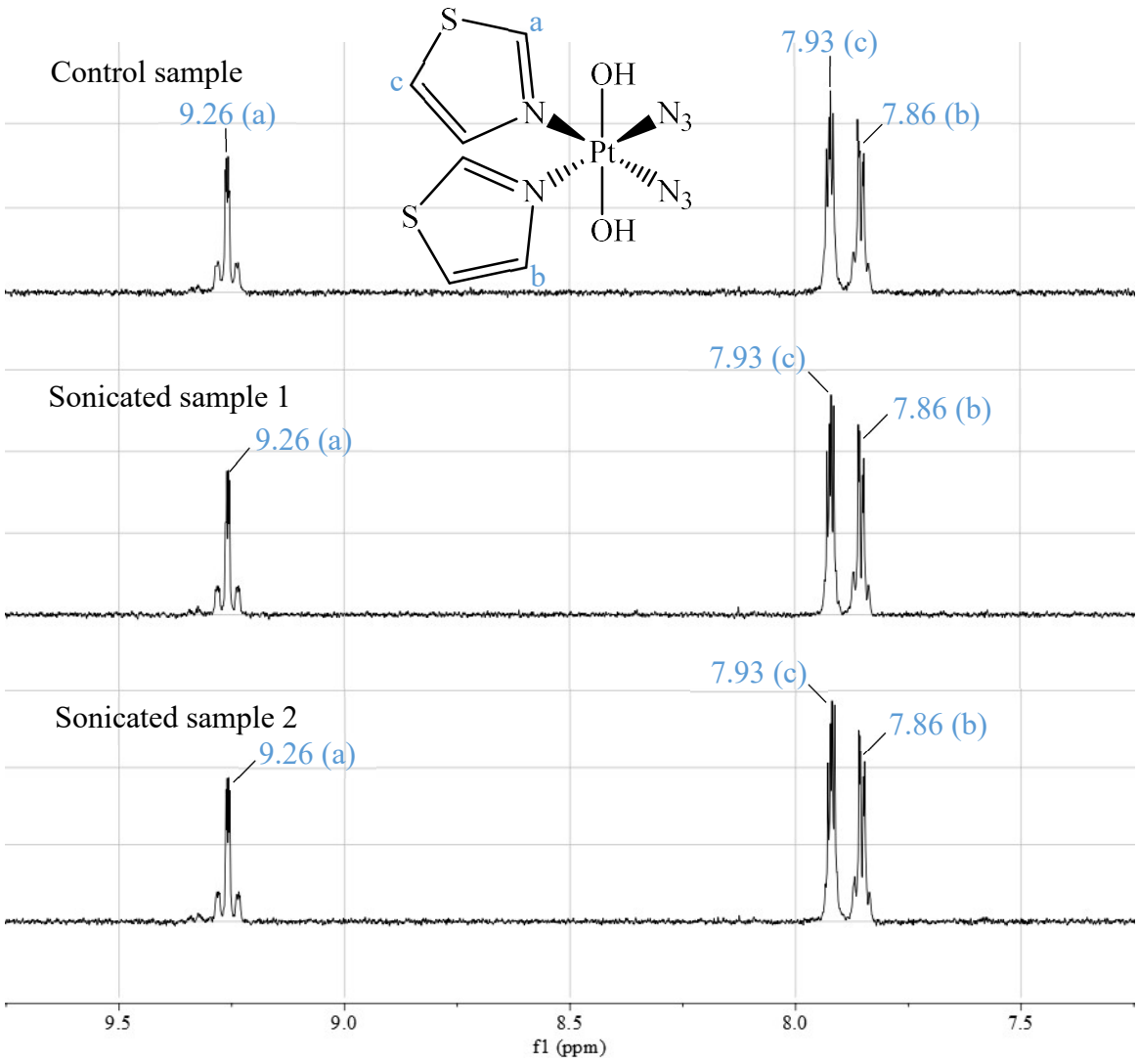

Figure 4.5 Stacked ^{1}H NMR spectra showing the spectra for control and duplicated sonicated samples of c,c,t-$[Pt(tz)_2(N_3)_2(OH)_2]$ measured in D_2O.

***trans,trans,trans*-[Pt(*pz*)$_2$(N$_3$)$_2$(OH)$_2$]**

The ^{1}H NMR spectrum of *t,t,t*-[Pt(*pz*)$_2$(N$_3$)$_2$(OH)$_2$] (run in D_2O) has two resonances, a doublet at 8.99 ppm and a doublet at 8.90 ppm. These correlate to the ortho and meta protons on the pyrazine ligands. Figure 4.6 shows that there are no changes in the spectra between the control and sonicated samples, indicating that the coumpound is stable when exposed to ultrasound. Due to lower aqueous solubility of this complex, the resonances in these spectra are weaker and there is lower resolution of the fine structure of the peaks. This could explain why the expected Pt satellites are not visible. The ^{1}H NMR spectrum of free pyrazine (in D_2O) has a single resonance at 8.48 ppm, which is not seen to appear in the spectra for the sonicated samples. This indicates there has been no loss of the pyrazine ligands.

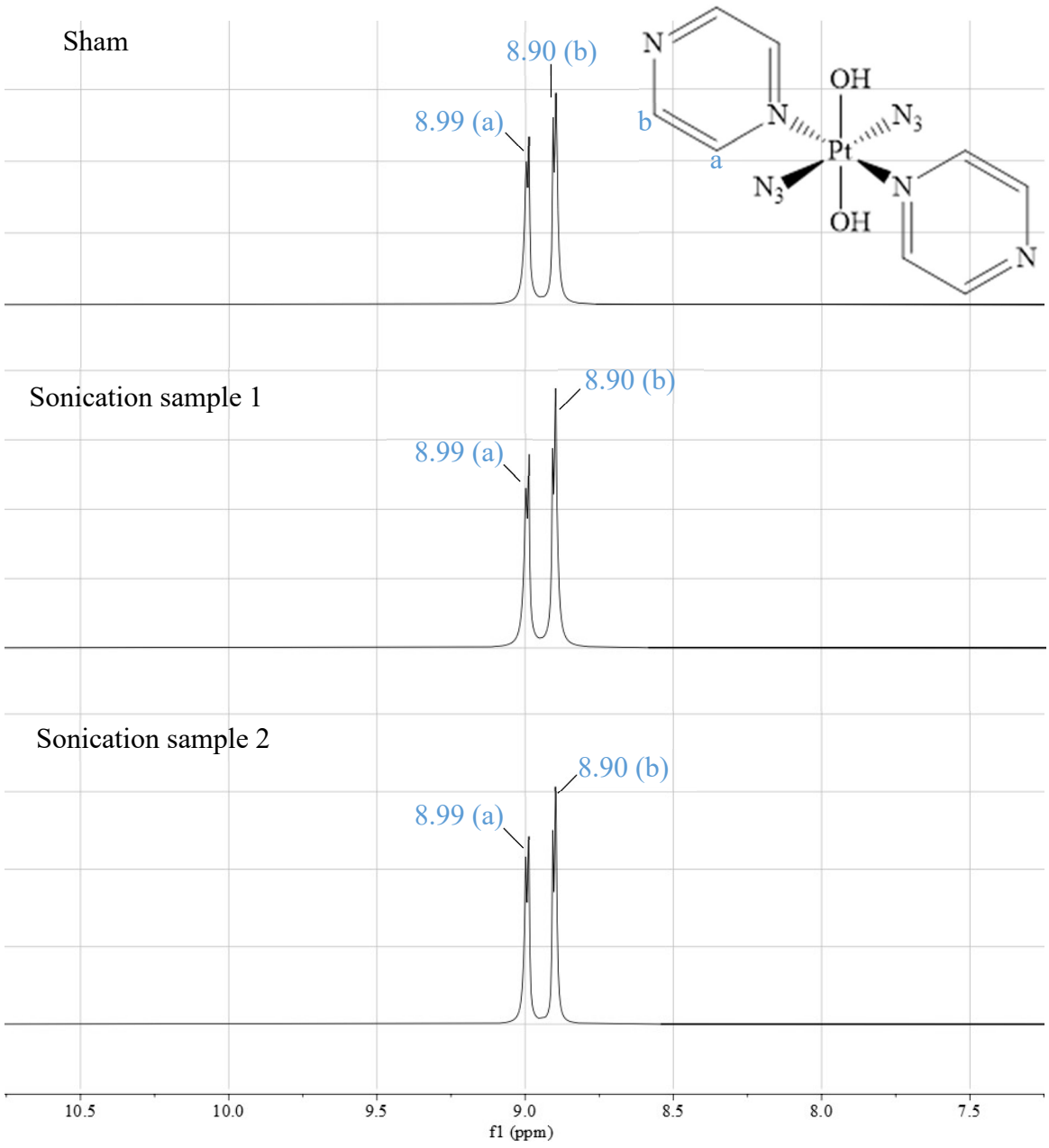

Figure 4.6 Stacked ^{1}H NMR spectra showing the spectra for control and duplicated sonicated samples of t,t,t-$[Pt(pz)_2(N_3)_2(OH)_2]$ measured in D_2O.

4.3.2 Platinum^{IV} reduction by microbubble cavitation

As outlined in Chapter 1, microbubbles have been shown to exhibit sonoluminescence, which is when a collapsing bubble emits light.[8] To assess if this could be used to reduce photoactivatable Pt^{IV} prodrugs to their active Pt^{II} counterparts, *t,t,t*-[Pt(*py*)$_2$(N$_3$)$_2$(OH)$_2$] was added to a solution of microbubbles formed from DSPC and DSPE-mPEG(2000), and the mixture exposed to ultrasound (US). The drug is strongly absorbing in the UV at 294 nm, with reduction in intensity seen as photoreduction occurs, and so UV-Vis spectroscopy was used to monitor the experiments. The microbubbles were formed using a 9:1 ratio of DSPC and DSPE-mPEG(2000). The lipids were predissolved in chloroform (typically 20 mg total lipids) in a glass vial. The chloroform was allowed to evaporate overnight to form a lipid film. The film was resuspended in PBS at approximately 100ºC for 30-60 minutes, and then the lipids fully dispersed with sonication for 1.5-2.5 minutes. The headspace was filled with perfluorobutane and, under continuous gas flow, the contents of the vial sonicated at the liquid-air interface at high intensity for approximately 30 s. The microbubbles were then cooled on ice for 10 minutes. The stock microbubble solution had a concentration of 6.89×10^8 microbubbles mL^{-1}. The concentration per sample was diluted to give 1.07×10^8 microbubbles mL^{-1}. The drug solution concentration was also kept constant at 100 μM. The ultrasound parameters were set to - centre frequency: 1 MHz, acoustic pressure: 185 kPa (peak to peak), pulse repetition frequency: 100 Hz, duty cycle: 30%, pulse length: 3000 cycles, exposure time: 5 mins.

To show that the drug was not reduced purely by ultrasound exposure, UV-Vis spectra were taken for a solution of the drug pre- and post-sonication (Figure 4.7). This shows the drug to be stable under ultrasound conditions, with minimal change between the two spectra.

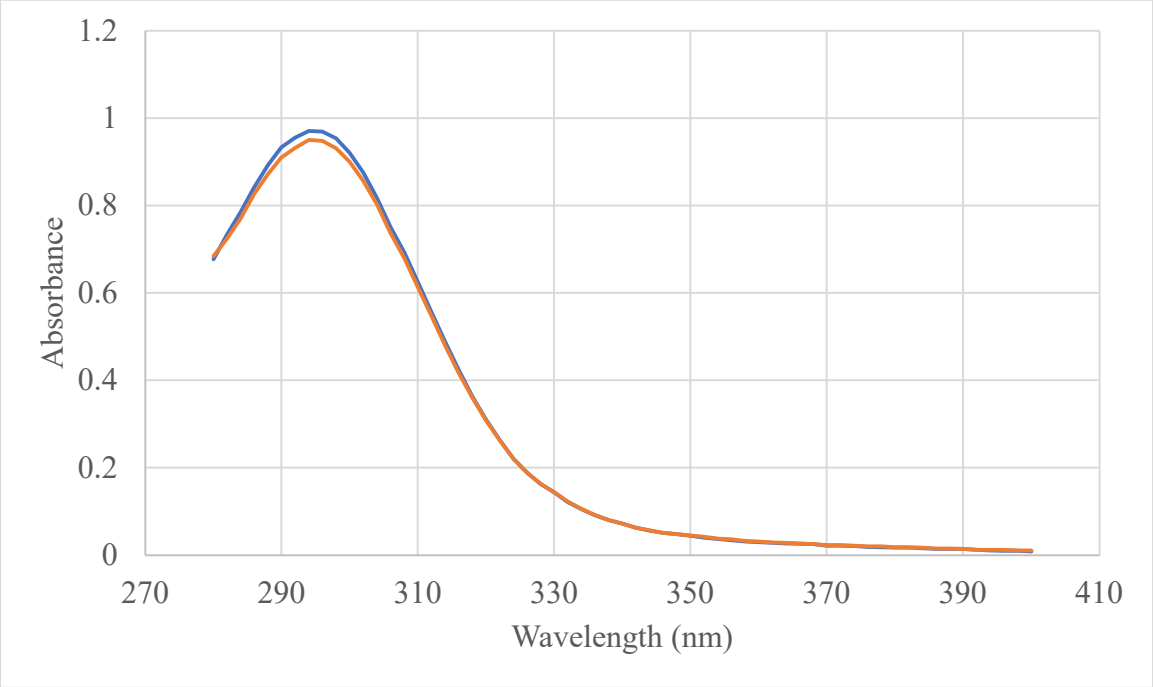

Figure 4.7 UV-Vis spectra comparing the absorbance of t,t,t-[Pt(py)$_2$(N$_3$)$_2$(OH)$_2$] before (blue) and after (orange) 5 minutes exposure to ultrasound.

Combined solutions of microbubbles and drug were then exposed to the same ultrasound conditions, with UV-Vis spectra taken before and after. As a control, these experiments were also run on suspensions of only microbubbles, to assess the absorbance and any change there may be before and after bubble cavitation.

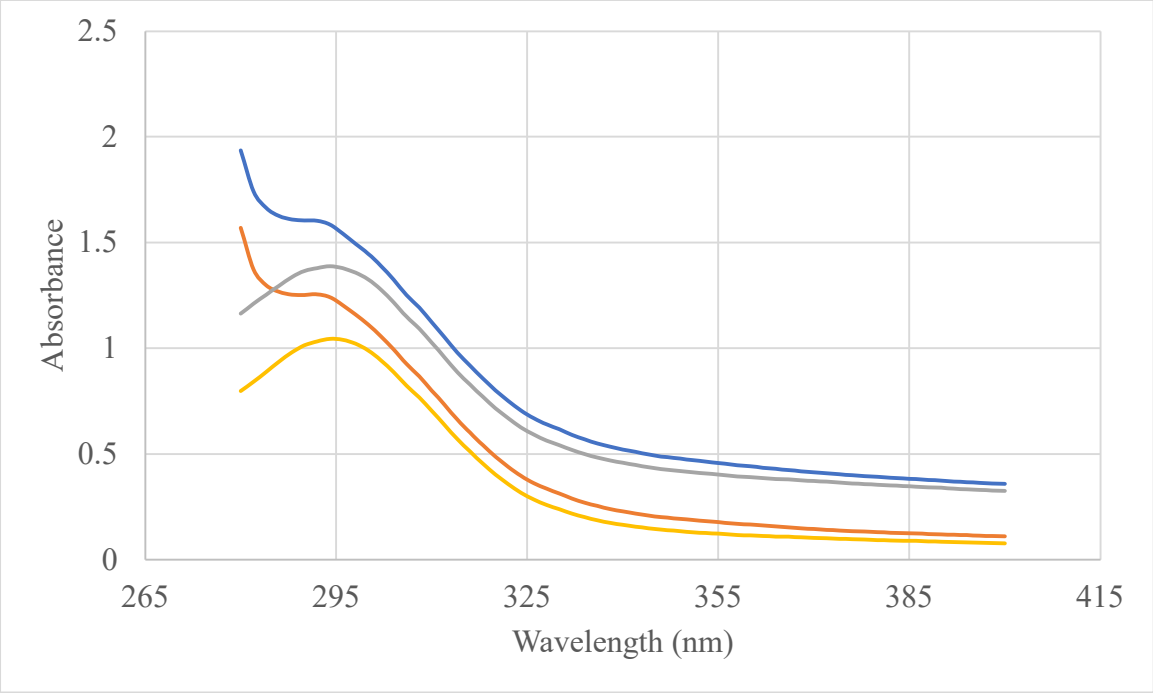

Figure 4.8 UV-Vis spectra comparing pre- and post-ultrasound exposure absorbances; MB only pre (blue), MB only post (orange), MB+Pt pre (grey), MB+Pt post (yellow).

On initial analysis of only the combined solution spectra (grey and yellow lines on Figure 4.8), a reduction in the absorbance was seen, which suggested the experiments had been successful and that the cavitation of the bubbles had caused sonoluminescence and induced photoreduction of the drug. However, when comparing these results with the change in absorbance of only the bubbles, it was seen that the difference in absorbance was the same. This can be seen on Figure 4.8 by the pre- and post-ultrasound spectra being identical, but shifted downwards in intensity. This suggests that as the bubbles are destroyed, their UV-Vis absorbance decreases, and this is therefore the change seen for the bubble and drug samples.

4.4 Conclusions

Based on the fluorescence imaging, it appears that the attempted method of conjugating azide-functionalised liposomes to a DBCO containing lipid before forming microbubbles is

unsuccessful. This may be due to a significantly shorter incubation time than used for the alternative method of conjugation. However, based on this preliminary study, despite the long incubation times the method of conjugating liposomes to already formed microbubbles may be more efficient and reproducible.

All of the complexes discussed in Chapter 2 show stability when exposed to sonication, which would mean that they would remain intact if administered with microbubbles and exposed to ultrasound.

From the sonoluminescence studies, the data suggests that the drug is not being photoreduced by microbubble cavitation. The changes seen in the absorbance between the pre- and post-ultrasound analyses can be assigned to reduced absorbance from the microbubbles being destroyed, rather than from reduction of the concentration of the drug. Because of the absorbance the microbubbles show in the UV-Vis spectra, it may be preferable to analyse the occurrence of the drug reduction by using an alternative technique. ^{195}Pt NMR could be useful for this, as the regions in which the resonances appear are strongly linked to the oxidation state of the Pt centre.

4.5 References

1 S. Tinkov, G. Winter, C. Coester and R. Bekeredjian, *J. Control. Release*, 2010, **143**, 143–150.

2 B. H. A. Lammertink, C. Bos, R. Deckers, G. Storm, C. T. W. Moonen and J. M. Escoffre, *Front. Pharmacol.*, 2015, **6**, 1–17.

3 A. Schroeder, J. Kost and Y. Barenholz, *Chem. Phys. Lipids*, 2009, **162**, 1–16.

4 A. L. Klibanov, T. I. Shevchenko, B. I. Raju, R. Seip and C. T. Chin, *J. Control Release*, 2010, **148**, 13–17.

5 B. Geers, I. Lentacker, N. N. Sanders, J. Demeester, S. Meairs and S. C. De Smedt, *J. Control. Release*, 2011, **152**, 249–256.

6 N. Thomas, University of Oxford, 2018.

7 B. Geers, I. Lentacker, N. N. Sanders, J. Demeester, S. Meairs and S. C. De Smedt, *J. Control. Release*, 2011, **152**, 249–256.

8 K. S. Suslick, S. J. Doktycz and E. B. Flint, *Ultrasonics*, 1990, **28**, 280–290.

Chapter 5 Conclusions and Future Work

5.1 Photoactivatable platinum complexes

This thesis explored the synthesis of two novel Pt^{IV} diazido complexes, *cis,cis,trans*-[$Pt(tz)_2(N_3)_2(OH)_2$] and *trans,trans,trans*-[$Pt(pz)_2(N_3)_2(OH)_2$]. Both complexes were synthesised in good yields and showed aqueous solubility. The photoreducibility of these compounds by irradiation at 405 nm was assessed by UV-Vis spectroscopy, and compared to the known compounds iproplatin (*cis,cis,trans*-[$Pt(NH_2{}^iPr)_2Cl_2(OH)_2$]) and *trans,trans,trans*-[$Pt(py)_2(N_3)_2(OH)_2$]. Both novel compounds showed similar photosensitivity to the *trans*-pyridine complex, with the *cis*-thiazole compound showing the greatest change in absorption at λ_{max}. This suggests it may be the most photoreducible of the compounds. The photochemical characteristics of these compounds may mean they could be used in photoactivated chemotherapy. Iproplatin is only weakly absorbing in the UV, but a slight reduction in the absorption intensity was seen in the UV-Vis spectrum as the irradiation time increased. The irradiation of all four complexes caused precipitation from solution, and the formation of bubbles was seen for the diazido compounds. The release of bubbles could indicate the formation of nitrogen gas through loss of the azide ligands. Future work would involve obtaining analytical quantities of the precipitates in order to characterise them, and to quantify how much of the Pt^{IV} is actually being reduced during irradiation. This in turn would allow for better understanding of the mechanisms by which the photoreduction is occurring.

The next steps for analysis of the novel compounds would be to carry out cell studies, to assess their chemotherapeutic properties, and obtain IC_{50} values. IC_{50}, defined as the concentration of a drug needed to inhibit a biological process or response by 50%, would give quantitative

values of how much of the compounds is needed to kill half of a known number of cells.[1] These studies would need to be carried out in the absense of light, to see if the compounds are non-toxic in the dark, and under clinically relevant irradiation conditions. In order to compare the cytotoxicities of the novel complexes to the known compound *trans,trans,trans*-[Pt(*py*)$_2$(N$_3$)$_2$(OH)$_2$], the cell lines utilised by Farrer *et al.* should be used; HaCaT, A2780, A2780CIS (cisplatin resistant), OE19, and HepG2.[2] These cancerous cell lines correspond to the skin, ovaries, gastric system and liver respectively. Although these are not relevant to the treatment of DIPG, having an understanding of the properties the novel compounds exhibit in comparison to a known complex may be of interest. To directly test the potential of *cis,cis,trans*-[Pt(*tz*)$_2$(N$_3$)$_2$(OH)$_2$] and *trans,trans,trans*-[Pt(*pz*)$_2$(N$_3$)$_2$(OH)$_2$] in the treatment of DIPG cell studies using the SF8628 cell line, derived by surgical biopsy from a pediatric H3.3K27M DIPG patient, could be carried out.[3]

Finally, further attempts would be made to synthesise *cis,cis,trans*-Pt[(*pz*)$_2$(N$_3$)$_2$(OH)$_2$]. This would involve varying the solvent system, as poor aqueous solubility of the Pt^{II} precursor *cis,cis*-[Pt(*pz*)$_2$I$_2$] may be one of the limiting factors of the synthesis. Variations in temperature and reaction time would also be explored to try and improve yields.

5.2 Liposomes

Liposomes composed of a phosphatidylcholine lipid (PC), cholesterol, and 1,2-distearoyl-sn-glycero-3-phosphoethanolamine-N-[methoxy(polyethyleneglycol)-2000] (DSPE-mPEG(2000)) in the molar ratio 54:36:10 were utilised for loading experiments, to assess the uniformity of liposome suspensions, and to identify whether differential scanning calorimetry (DSC) could be used in the characterisation of liposomes.

Comparisons between 1,2-dipalmitoyl-sn-glycero-3-phosphocholine (DPPC), and 1,2-dibehenoyl-sn-glycero-3-phosphocholine (DBPC) containing liposomes by dynamic light scattering (DLS) found that DPPC formulations yielded suspensions with a lower polydispersity index (PdI), and fractionally smaller liposomes, when formed by extrustion. DBPC containing liposomes formed by extrusion and sonication were both less monodisperse than the DPPC formulations. Due to the increased uniformity, and lower extrusion temperature required, the DPPC containing compositions was chosen for all loading experiments.

It was hypothesised that liposomes could be characterised by DSC, with the thermal profile of a liposomal formulation corresponding to an average of its composite lipids.[4] Experimental analysis found that no thermal transitions could be seen for liposomal suspensions, and altering the liposomal matrices did not change the outcome. As DLS had previously been used to characterise liposomes with high success, all subsequent liposomes were analaysed by this method.

Iproplatin was loaded into standard formulation liposomes using either the calcium acetate, or ammonium sulphate active loading methods.[5–8] Experiments were repeated in quintuplicate and found that the initial loading, and subsequent retention, was higher when using the ammonium sulphate method. The average initial encapsulations were 1.02 mg mL^{-1} for the calcium acetate method, and 1.61 mg mL^{-1} for the ammonium sulphate method. After 10 days, 21.5% of the encapsulated drug remained in the calcium acetate liposomes, whilst 34.9% remained in the ammonium sulphate liposomes. The improved loading and retention by the ammonium sulphate method suggests that iproplatin may behave as a weak base, however determination of the pK_a of the complex yielded a value of 3.54 in H_2O. This is a relatively acidic pK_a. This indicates that the best loading method for a given compound may not relate

solely to its acidic or basic behaviour, but may be a combination of several factors, and therefore pK_a values cannot be used as the sole deciding factor in choosing a loading method for a complex. Loading of the complex *trans,trans,trans*-[Pt(*py*)$_2$(N$_3$)$_2$(OH)$_2$] into the same standard liposomes was briefly explored by the calcium acetate method, which showed poorer loading and retention compared to iproplatin, however replicates of these experiments would need to be done to reinforce this result. Future work would involve loading the *trans*-pyridine complex, and both novel compounds from Chapter 2 into the standard liposomes using both the calcium acetate and ammonium sulphate methods. Replicates of these experiments would provide a better understanding of how these complexes behave, and could be compared to the experimentally derived pK_a values obtained in this thesis.

Although iproplatin can be loaded into the standard formulation liposomes, the retention of the drug by both methods is still relatively poor, and therefore cross-linked liposomes were explored to try and improve this quality. The standard composition was altered by removing half of the DPPC, and substituting it for 1,2-bis(10,12-tricosadiynoyl)-sn-glycero-3-phosphocholine (23:2 Diyne PC) which polymerises when irradiated with UV-light (254 nm). Raman spectroscopy was used to monitor the polymerisation, and an optimum irradiation time of 40 minutes was selected as beyond this point pores start to form in the bilayer. The drug was loaded into the liposomes, by either the calcium acetate or ammonium sulphate method, before irradiation. Initial encapsulation efficiencies showed the ammonium sulphate method to be significantly more efficient, with an encapsulation concentration of 2.18 mg mL^{-1} compared to 0.44 mg mL^{-1} using the calcium acetate method. However, samples measured immediately after irradiation showed a drastic decrease in the concentration of Pt, suggesting the drug is either decomposing or leaking out during the polymerisation stage. This data, along with the

UV-Vis irradiation data for iproplatin, suggests that it is photoreducible and is therefore not compatible with liposomes cross-linked by this method. The diazido complexes discussed in Chapter 2 are more strongly photoactivatable, and would therefore also not be viable for this liposomal formulation.

Another method of improving liposomal encapsulation is to use a chitosan coating on the external surface of the liposomes. Chitosan is a positively charged linear polysaccharide, and so forms electrostatic interactions with the negatively charged liposomal surface, leading to surface adsorption.[9] Research has shown that it can be used to successully coat DPPC liposomes, increasing their stability without significantly altering the main phase transition temperature.[10] One study has shown that chitosan coated butyric acid loaded liposomes could be used as chemotherapeutics to treat human hepatoma cells.[11] The use of chitosan to stabilise liposomes for oral administration has also been investigated.[12,13] Future work would explore using chitosan coatings with the standard liposome formulation used in this thesis to assess if it improves the retention of any loaded drugs. Initial studies would be carried out using iproplatin, as there is the most data for these systems for comparison. However, if the other complexes had showed successful encapsulation by active loading methods, then chitosan coating could also be applied to those systems.

5.3 Microbubbles and ultrasound

An alternative method of liposome-microbbuble conjugation was attempted. This involved clicking azide functionalised liposomes to a DBCO functionalised lipid, before adding this to a solution of the other microbubble lipids, and forming the bubbles *in situ*. The inclusion of 3,3'-dioctadecyloxacarbocyanine perchlorate (DiO) in the liposome formulation allowed for

the conjugated systems to be analysed by fluorescence microscopy. It appeared that at a concentrated reaction ratio of liposomes to microbubbles (1:4, v/v) conjugation had been successful. This was determined by the appearance of circular rings in the fluorescence imaging, which correspond to liposomes bound to the surface of the microbubbles. A dilute reaction ratio sample (1:40, v/v) did not show this fluorescence, suggesting that the liposomes may not have been conjugated and had been removed from the suspension during the washing phase. Replicates of these experiments would need to be done in order to confirm whether the adherance seen for the concentrated sample was reproducible. When altering the method of conjugation for this work the time frame for the reaction was dropped significantly, from 18 hours using the original method to 2 hours using the new method. This limits the comparisons that can be drawn between the methods, as the change is too significant. A reaction time of 18 hours should have been used for the new method, with concentrations of liposomes and microbubbles kept constant, and then the products of both methods compared by quantitative fluorescence. This would have allowed for a direct comparison of the amount of liposomes conjugated to the microbubbles, and would have given an answer for which method yielded the best system. The reaction time for the new method could then be decreased to see if the maximum conjugation could be achieved in a shorter time frame. These studies would be undertaken as part of the future work for this project.

Reduction of the photoactivatable Pt^{IV} drug *trans,trans,trans*-$[Pt(py)_2(N_3)_2(OH)_2]$ was attempted by sonoluminescence. The results showed that there was a reduction in intensity in the UV-Vis spectra of the solution of microbubbles and drug after exposure to ultrasound. However, this reduction was later attributed to absorption of the bubbles, which decreased after cavitation. In order to assess if sonoluminescence can occurr with these systems, a different

method of analysis may be needed in which the microbubbles do not mask the presence of any Pt species. One possible alternative would be using ^{195}Pt NMR spectroscopy. This would allow for analysis before sonication to ensure that only Pt^{IV} species were present, and analysis afterwards to identify if any Pt^{II} species had been produced. Finally, to ensure that the complexes discussed in Chapter 2 would be compatible with a microbubble-liposome system that needed ultrasound exposure, the stability of all complexes when sonicated was assessed. ^{1}H NMR spectra showed no changes between sham and sonicated samples for iproplatin, *cis,cis,trans*-[Pt(*tz*)$_2$(N$_3$)$_2$(OH)$_2$], and *trans,trans,trans*-[Pt(*pz*)$_2$(N$_3$)$_2$(OH)$_2$], indicating that these three compounds are stable under ultrasound exposure. The ^{1}H NMR spectrum for *trans,trans,trans*-[Pt(*py*)$_2$(N$_3$)$_2$(OH)$_2$] showed no significant changes, however weak resonances could be seen appearing adjacent to the para and meta compound resonance peaks. These could indicate the formation of a Pt^{II} species, and further analysis would need to be done to identify this species.

The long term goals from this work would be to optimise the synthesis of a microbubble-liposome system which could carry a photoactivatable Pt^{IV} prodrug. This system could then be used in ultrasound targeted therapy, utilising the targeted delivery and enhanced uptake afforded by sonoporation at impermeable biological membranes, and exploiting the phenomenom of sonoluminescence to reduce the drug to its active counterpart.

5.4 References

1 D. C. Swinney, in *Annual Reports in Medicinal Chemistry*, ed. J. E. Macor, Academic Press, 46th edn., 2011, pp. 301–317.

2 N. J. Farrer, J. A. Woods, L. Salassa, Y. Zhao, K. S. Robinson, G. Clarkson, F. S. MacKay and P. J. Sadler, *Angew. Chemie - Int. Ed.*, 2010, **49**, 8905–8908.

3 S. Mueller, R. Hashizume, X. Yang, I. Kolkowitz, A. K. Olow, J. Phillips, I. Smirnov, M. W. Tom, M. D. Prados, C. D. James, M. S. Berger, N. Gupta and D. A. Haas-Kogan, *Neuro. Oncol.*, 2014, **16**, 352–360.

4 M. Bastos, *Malvern Instruments Ltd.*, 2016.

5 G. Haran, R. Cohen, L. K. Bar and Y. Barenholz, *BBA - Biomembr.*, 1993, **1151**, 201–215.

6 E. M. Bolotin, R. Cohen, L. K. Bar, N. Emanuel, S. Ninio, Y. Barenholz and D. D. Lasic, *J. Liposome Res.*, 1994, **4**, 455–479.

7 S. Clerc and Y. Barenholz, *BBA - Biomembr.*, 1995, **1240**, 257–265.

8 D. D. Lasic, B. Čeh, M. C. A. Stuart, L. Guo, P. M. Frederik and Y. Barenholz, *BBA - Biomembr.*, 1995, **1239**, 145–156.

9 M. O. Alshraim, S. Sangi, G. I. Harisa, A. H. Alomrani, O. Yusuf and M. M. Badran, *Molecules*, 2019, **24**, 1–14.

10 M. M. Mady and M. M. Darwish, *J. Adv. Res.*, 2010, **1**, 187–191.

11 V. Quagliariello, M. Masarone, E. Armenia, A. Giudice, M. Barbarisi, M. Caraglia, A. Barbarisi and M. Persico, *Oncol. Rep.*, 2019, **41**, 1476–1486.

12 C. M. Lee, D. W. Kim and K. Y. Lee, *J. Exp. Biomed. Sci.*, 2011, **17**, 211–216.

13 C. Hui and H. Huang, *J. Dispers. Sci. Technol.*, 2021, **42**, 1494–1503.

Chapter 6 Experimental Methods

6.1 General Procedures

Commercially available solvents and chemicals were purchased and used without further purification (unless otherwise stated). Deionised water was obtained using an Elix® Essential water purification system.

NMR Spectroscopy: NMR spectra were acquired at 298 K. 400.2 MHz ^{1}H NMR, 100.6 MHz ^{13}C NMR, and 86 MHz ^{195}Pt NMR spectra were recorded on a Bruker Avance III HD nanobay NMR equipped with an 9.4 T magnet. All spectra are referenced to the residual solvent peak, unless otherwise stated. The chemical shifts (δ) are reported in parts per million (ppm).

Mass Spectrometry: Mass spectra were acquired using either an Agilent Technology 1260 Infinity or a Waters LCT premier XE spectrometer. High resolution accurate mass spectra were recorded to 4 decimal places using Bruker μTOF and Micromass GCT systems.

IR-Spectroscopy: Infrared spectra were recorded in solid-state using a Bruker Tensor 27 FT-IR spectrometer with an IR Diamond Attenuated Total Reflectance module. Data was processed using Bruker OPUS software.

UV-Vis Spectroscopy: UV-Visible absorption spectra were recorded using a Jasco V770 spectrophotometer with Spectra Manager™ Suite software.

Dynamic Light Scattering: Liposomes and microbubbles were sized by dynamic light scattering using a Malvern Zetasizer Nano ZS.

Differential Scanning Calorimetry: DSC experiments were carried out using the Williams' group instrument at the University of Oxford.

pH Measurements: pH measurements for the pK_a analysis in Chapter 3 were recorded at ambient temperature using Hanna Instruments Pocket Checker pH Tester. The meter was calibrated using standard buffer solutions (pH 7.00, pH 4.01, pH 10.01), as supplied by the provider.

ICP-MS

Platinum and phosphorus content in samples were determined by ICP-MS, using either a Perkin Elmer Elan 6100 DRC ICP-MS or a Perkin Elmer NexION 2000B ICP-MS. Analysis was carried out by Dr. Philip Holdship in the Department of Earth Sciences and Dr. Trang To in the Department of Geography, University of Oxford. Volumetric flasks were prepared by washing with 20% Romil ultrapure analytical grade (UPA) nitric acid overnight. 50 µL of each sample was placed into a 10 mL volumetric flask with 450 µL concentrated HNO_3, 50 µL concentrated HCl, and 100 µL H_2O_2 (30% v/v) added. Samples were heated at 110 °C for approximately 2 hours until foaming had stopped, to ensure complete digestion. Samples were diluted up to 10 mL with deionised water, and 2 mL of this further diluted up to 10 mL with deionised water. Concentrations were detected for ^{194}Pt, ^{195}Pt and ^{31}P isotopes and scaled up according to isotopic abundance.

Microscopy

Brightfield microscope images were captured using a Leica microscope (Leica Microsystems GmbH, Wetzlar, Germany), with a QImaging digital camera (MicroPublisher 3.3 RTV, QImaging, Surrey, Canada). The processing software was LivingImage v8 (Media Cybernetics, Inc., Rockville, MD, USA). For fluorescence imaging, a Zeiss Laser Scanning

Microscope 710 (LSM 710) (Carl Zeiss Microscopy GmbH, Jena, Germany) was used. The processing software was ZEN (Zeiss).

Ultrasound conditions

Experiments were carried out in the Biomedical Ultrasonics & Biotherapy Laboratory (BUBBL) at the Oxford Institute of Biomedical Engineering. Samples were placed into the SAT2 ultrasound treatment device and treated with ultrasound for 3 minutes. Ultrasound parameters were set to - centre frequency: 1 MHz, acoustic pressure: 148 kPa (peak to peak), pulse repetition frequency: 100 Hz, duty cycle: 30%, pulse length: 3000 cycles, exposure time: 180 s. Samples without ultrasound applied were loaded into the setup for 3 minutes (sham irradiation).

6.2 Synthetic Methods

***cis,cis*-[Pt($NH_2{}^iPr$)$_2$$I_2$]**

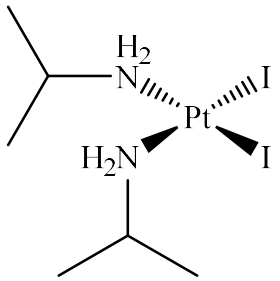

K_2PtCl_4 (1.00 g, 2.41 mmol) was added to deionised water (50 mL) and stirred to dissolve. KI (3.88 g, 23.37 mmol) was added, and the reaction stirred in the dark at RT for 1 hour. $NH_2{}^iPr$ (0.4 mL, 4.70 mmol) was added drop wise over 10 minutes, and the reaction stirred in the dark at RT for a further 4 hours. The resulting dark orange precipitate was collected by filtration

under suction, and washed with the minimum amount of cold water, methanol and diethyl ether.

Yield: 1.180 g, 83.2%. ^{1}H NMR (DMF-d_7, 400 MHz) δ (ppm) 4.81 (4H, broad singlet, NH_2), 3.53 (2H, septet, CH), 1.28 (12H, doublet, CH_3) ppm. ^{13}C NMR (DMF-d_7, 101 MHz) δ (ppm) 49.1, 23.2 ppm. ^{195}Pt NMR (DMF-d_7, 86 MHz) δ (ppm) -2238 ppm. ES$^+$MS (*m/z*) 1136 ($[2M + H]^+$), 1158 ($[2M + Na]^+$).

***cis,cis*-[Pt($NH_2{}^iPr$)$_2$$Cl_2$]**

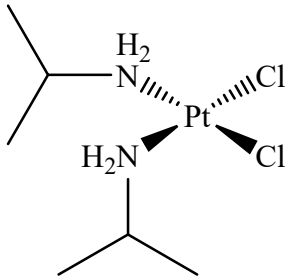

Cis-[Pt($NH_2{}^iPr$)$_2$$I_2$] (0.88 g, 1.56 mmol) was added to deionised water (60 mL). $AgNO_3$ (0.49 g, 1.85 eq.) was added and the reaction stirred in the dark at RT overnight. The resulting suspension was filtered (celite and IM) to remove the AgI. The clear yellow filtrate was transferred to a clean flask and NaCl (0.36 g, 3.95 eq.) was added. The reaction was left stirring in the dark at 40 °C overnight, followed by cooling to 4 °C. The resulting pale yellow precipitate was collected by filtration under suction and washed with the minimum amount of cold water, methanol and diethyl ether.

Yield: 0.441 g, 73.5%. ^{1}H NMR (DMF-d_7, 400 MHz) δ (ppm) 4.80 (4H, broad singlet, NH_2), 3.24 (2H, septet, CH), 1.27 (12H, doublet, CH_3) ppm. ^{13}C NMR (DMF-d_7, 101 MHz) δ (ppm) 48.0, 22.9 ppm. ^{195}Pt NMR (DMF-d_7, 86 MHz) δ (ppm) -2210 ppm. ES$^+$MS (*m/z*) 733 ($[2M – Cl]^+$), 1117 ($[3M – Cl]^+$).

***cis,cis,trans*-[Pt(NH$_2$^{i}Pr)$_2$Cl$_2$(OH)$_2$]**

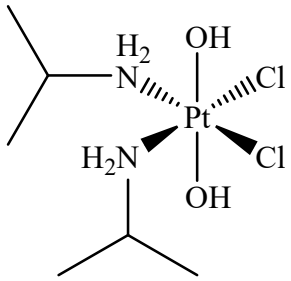

Cis-[Pt(NH$_2$^{i}Pr)$_2$Cl$_2$] (0.14 g, 0.37 mmol) was added to deionised water (5 mL). H_2O_2 (0.5 mL, 30% v/v) was added drop wise, and the reaction left to stir in the dark at 50 °C overnight. The solvent was removed by rotary evaporation to give a pale yellow solid. The resulting solid was dissolved in water:acetonitrile (95:5) and purified by HPLC.

Yield: 0.090 g, 58.2%. ^{1}H NMR (D_2O, 400 MHz) δ (ppm) 3.19 (2H, septet, CH), 1.27 (12H, doublet, CH_3) ppm. ^{13}C NMR (D_2O, 101 MHz) δ (ppm) 48.0, 22.1 ppm. ^{195}Pt NMR (D_2O, 86 MHz) δ (ppm) 942 ppm. ES$^+$MS (*m/z*) 418 ([M + H]$^+$), 835 ([2M + H]$^+$), 1252 ([3M + H]$^+$).

***trans,trans*-[Pt(*py*)$_2$Cl$_2$]**

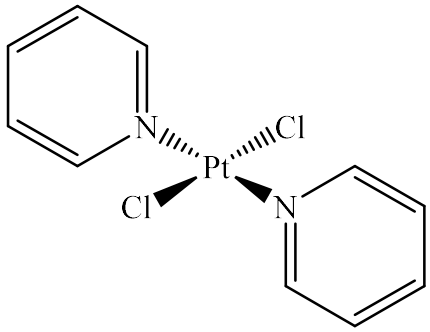

K_2PtCl_4 (1.00 g, 2.41 mmol) was dissolved in deionised water (25 mL) and pyridine (0.9 mL, 11.17 mmol) was added. The reaction was stirred in the dark at 85 °C overnight, cooled to RT and then filtered (IM). The solvent was removed from the filtrate by rotary evaporation to give a white solid. The solid was washed with a small amount of diethyl ether. HCl (25 mL, 2 M) was added to the dried product and the reaction stirred in the dark at 75 °C for 24 hours. The yellow suspension was cooled on ice. The resulting yellow precipitate was collected by filtration under suction, and washed with the minimum amount of cold water, ethanol and diethyl ether.

Yield: 0.837 g, 81.4%. ^{1}H NMR (DMF-d_7, 400 MHz) δ (ppm) 8.85 (4H, doublet, CH), 8.03 (2H, triplet, CH), 7.55 (4H, triplet, CH) ppm. ^{13}C NMR (DMF-d_7, 101 MHz) δ (ppm) 153.6, 139.4, 125.8 ppm. ^{195}Pt NMR (DMF-d_7, 86 MHz) δ (ppm) -1947 ppm. ES$^+$MS (*m/z*) 425 ($[M + H]^+$), 447 ($[M + Na]^+$).

***trans,trans*-[Pt(*py*)$_2$(N$_3$)$_2$]**

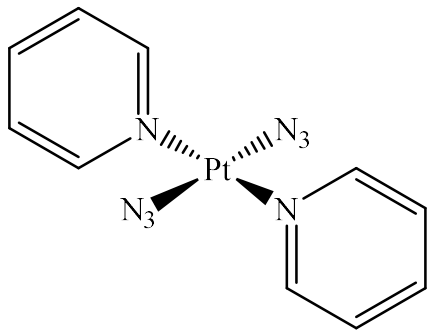

trans-[Pt(*py*)$_2$Cl$_2$] (0.70 g, 1.65 mmol) was suspended in deionised water (120 mL) with $AgNO_3$ (0.55 g, 3.24 mmol). The reaction was stirred in the dark overnight at 60 °C. The resulting suspension was filtered (celite and IM) to remove the AgCl. NaN_3 (0.55 g,

8.46 mmol) was added to the filtrate, and the reaction stirred in the dark at RT for 4 hours. A second quanitity of NaN_3 (0.55 g, 8.46 mmol) was added and stirred for a further 4 hours. The suspension was placed on ice, and the resulting yellow solid collected by filtration under suction. The product washed with the minimum amount of cold water, ethanol and diethyl ether to get crude product. The crude product was recrystallised from pyridine (1 g per 37.5 mL, preheated to 40 °C) and immediately filtered (IM). The solution was cooled on ice to give a yellow precipitate. The pure product was collected by filtration under suction.

Yield: 0.360 g, 50.8%. ^{1}H NMR ($CDCl_3$, 400 MHz) δ (ppm) 8.75 (4H, doublet, CH), 7.82 (2H, triplet, CH), 7.39 (4H, triplet, CH) ppm. ^{13}C NMR ($CDCl_3$, 101 MHz) δ (ppm) 152.6, 138.9, 126.1 ppm. ^{195}Pt NMR ($CDCl_3$, 86 MHz) δ (ppm) -2096 ppm. ES$^+$MS (*m/z*) 438 ($[M + H]^+$), 876 ($[2M + H]^+$), 898 ($[2M + Na]^+$).

***trans,trans,trans*-[Pt(*py*)$_2$(N$_3$)$_2$(OH)$_2$]**

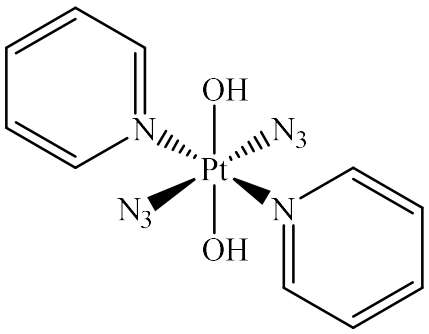

trans-[Pt(*py*)$_2$(N$_3$)$_2$] (0.15 g, 0.34 mmol) was suspended in H_2O_2 (10.5 mL, 30% v/v) and stirred in the dark at 45 °C for 3 hours. The solvent level was reduced to approximately 2.5 mL by rotary evaporation at 50 °C. Ethanol (6 mL) was added and the solution filtered (IM). Diethyl ether (18 mL) was added to the filtrate and the solution cooled in the freezer overnight to give yellow needle crystals. The product was collected by filtration under suction.

Yield: 0.127 g, 79.4%. ^{1}H NMR (D_2O, 400 MHz) δ (ppm) 8.73 (4H, doublet, CH), 8.21 (2H, triplet, CH), 7.75 (4H, triplet, CH) ppm. ^{13}C NMR (D_2O, 101 MHz) δ (ppm) 149.4, 142.6, 127.1 ppm. ^{195}Pt NMR (D_2O, 86 MHz) δ (ppm) 958 ppm. ES^{+}MS (*m/z*) 494 ($[M + Na]^{+}$), 943 ($[2M + H]^{+}$), 965 ($[2M + Na]^{+}$).

***cis,cis*-[Pt(*tz*)$_2$I$_2$]**

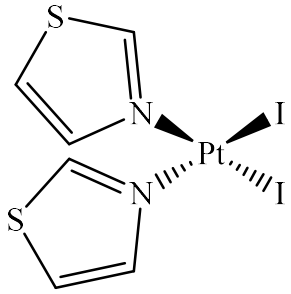

K_2PtCl_4 (0.50 g, 1.21 mmol) was dissolved in distilled water (38 mL). KI (2.00 g, 12.1 mmol) was added and the reaction left to stir in the dark at RT for 1 hour. Thiazole (0.17 mL, 2.41 mol) was added and the reaction stirred in the dark at RT for 24 hours. The suspension was separated by filtration under suction. The resulting solid was washed with the minimum amount of cold water, ethanol and diethyl ether.

Yield: 0.644 g, 86.2%. ^{1}H NMR (DMSO-d_6, 400 MHz) δ (ppm) 9.14 (2H, doublet of doublets, CH), 7.98 (2H, doublet of doublets, CH), 7.80 (2H, doublet of doublets, CH) ppm. ^{13}C NMR (DMSO-d_6, 101 MHz) δ (ppm) 154.4, 143.7, 120.4 ppm. ^{195}Pt NMR (DMSO-d_6, 86 MHz) δ (ppm) -3105 ppm. ES^{+}MS (*m/z*) 1239 ($[2M + H]^{+}$).

***cis,cis*-[Pt(*tz*)$_2$Cl$_2$]**

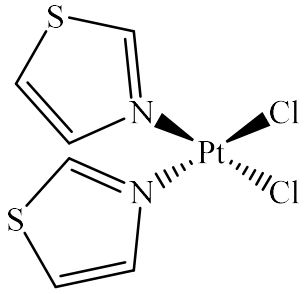

cis-[Pt(*tz*)$_2$I$_2$] (0.64 g, 1.03 mmol) was suspended in distilled water (125 mL). $AgNO_3$ (0.35 g, 2.06 mmol) was added and the reaction stirred in the dark at 60 °C for 24 hours. The suspension was filtered (celite and IM) to remove the AgI. NaCl (0.60 g, 10.30 mmol) was added to the filtrate and the reaction stirred in the dark at RT for 24 hours. The product was isolated by filtration under suction and washed with the minimum amount of cold water, ethanol and diethyl ether.

Yield: 0.209 g, 84.0%. ^{1}H NMR (DMSO-d$_6$, 400 MHz) δ (ppm) 9.47 (2H, doublet of doublets, CH), 7.97 (2H, doublet of doublets, CH), 7.95 (2H, doublet of doublets, CH) ppm. ^{13}C NMR (DMSO-d$_6$, 101 MHz) δ (ppm) 154.4, 143.7, 120.4 ppm. ^{195}Pt NMR (DMSO-d$_6$, 86 MHz) δ (ppm) -1905 ppm. ES$^+$MS (*m/z*) 837 ([2M – Cl]$^+$).

***cis,cis*-[Pt(*tz*)$_2$(N$_3$)$_2$]**

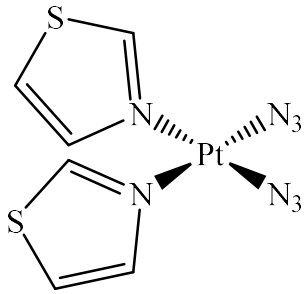

cis-[Pt(*tz*)$_2$Cl$_2$] (0.10 g, 0.23 mmol) was suspended in distilled water (20 mL). $AgNO_3$ (0.08 g, 0.46 mmol) was added and the reaction left to stir overnight in the dark at 60 °C. The

suspension was filtered (celite and IM) to remove the AgCl. NaN_3 (0.15 g, 2.30 mmol) was added to the filtrate and the reaction stirred at in the dark at RT for 24 hours. The resulting suspension was separated by filtration under suction and the solid washed with minimal cold water, ethanol and diethyl ether.

Yield: 0.082 g, 79.3%. ^{1}H NMR (CD_3CN, 400 MHz) δ (ppm) 9.11 (2H, doublet of doublets, CH), 7.84 (2H, doublet of doublets, CH), 7.73 (2H, doublet of doublets, CH) ppm. ^{13}C NMR (CD_3CN, 101 MHz) δ (ppm) 158.0, 144.2, 123.1 ppm. ^{195}Pt NMR (CD_3CN, 86 MHz) δ (ppm) -2049 ppm. ES^+MS (m/z) 365 ($[M - 2N_3]^{2+}$), 407 ($[M - N_3]^+$), 450 ($[M + H]^+$), 856 ($[2M - N_3]^+$), 900 ($[2M + H]^+$), 1349 ($[3M + H]^+$).

***cis,cis,trans*-[Pt(*tz*)$_2$(N$_3$)$_2$(OH)$_2$]**

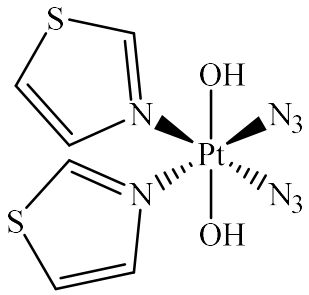

cis-[Pt(*tz*)$_2$(N$_3$)$_2$] (0.05 g, 0.11 mmol) was suspended in H_2O_2 (3.5 mL, 30% v/v). The reaction mixture was stirred in the dark at 45 °C for 2 hours. The reaction was quenched by dilution with distilled water and the solution lyophilized to give a yellow solid.

Yield: 0.030 g, 63.0%. ^{1}H NMR (D_2O, 400 MHz) δ (ppm) 9.27 (2H, doublet of doublets, CH), 7.93 (2H, doublet of doublets, CH), 7.86 (2H, doublet of doublets, CH) ppm. ^{13}C NMR (D_2O, 101 MHz) δ (ppm) 157.3, 139.5, 123.8 ppm. ^{195}Pt NMR (D_2O, 86 MHz) δ (ppm) 1038 ppm. ES^+MS (m/z) 484 ($[M + H]^+$), 506 ($[M + Na]^+$), 967 ($[2M + H]^+$), 1451 ($[3M + H]^+$).

***trans,trans*-[Pt(*pz*)$_2$Cl$_2$]**

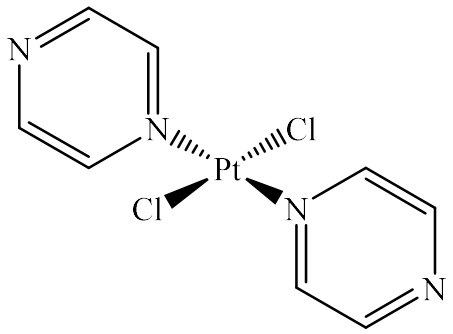

K_2PtCl_4 (0.50 g, 1.20 mmol) was dissolved in deionised water (12.5 mL). Pyrazine (0.45 g, 5.62 mmol) was added to the solution, and the reaction left to stir in the dark at 85 °C overnight. The reaction was allowed to cool before being filtered (IM). The solvent was removed under vacuum, and the residual white solid washed with diethyl ether. HCl (12.5 mL, 2 M) was added to the solid and the reaction left to stir in the dark at 75 °C for 24 hours. The yellow suspension was cooled on ice and filtered under suction. The yellow solid was washed with the minimum amount of cold water, ethanol and diethyl ether.

Yield: 0.480 g, 93.3%. ^{1}H NMR ($CDCl_3$, 400 MHz) δ (ppm) 8.85 (4H, doublet of doublets, CH), 8.58 (4H, doublet of doublets, CH) ppm. ^{13}C NMR ($CDCl_3$, 101 MHz) δ (ppm) 147.7, 147.1 ppm. ^{195}Pt NMR ($CDCl_3$, 86 MHz) δ (ppm) -2015 ppm. ES$^+$MS (*m/z*) 853 ($[2M + H]^+$), 875 ($[2M + Na]^+$), 1279 ($[3M + H]^+$).

***trans,trans*-[Pt(*pz*)$_2$(N$_3$)$_2$]**

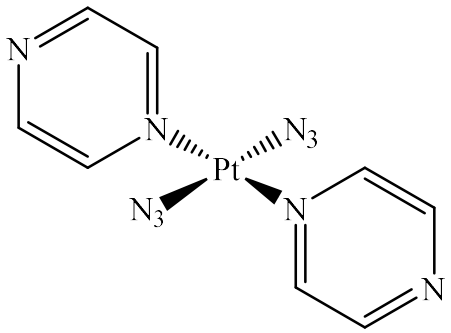

trans-[Pt(*pz*)$_2$Cl$_2$] (0.40 g, 0.94 mmol) was suspended in deionised water (70 mL). $AgNO_3$ (0.32 g, 1.90 mmol) was added and the reaction stirred in the dark at 60 °C overnight. The resulting suspension was filtered (celite and IM) to remove the AgCl. NaN_3 (0.31 g, 4.76 mmol) was added and reaction stirred in the dark at RT for 4 hours. Another aliquot of NaN_3 (0.31 g, 4.76 mmol) was added and the reaction stirred in the dark for a further 4 hours. The suspension was placed on ice, and the yellow solid collected by filtration under suction. The solid was washed with the minimum amount of cold water, ethanol and diethyl ether.

Yield: 0.225 g, 54.6%. ^{1}H NMR (CD_3CN, 400 MHz) δ (ppm) 8.85 (4H, doublet of doublets, CH), 8.82 (4H, doublet of doublets, CH) ppm. ^{13}C NMR (CD_3CN, 101 MHz) δ (ppm) 148.9, 147.1 ppm. ^{195}Pt NMR (CD_3CN, 86 MHz) δ (ppm) -2171 ppm. ES$^+$MS (*m/z*) 440 ($[M + H]^+$), 478 ($[M + K]^+$), 1275 ($[3M – N_3]^+$).

***trans,trans,trans*-[Pt(*pz*)$_2$(N$_3$)$_2$(OH)$_2$]**

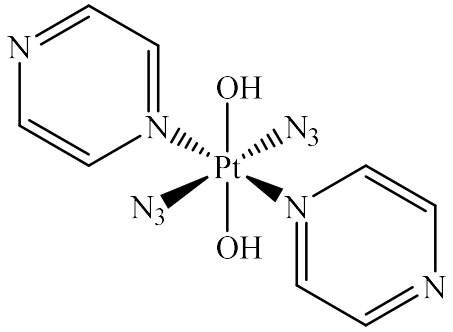

trans-[Pt(N$_3$)$_2$(*pz*)$_2$] (0.20 g, 0.46 mmol) was suspended in 30% H_2O_2 (14 mL, 30% v/v) and stirred in the dark at 45 °C for 3 hours. The solvent volume was reduced to ~2.5 mL under vacuum at 50 °C. Ethanol (10 mL) was added and the solution filtered (IM). Diethyl ether (30 mL) was added and the solution cooled in the freezer overnight. The crystals were isolated by filtration under suction.

Yield: 0.128 g, 67.3%. ^{1}H NMR (D_2O, 400 MHz) δ (ppm) 8.99 (4H, doublet of doublets, CH), 8.90 (4H, doublet of doublets, CH) ppm. ^{13}C NMR (D_2O, 101 MHz) δ (ppm) 148.7, 143.9 ppm. ^{195}Pt NMR (D_2O, 86 MHz) δ (ppm) 783 ppm. ES$^+$MS (*m/z*) 496 ($[M + Na]^+$), 947 ($[2M + H]^+$).

***cis,cis*-[Pt(*pz*)$_2$I$_2$]**

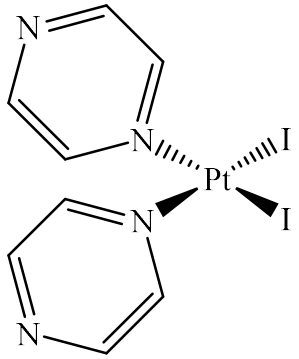

K_2PtCl_4 (0.25 g, 0.60 mmol) was dissolved in deionised water (19 mL). KI (1.00 g, 6.02 mmol) was added and the reaction stirred in the dark at RT for 1 hour. Pyrazine (0.096g, 1.20 mmol) was added and the reaction stirred in the dark at RT for a further 24 hours. The suspension was filtered under suction. The solid was washed with the minimum amount of cold water, ethanol and diethyl ether.

Yield: 0.306 g, 83.5%. ^{1}H NMR (DMF-d_7, 400 MHz) δ (ppm) 9.11 (4H, doublet of doublets, CH), 8.78 (4H, doublet of doublets, CH) ppm.

***cis,cis*-[Pt(*pz*)$_2$Cl$_2$]**

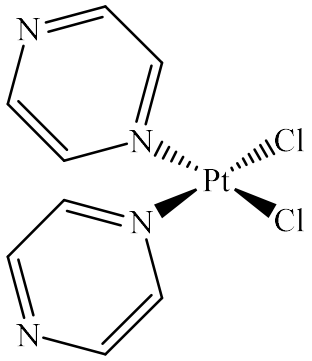

Method 1: *cis*-[Pt(*pz*)$_2$I$_2$] (0.25 g, 0.41 mmol) was suspended in deionised water (50 mL). $AgNO_3$ (0.14 g, 0.81 mmol) was added and the reaction left to stir in the dark at 60 °C for 24 hours. The suspension was filtered (celite and IM) to remove the AgI. NaCl (0.23 g, 4.01 mmol) was added to the filtrate and the reaction stirred in the dark at RT for 24 hours. The suspension was filtered under suction. Analysis of the solid was not possible due to the quantity being too low.

Method 2: *cis*-[Pt(*pz*)$_2$I$_2$] (0.30 g, 0.49 mmol) was suspended in a solution of deionised water and DMF (60 mL, 50:50 volume). $AgNO_3$ (0.17 g, 1.00 mmol) was added and the reaction left to stir in the dark at 60 °C for 24 hours. The suspension appeared as a black solid in a clear solution, indicating the formation of Pt^0.

***cis,cis*-[Pt(*pz*)$_2$(N$_3$)$_2$]**

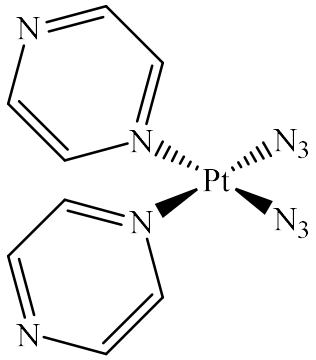

cis-[Pt(*pz*)$_2$I$_2$] (0.20 g, 0.33 mmol) was suspended in deionised water (40 mL). $AgNO_3$ (0.11 g, 0.66 mmol) was added and the reaction left to stir in the dark at 60 °C overnight. The suspension was filtered (celite and IM) to remove the AgI. NaN_3 (0.14 g, 2.14 mmol) was added and the reaction stirred in the dark at RT for 24 hours. The suspension was filtered under suction. Analysis of the solid was not possible due to the quantity being too low.

Liposome Synthesis and Loading

Calcium Acetate Method - Standard

DPPC (17.66 mg), cholesterol (6.2 mg), DSPE-PEG2000^{+} (12.5 mg) and DiO (100 µL of 2 mg mL^{-1} in $CHCl_3$) were added to a 250 mL round bottom flask with 1 mL of chloroform and swirled to dissolve. The solution was dried to give a thin film and then reydrated film with 1.2 mL of 200 mM calcium acetate solution, vortexing at 60 °C for 20 mins. The solution was frozen on liquid N_2, then thawed using a 60 °C water bath with 10 seconds of vortexing as it was warming. Five of these freeze-thaw cycles were completed, leaving the flask at each extreme for 10 mins. The solution was kept at 60 °C until extrusion, and the syringes and extrusion block pre-heated to 65 °C. The solution was extruded 11 times through a 400 nm

filter, and 11 times through a 200 nm filter. The extraliposomal calcium acetate was replaced with 200 mM sodium sulphate by dialysis. 3 cycles of dialysis against 200 times the volume of liposome solution were completed using a float-a-lyser G2 0.5-1 kDa pre-prepared dialysis 1ml tube, stirring at 40 °C for 1 hour. A fourth cycle of dialysis against 400 times the volume at ambient temperature was left stirring overnight. The liposomes were transferred to a clean flask and incubated with a concentrated solution of iproplatin (15 mg mL^{-1}) in 200 mM sodium sulphate for 1 hour at 55 °C, before cooling to 4 °C. The liposomes were filtered using pre-packed gel column (Sephadex G-25 in PD-10) to remove any unencapsulated drug, and stored at 4 °C.

Calcium Acetate Method – Cross-linked

DPPC (8.8 mg), 23:2 Diyne PC (11 mg), cholesterol (6.2 mg), and DSPE-PEG2000 (12.5 mg) were added to a 250 mL round bottom flask with 1 mL of chloroform and swirled to dissolve. The solution was dried to give a thin film and then reydrated film with 1.2 mL of 200 mM calcium acetate solution, vortexing at 60 °C for 20 mins. The solution was frozen on liquid N_2, then thawed using a 60 °C water bath with 10 seconds of vortexing as it was warming. Five of these freeze-thaw cycles were completed, leaving the flask at each extreme for 10 mins. The solution was kept at 60 °C until extrusion, and the syringes and extrusion block pre-heated to 65 °C. The solution was extruded 11 times through a 400 nm filter, and 11 times through a 200 nm filter. The extraliposomal calcium acetate was replaced with 200 mM sodium sulphate by dialysis. 3 cycles of dialysis against 200 times the volume of liposome solution were completed using a float-a-lyser G2 0.5-1 kDa pre-prepared dialysis 1ml tube, stirring at 40 °C for 1 hour. A fourth cycle of dialysis against 400 times the volume at ambient temperature was left stirring overnight. The liposomes were transferred to a clean flask and incubated with a

concentrated solution of iproplatin (15 mg mL^{-1}) in 200 mM sodium sulphate for 1 hour at 55 °C, before cooling to 4 °C. The liposomes were then filtered using a pre-packed gel column (Sephadex G-25 in PD-10), using sodium sulphate as the eluent, to remove any unencapsulated drug. The liposomes were then irradiated with UV-light (254 nm, 28 W) for 70 mins, and filtered again though a pre-packed gel column. The liposomes were stored at 4 °C.

Calcium Acetate Method – Microbubble-conjugation

DPPC (17.66 mg), cholesterol (6.2 mg), DSPE-PEG Azide (12.5 mg) and DiO (100 μL of 2 mg mL^{-1} in $CHCl_3$) were added to a 250 mL round bottom flask with 1 mL of chloroform and swirled to dissolve. The solution was dried to give a thin film and then reydrated film with 1.2 mL of 200 mM calcium acetate solution, vortexing at 60 °C for 20 mins. The solution was frozen on liquid N_2, then thawed using a 60 °C water bath with 10 seconds of vortexing as it was warming. Five of these freeze-thaw cycles were completed, leaving the flask at each extreme for 10 mins. The solution was kept at 60 °C until extrusion, and the syringes and extrusion block pre-heated to 65 °C. The solution was extruded 11 times through a 400 nm filter, and 11 times through a 200 nm filter. The extraliposomal calcium acetate was replaced with 200 mM sodium sulphate by dialysis. 3 cycles of dialysis against 200 times the volume of liposome solution were completed using a float-a-lyser G2 0.5-1 kDa pre-prepared dialysis 1ml tube, stirring at 40 °C for 1 hour. A fourth cycle of dialysis against 400 times the volume at ambient temperature was left stirring overnight. For blank liposomes, the synthesis was stopped at this point. For drug loaded liposomes, the suspension was transferred to a clean flask and incubated with a concentrated solution of iproplatin (15 mg mL^{-1}) in 200 mM sodium sulphate for 1 hour at 55 °C, before cooling to 4 °C. The liposomes were filtered using pre-

packed gel column (Sephadex G-25 in PD-10) to remove any unencapsulated drug, and stored at 4 °C.

Ammonium Sulphate Method - Standard

DPPC (17.66 mg), cholesterol (6.20 mg), DSPE-PEG2000 (12.50 mg), and DiO (100 μL of 2 mg mL in $CHCl_3$) were added to a 250 mL round bottom flask with 1 mL of chloroform and swirled to dissolve. The solution was dried to give a thin film and then reydrated film with 1.2 mL of 250 mM ammonium sulphate solution, vortexing at 60 °C for 20 mins. The solution was frozen on liquid N_2, then thawed using a 60 °C water bath with 10 seconds of vortexing as it was warming. Five of these freeze-thaw cycles were completed, leaving the flask at each extreme for 10 mins. The solution was kept at 60 °C until extrusion, and the syringes and extrusion block pre-heated to 65 °C. The solution was extruded 11 times through a 400 nm filter, and 11 times through a 200 nm filter. The extraliposomal ammonium sulphate was replaced with isosmotic sodium chloride (375 mM) by eluting through a pre-packed gel column (Sephadex G-25 in PD-10). The liposomes were transferred to a clean flask and incubated with a concentrated solution of iproplatin (15 mg mL^{-1}) in 375 mM sodium chloride for 1 hour at 55 °C, before cooling to 4 °C for storage.

Ammonium Sulphate Method – Cross-linked

DPPC (8.8 mg), 23:2 Diyne PC (11 mg), cholesterol (6.2 mg), and DSPE-PEG2000 (12.5 mg) were added to a 250 mL round bottom flask with 1 mL of chloroform and swirled to dissolve. The solution was dried to give a thin film and then reydrated film with 1.2 mL of 250 mM ammonium sulphate solution, vortexing at 60 °C for 20 mins. The solution was frozen on liquid N_2, then thawed using a 60 °C water bath with 10 seconds of vortexing as it was warming. Five

of these freeze-thaw cycles were completed, leaving the flask at each extreme for 10 mins. The solution was kept at 60 °C until extrusion, and the syringes and extrusion block pre-heated to 65 °C. The solution was extruded 11 times through a 400 nm filter, and 11 times through a 200 nm filter. The extraliposomal ammonium sulphate was replaced with isosmotic sodium chloride (375 mM) by eluting through a pre-packed gel column (Sephadex G-25 in PD-10). The liposomes were transferred to a clean flask and incubated with a concentrated solution of iproplatin (15 mg mL^{-1}) in 375 mM sodium chloride for 1 hour at 55 °C, before cooling to 4 °C for storage. The liposomes were then filtered using a pre-packed gel column (Sephadex G-25 in PD-10), using sodium chloride as the eluent, to remove any unencapsulated drug. The liposomes were then irradiated with UV-light (254 nm, 28 W) for 70 mins, and filtered again though a pre-packed gel column. The liposomes were stored at 4 °C.

Microbubble Synthesis – For Unconjugated Microbubbles

DPPC (7.00 mg), DSPE-mPEG(2000) (1.50 mg), and DSPE-PEG-DBCO (1.65 mg) were dissolved in 1 mL chloroform in a 9:0.5:0.5 molar ratio. The solution was dried to give a thin film and then rehydrated with 2.5 mL of a solution of PBS:glycerol:propylene glycol (8:1:1). 250 μL of the solution was placed into a 0.5 mL Eppendorf and the headspace filled with perfluorobutane (PFB) gas. The microbubbles were formed using a capsule mixer (Vialmix) shaking for 45 seconds before cooling on ice.

Microbubble Synthesis – For Liposome Conjugated Microbubbles

DPPC (7.00 mg), DSPE-mPEG(2000) (1.50 mg), and DSPE-PEG-DBCO (1.65 mg) were dissolved in 1 mL chloroform in a 9:0.5:0.5 molar ratio. The solution was dried to give a thin film and then rehydrated with 2.5 mL of a solution of PBS:glycerol:propylene glycol (8:1:1).

1 mL of this solution was added to 200 μL of a liposome solution formed by the calcium acetate method (after dialysis with sodium sulphate), and 300 μL of a solution of PBS:glycerol:propylene glycol (8:1:1). The solution was left to stir for 2 hours (RT, 480 rpm) so the click reaction could occur between the liposomal-N_3 group and the DSPE-PEG-DBCO.

Appendix

A.1 Structures

Cholesterol

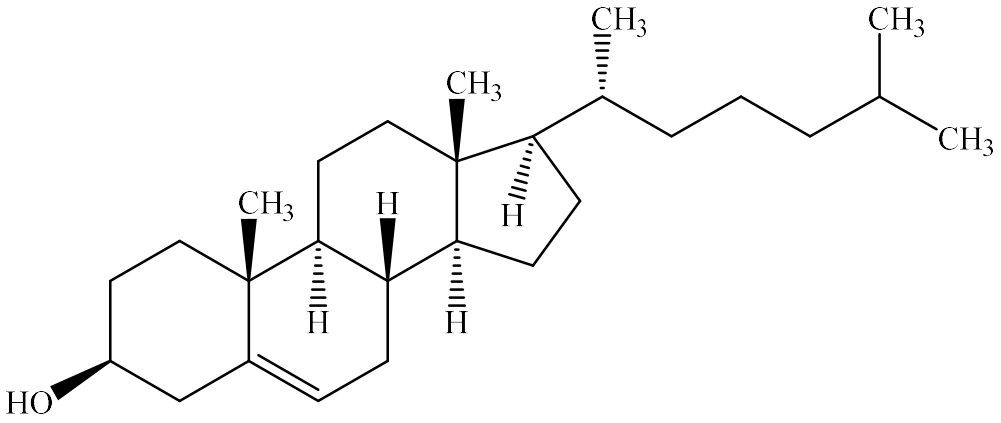

DiO

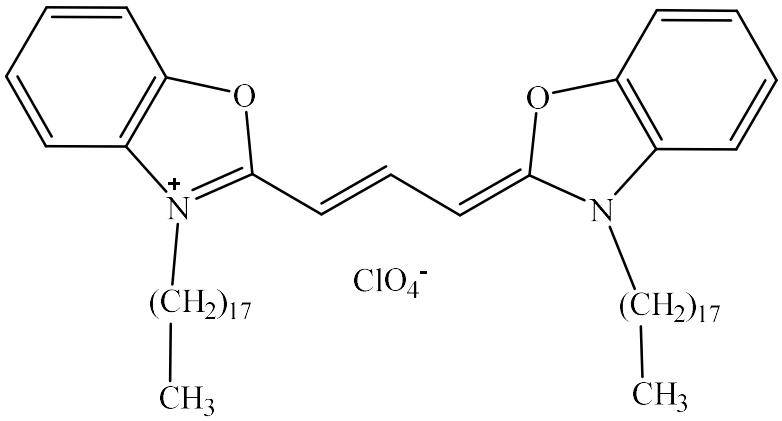

DPPC

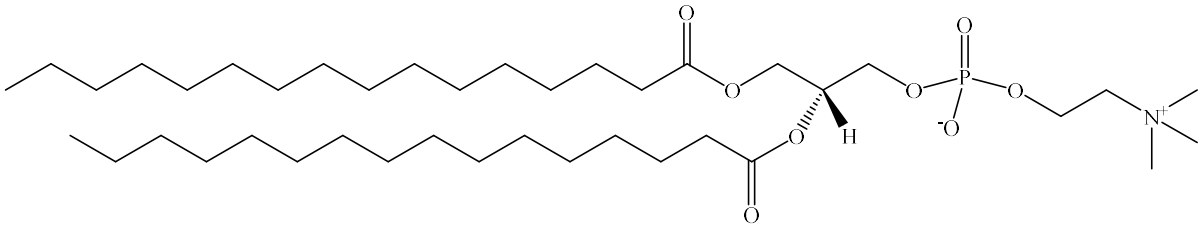

DBPC

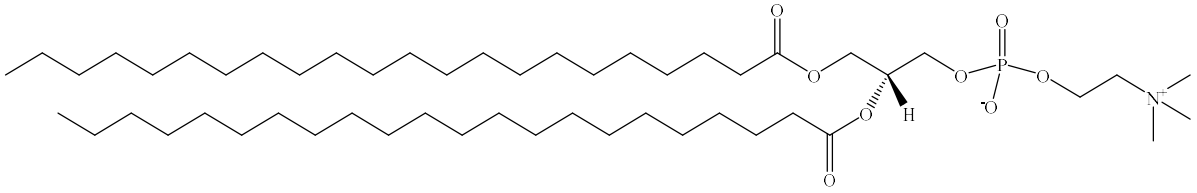

DSPE-mPEG(2000)

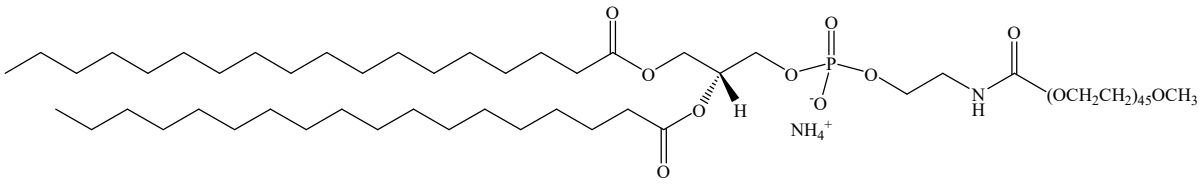

DSPE-PEG(2000) Azide

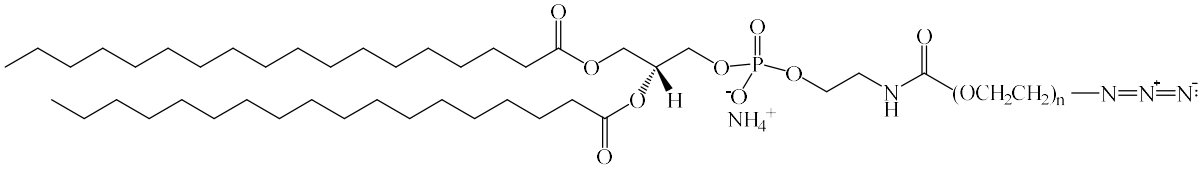

DSPE-PEG(2000)-DBCO

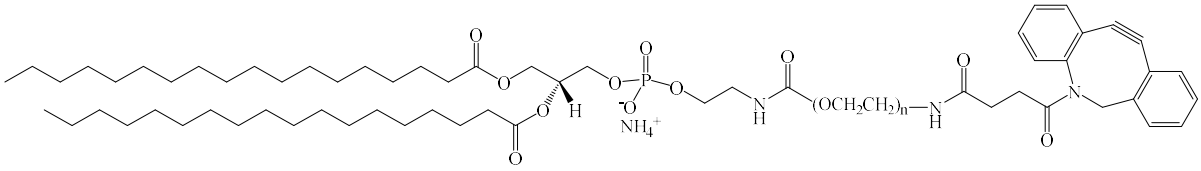

23:2 Diyne PC

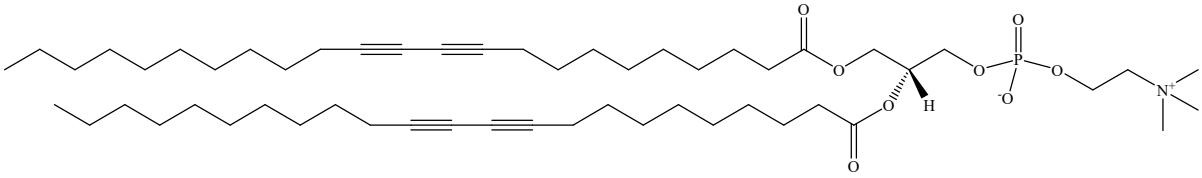

PEG 40 S

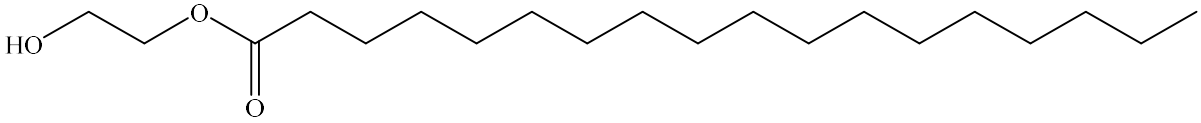

A.2 NMR Spectroscopy

Iproplatin

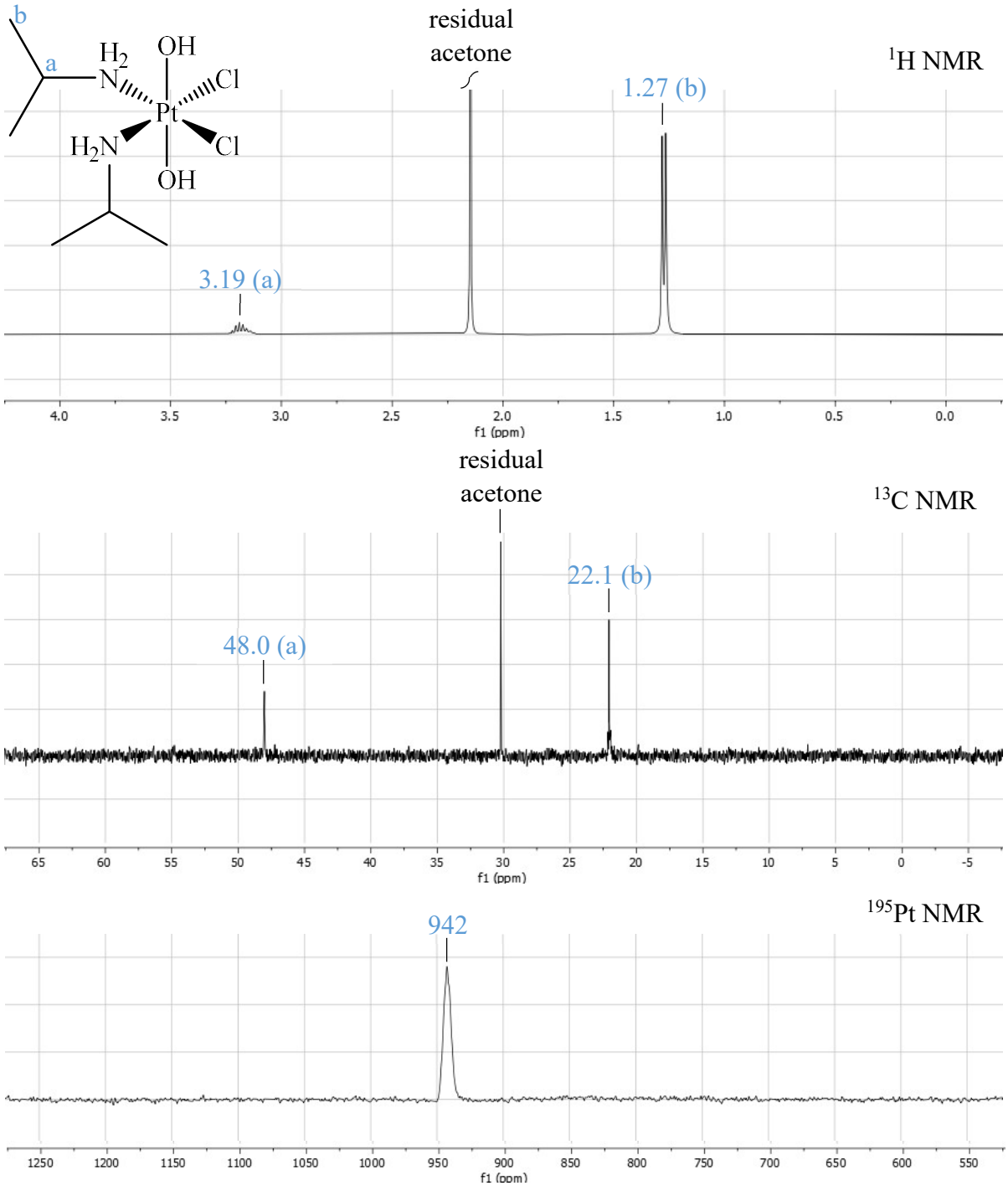

Figure A2.1 Assigned NMR spectra for iproplatin run in D_2O, top to bottom: ^{1}H NMR, ^{13}C NMR, and ^{195}Pt NMR spectra.

For the ^{1}H NMR spectra provided in Figure A2.1, the OH and NH_2 protons are masked by the D_2O solvent peak at 4.70 ppm. Residual acetone from washing can be seen in the ^{1}H and ^{13}C NMR spectra, with the second acetone peak in the ^{13}C NMR spectrum appearing at 215.4 ppm. Finally, the ^{195}Pt NMR spectrum shows a single resonance in the Pt^{IV} region (942 ppm) which is significantly downfield shifted compared to the Pt^{II} precursor (-2211 ppm).

***trans,trans,trans*-[Pt(*py*)$_2$(N$_3$)$_2$(OH)$_2$]**

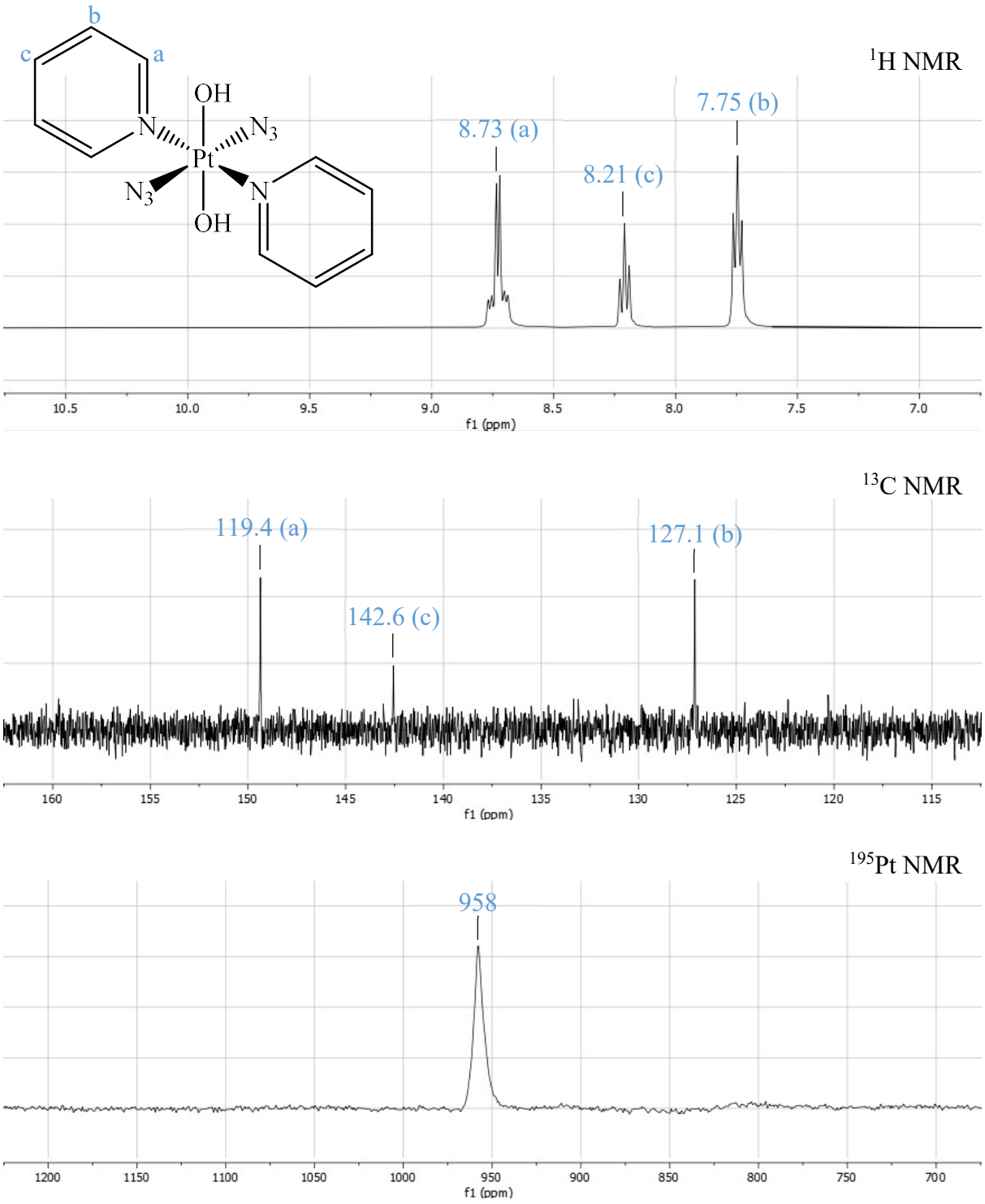

Figure A2.2 Assigned NMR spectra for trans,trans,trans-[Pt(py)$_2$(N$_3$)$_2$(OH)$_2$] run in D$_2$O, top to bottom: ^{1}H NMR, ^{13}C NMR, and ^{195}Pt NMR spectra.

For the ^{1}H NMR spectra provided in Figure A2.2, the OH protons are masked by the D_2O solvent peak at 4.70 ppm. The ^{195}Pt NMR spectrum shows a single resonance in the Pt^{IV} region (968 ppm) which is significantly downfield shifted compared to the Pt^{II} precursor (-2096 ppm).

***cis,cis*-[Pt(*tz*)$_2$I$_2$]**

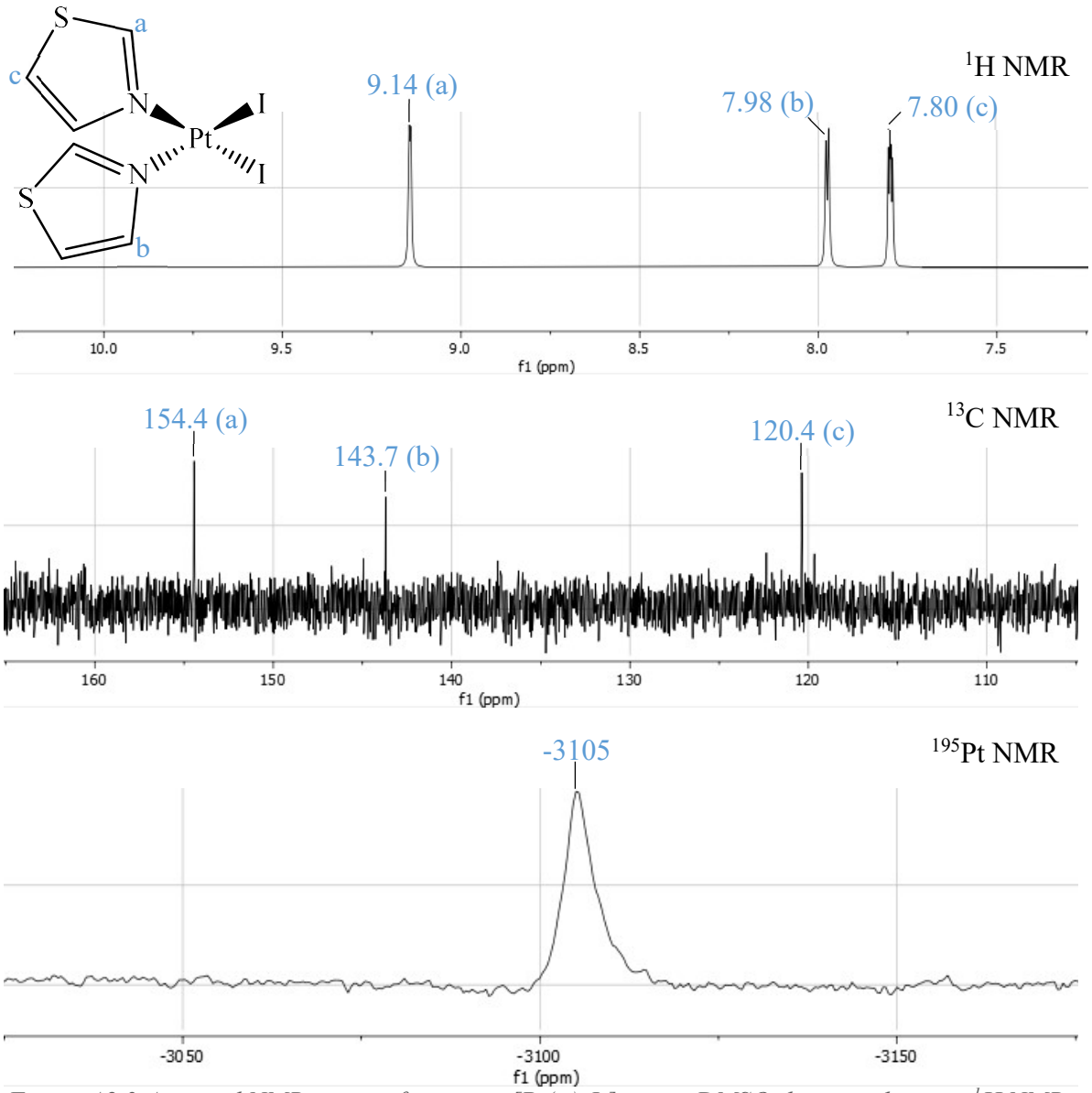

Figure A2.3 Assigned NMR spectra for cis,cis-[Pt(tz)$_2$I$_2$] run in DMSO-d$_6$, top to bottom: ^{1}H NMR, ^{13}C NMR, and ^{195}Pt NMR spectra.

***cis,cis*-[Pt(*tz*)$_2$Cl$_2$]**

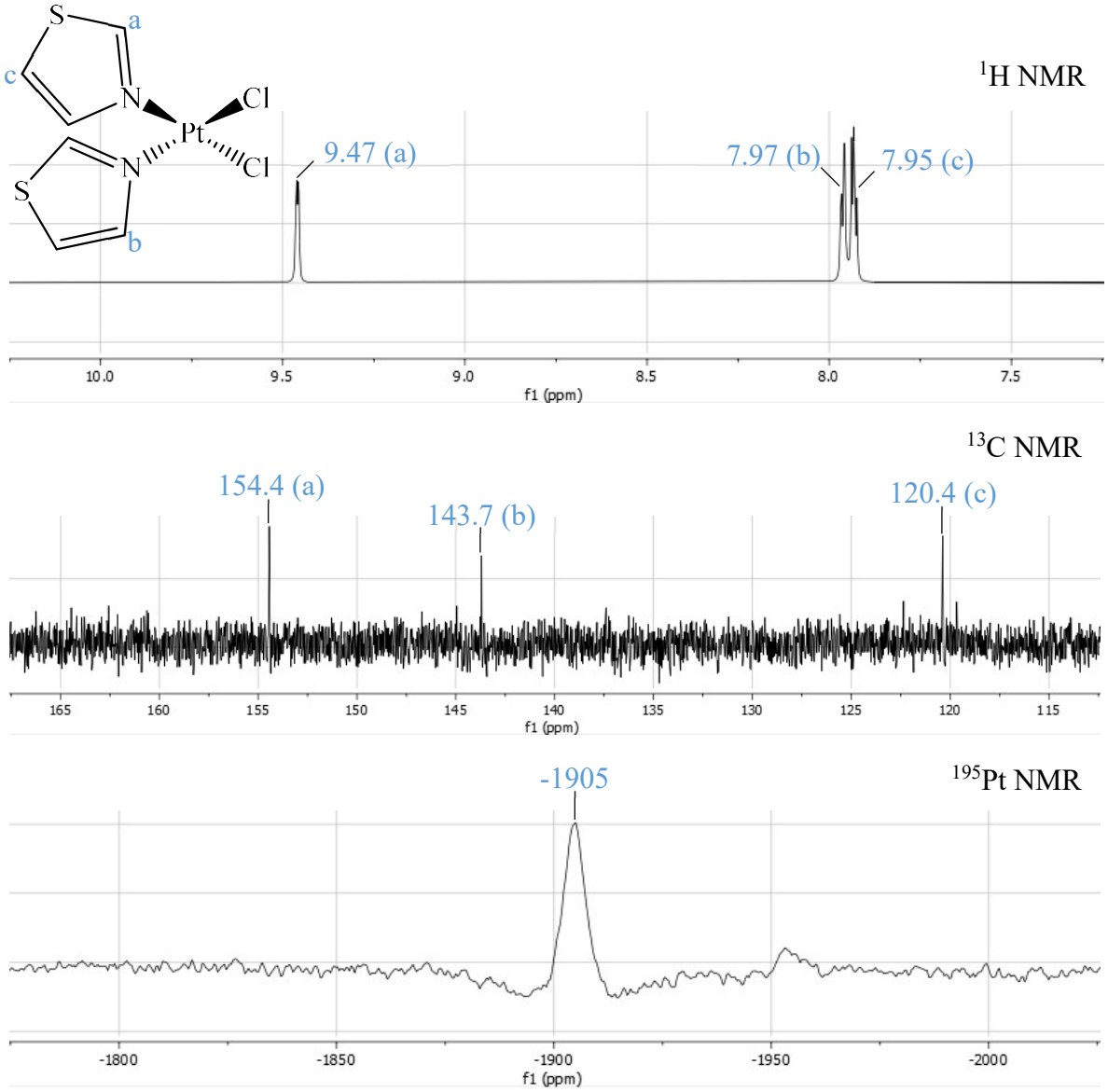

Figure A2.4 Assigned NMR spectra for cis,cis-[Pt(tz)2Cl2] run in DMSO-d_6, top to bottom: ^{1}H NMR, ^{13}C NMR, and ^{195}Pt NMR spectra.

***cis,cis*-[Pt(*tz*)$_2$(N$_3$)$_2$]**

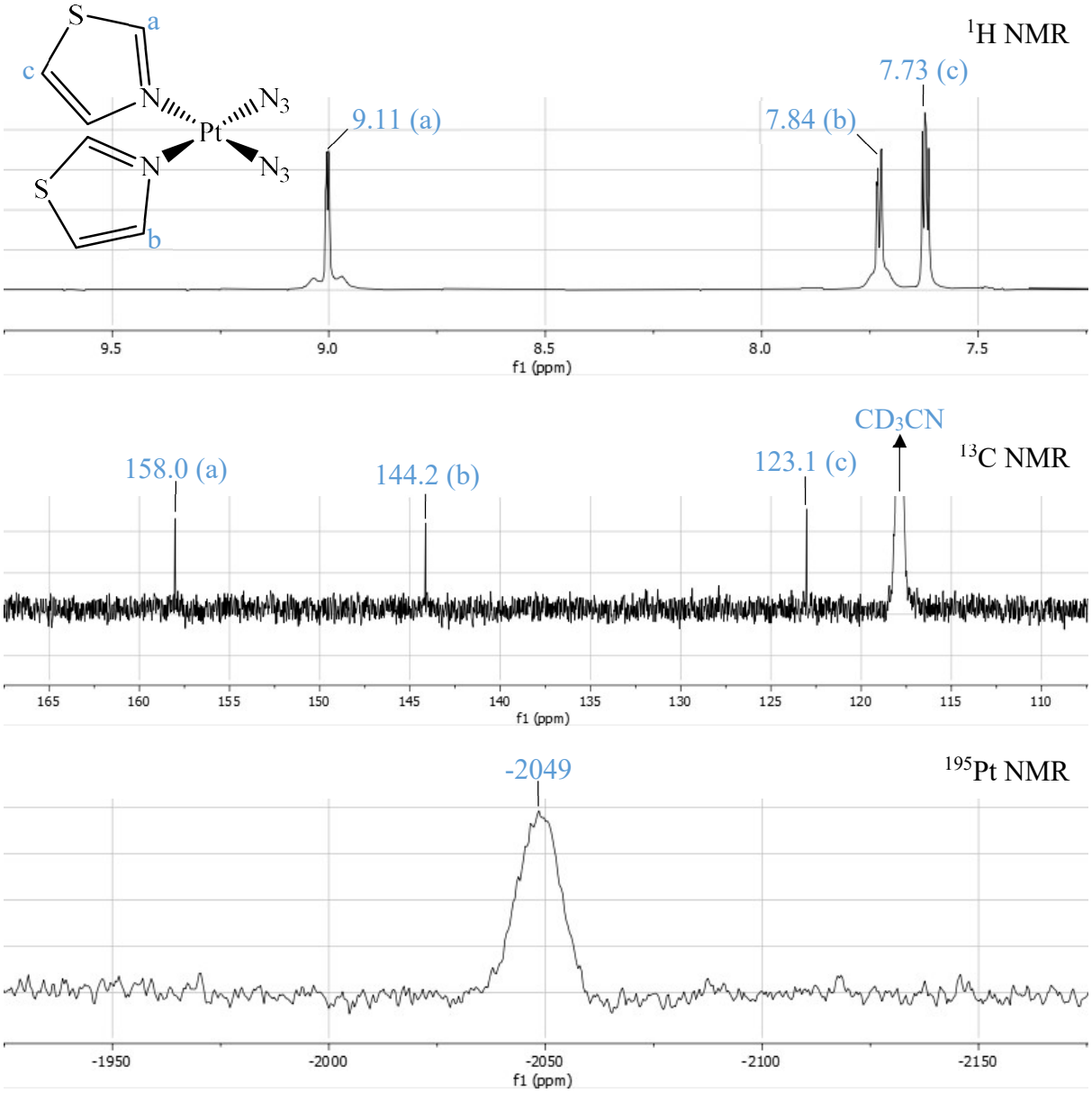

Figure A2.5 Assigned NMR spectra for cis,cis-[Pt(tz)$_2$(N$_3$)$_2$] run in CD$_3$CN, top to bottom: ^{1}H NMR, ^{13}C NMR, and ^{195}Pt NMR spectra.

***cis,cis,trans*-[Pt(*tz*)$_2$(N$_3$)$_2$(OH)$_2$]**

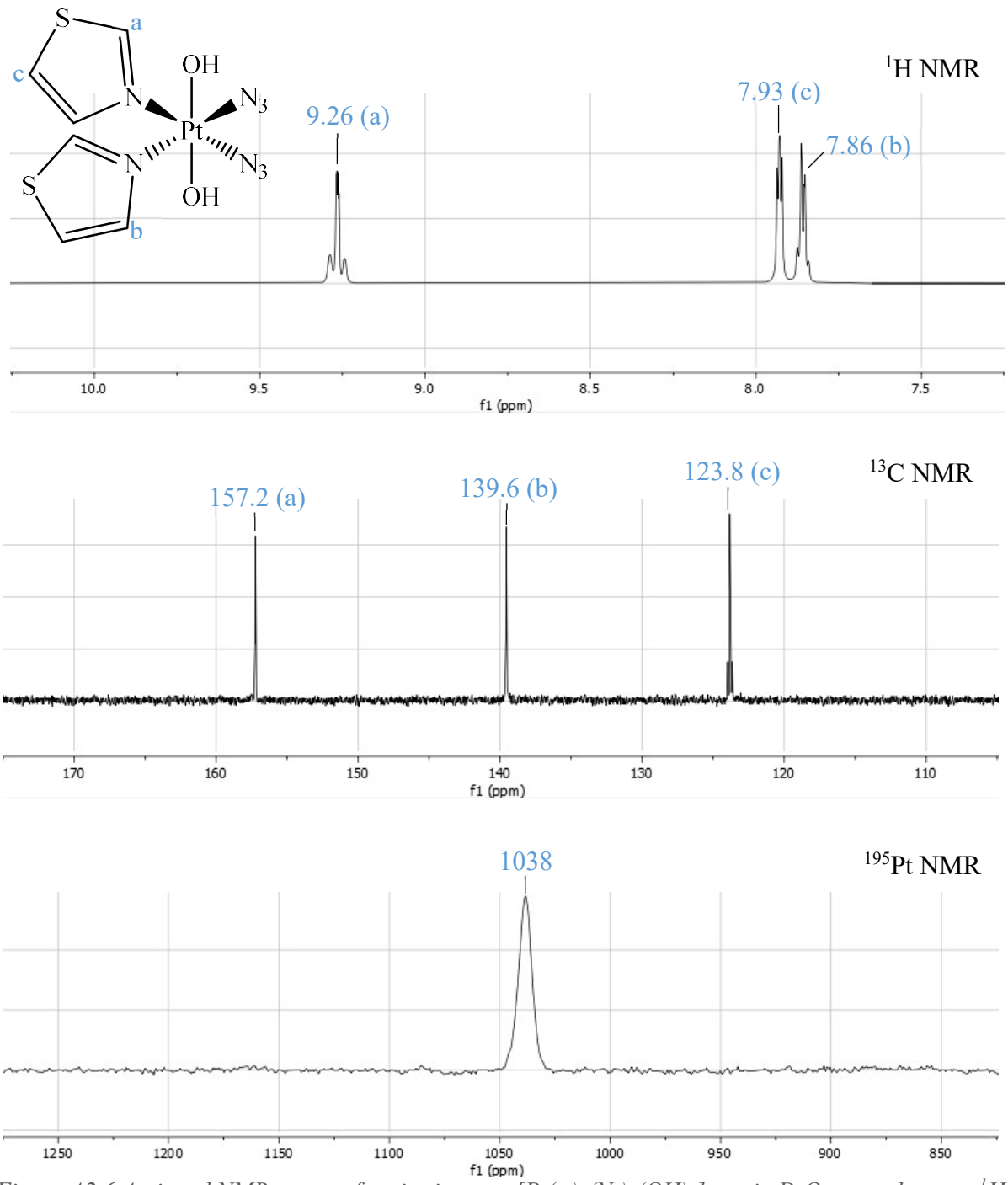

Figure A2.6 Assigned NMR spectra for cis,cis,trans-[Pt(tz)$_2$(N$_3$)$_2$(OH)$_2$] run in D$_2$O, top to bottom: ^{1}H NMR, ^{13}C NMR, and ^{195}Pt NMR spectra.

For the ^{1}H NMR spectra provided in Figure A2.6, the OH protons are masked by the D_2O solvent peak at 4.70 ppm. In the ^{1}H-NMR spectrum, sharp Pt satellites can be seen either side of resoances a and b. These are the protons on the nitrogen adjacent carbons in the thiazole ligands, and the linewidth indicates that the complex is Pt^{IV}. Finally, the ^{195}Pt NMR spectrum shows a single resonance in the Pt^{IV} region (1038 ppm) which is significantly downfield shifted compared to the Pt^{II} precursor (-2046 ppm).

***trans,trans*-[Pt(*pz*)$_2$Cl$_2$]**

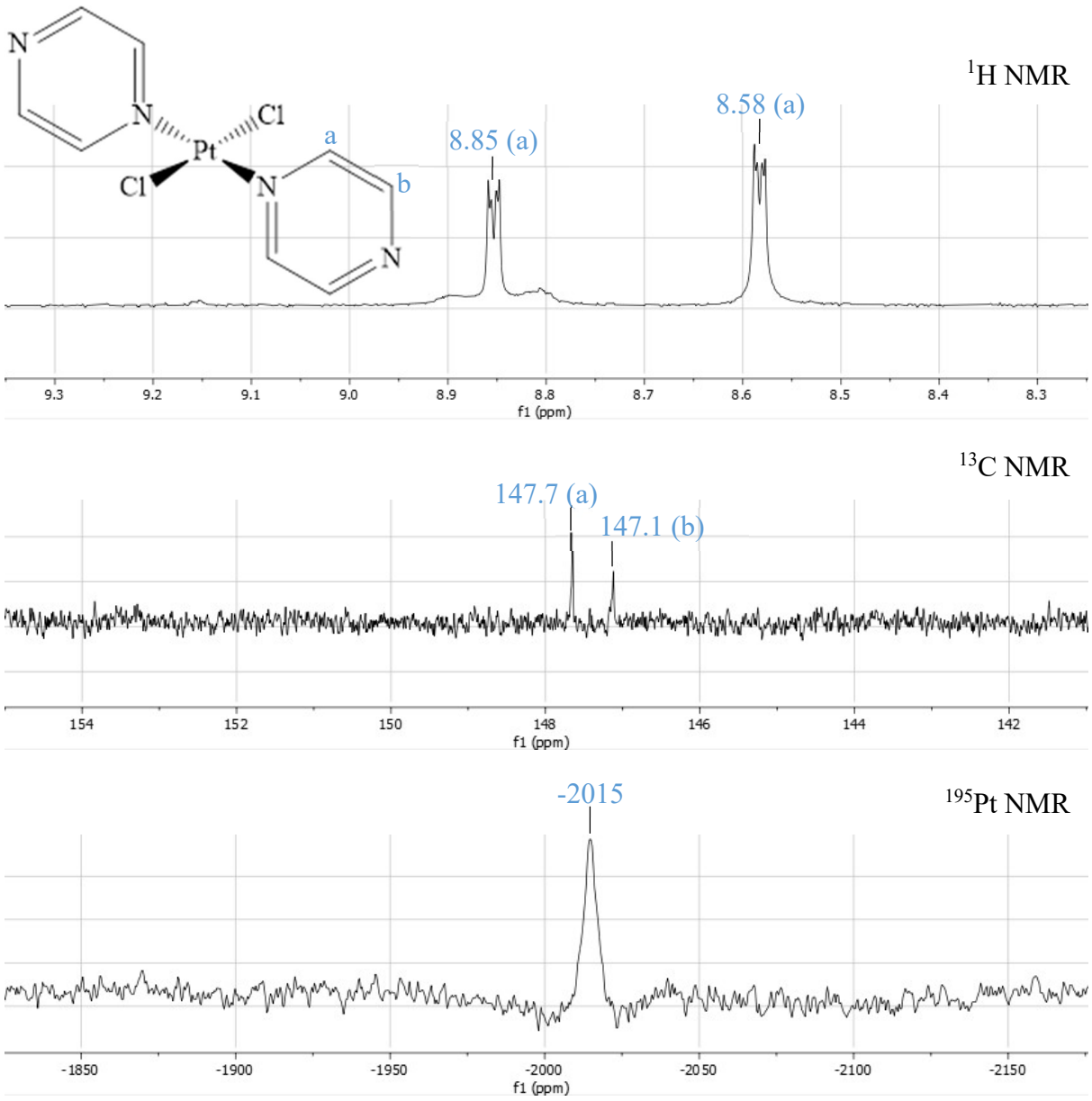

Figure A2.7 Assigned NMR spectra for trans,trans-[Pt(pz)$_2$Cl$_2$] run in CDCl$_3$, top to bottom: ^{1}H NMR, ^{13}C NMR, and ^{195}Pt NMR spectra.

***trans,trans*-[Pt(*pz*)$_2$(N$_3$)$_2$]**

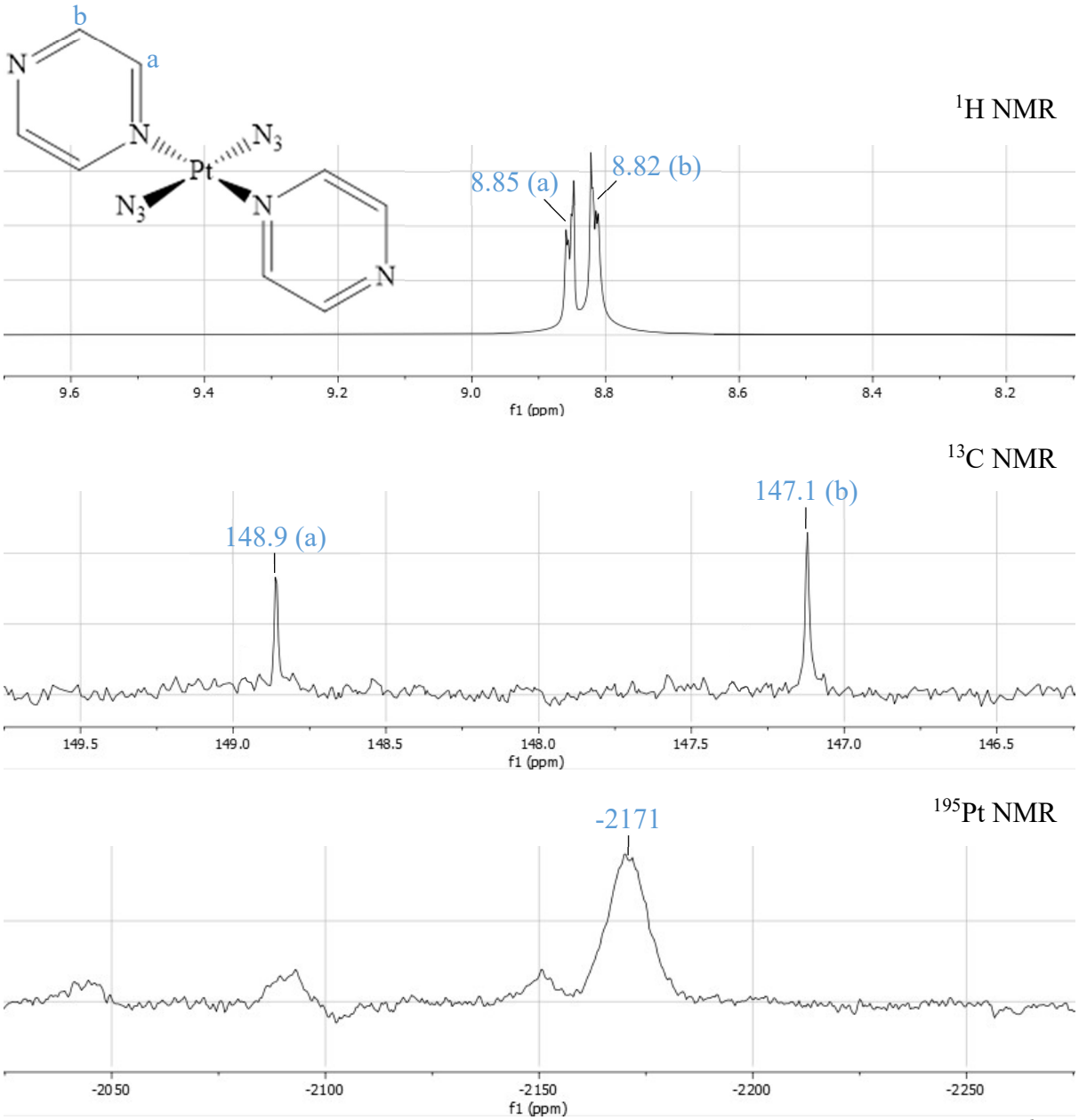

Figure A2.8 Assigned NMR spectra for trans,trans-[Pt(pz)$_2$(N$_3$)$_2$] run in CD$_3$CN, top to bottom: ^{1}H NMR, ^{13}C NMR, and ^{195}Pt NMR spectra.

***trans,trans,trans*-[Pt(*pz*)$_2$(N$_3$)$_2$(OH)$_2$]**

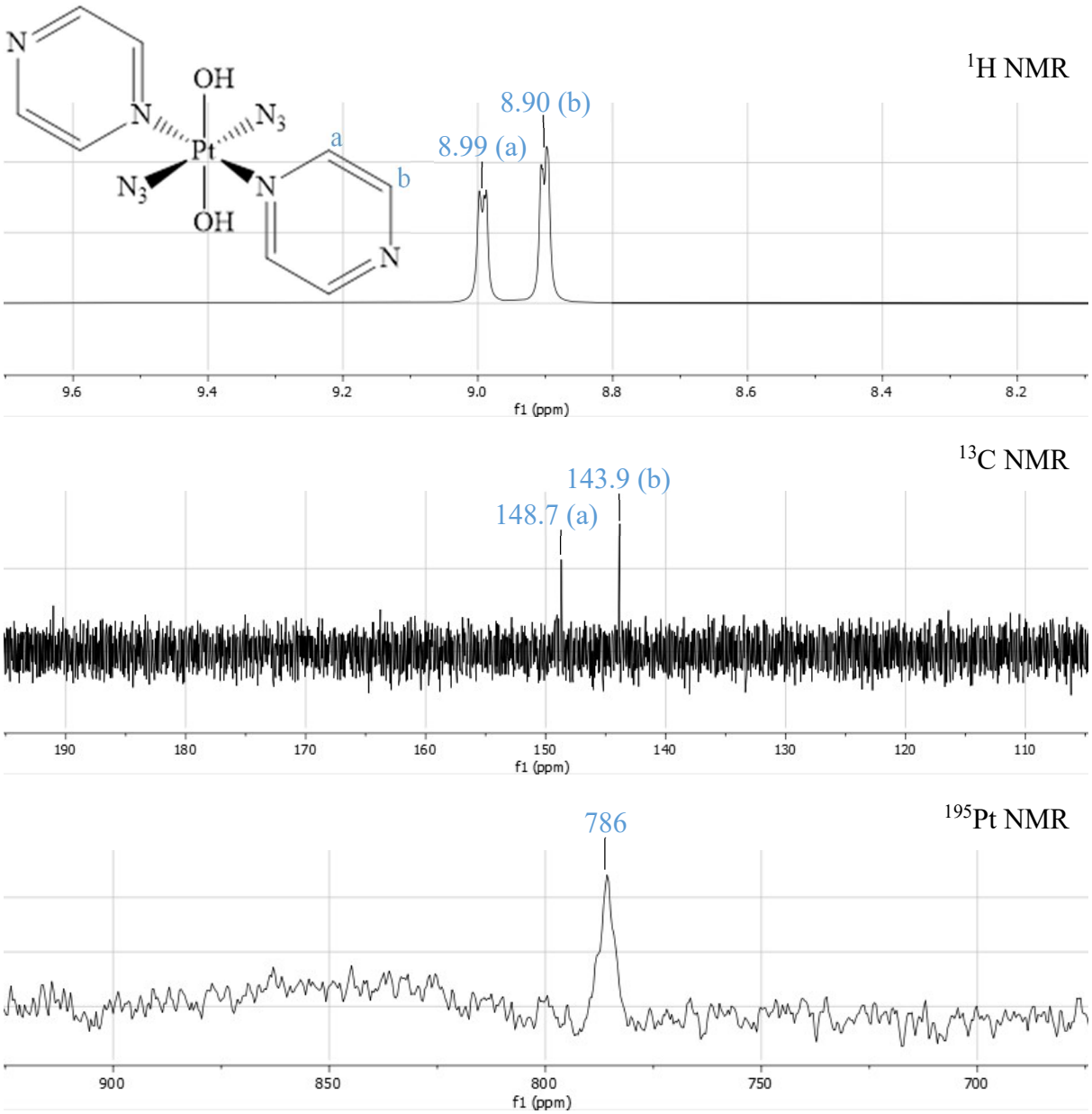

Figure A2.9 Assigned NMR spectra for trans,trans,trans-[Pt(pz)$_2$(N$_3$)$_2$(OH)$_2$] run in D$_2$O, top to bottom: ^{1}H NMR, ^{13}C NMR, and ^{195}Pt NMR spectra.

For the ^{1}H NMR spectra provided in Figure A2.9, the OH protons are masked by the D$_2$O solvent peak at 4.70 ppm. The ^{195}Pt NMR spectrum shows a single resonance in the Pt^{IV} region (786 ppm) which is significantly downfield shifted compared to the Pt^{II} precursor (-2171 ppm). Due to the complex being sparingly soluble in most solvents, the signal to noise ratio is lower in the presented spectra.

A.3 Mass Spectrometry

Iproplatin

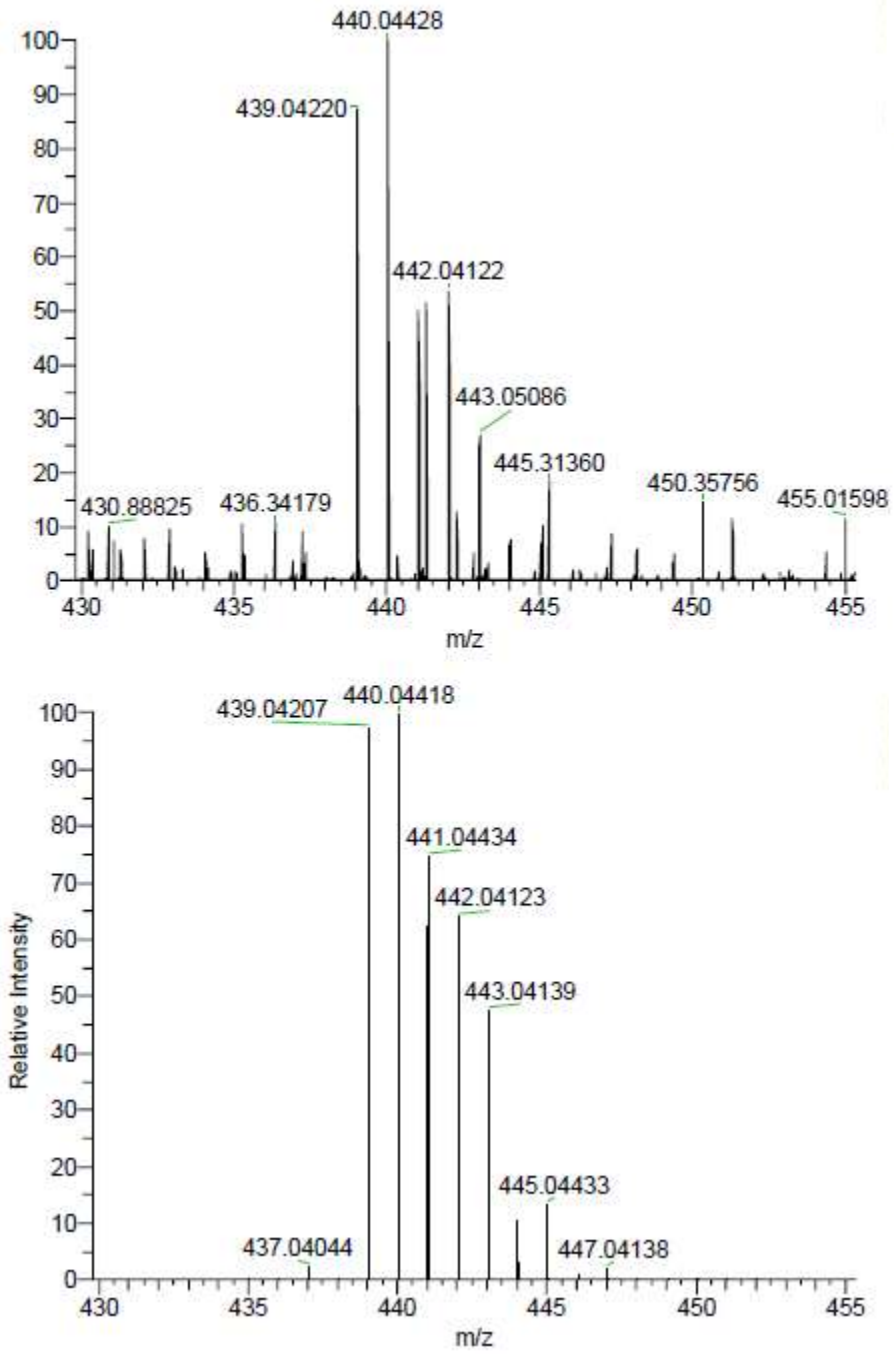

Figure A3.1 Accurate ESI-MS for iproplatin, fragment $[M+Na]^+$ (M_r = 440.04, accuracy 0.2 ppm).

***trans,trans,trans*-[Pt(*py*)$_2$(N$_3$)$_2$(OH)$_2$]**

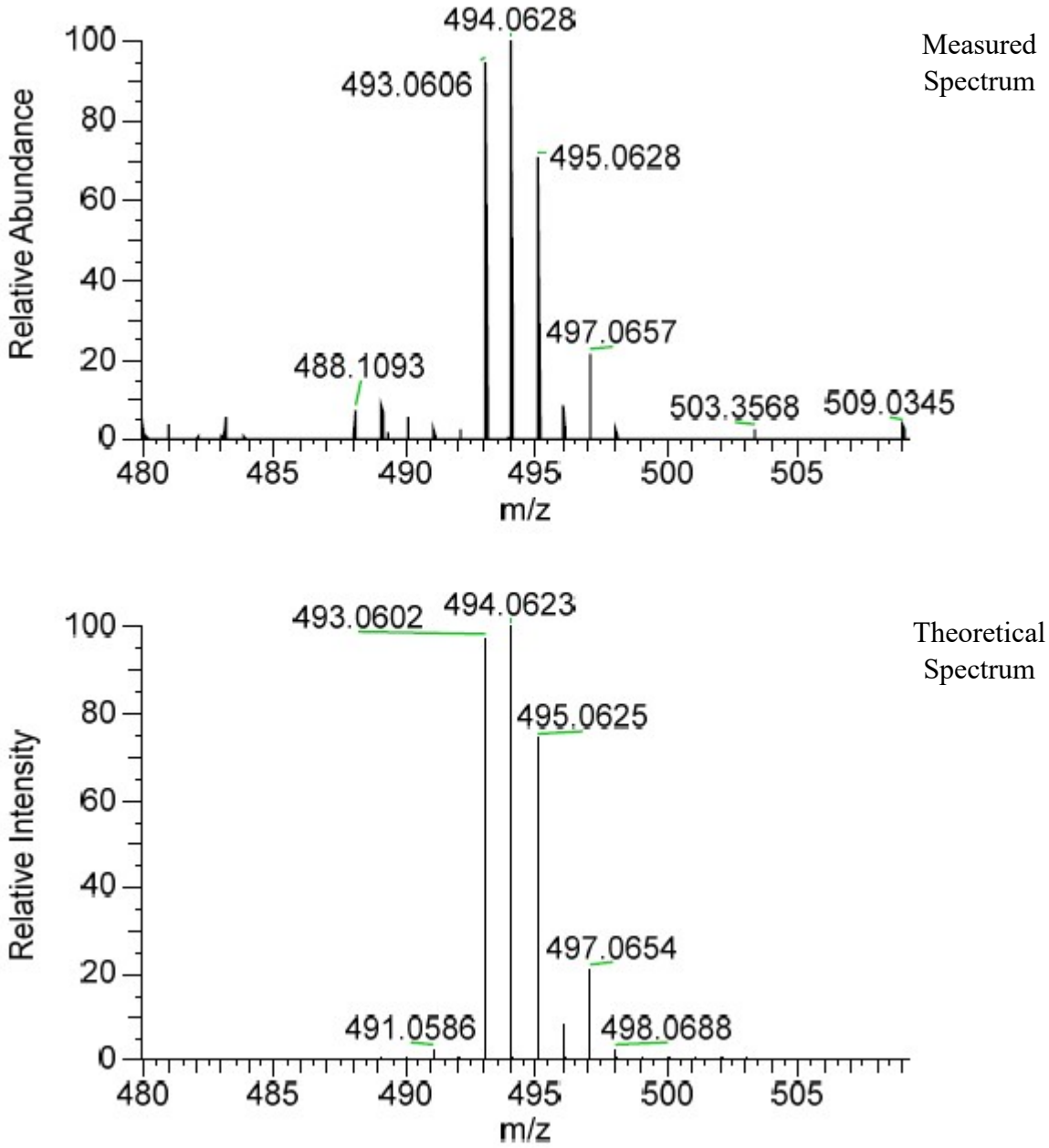

Figure A3.2 Accurate ESI-MS for trans,trans,trans-[Pt(py)$_2$(N$_3$)$_2$(OH)$_2$], fragment [M+Na]$^+$ (M_r = 494.06, accuracy 0.8 ppm).

***cis,cis,trans*-[Pt(*tz*)$_2$(N$_3$)$_2$(OH)$_2$]**

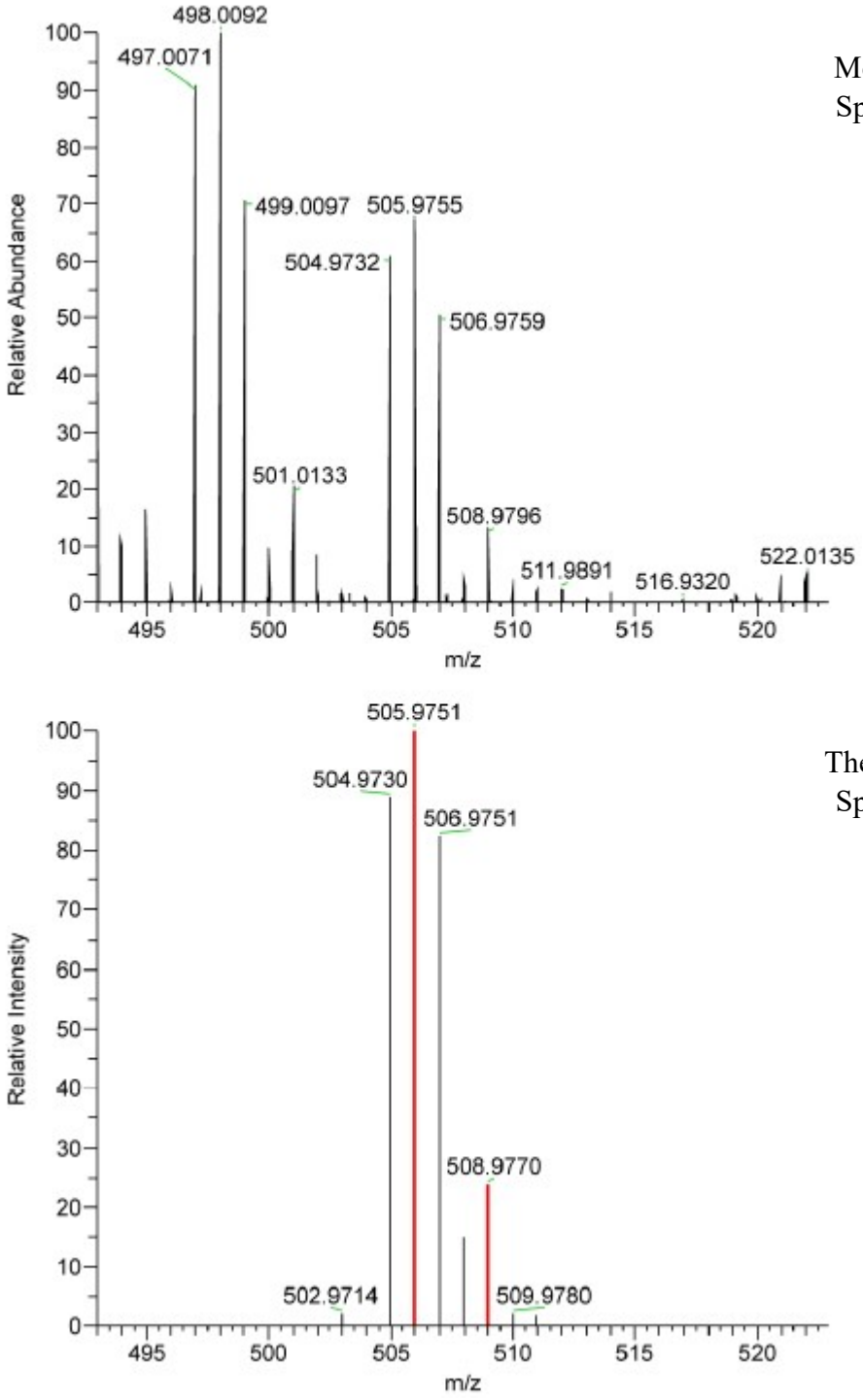

Figure A3.3 Accurate ESI-MS for cis,cis,trans-[Pt(tz)$_2$(N$_3$)$_2$(OH)$_2$], fragment [M+Na]$^+$ (M_r = 505.98, accuracy 0.2 ppm).

***trans,trans,trans*-[Pt(*pz*)$_2$(N$_3$)$_2$(OH)$_2$]**

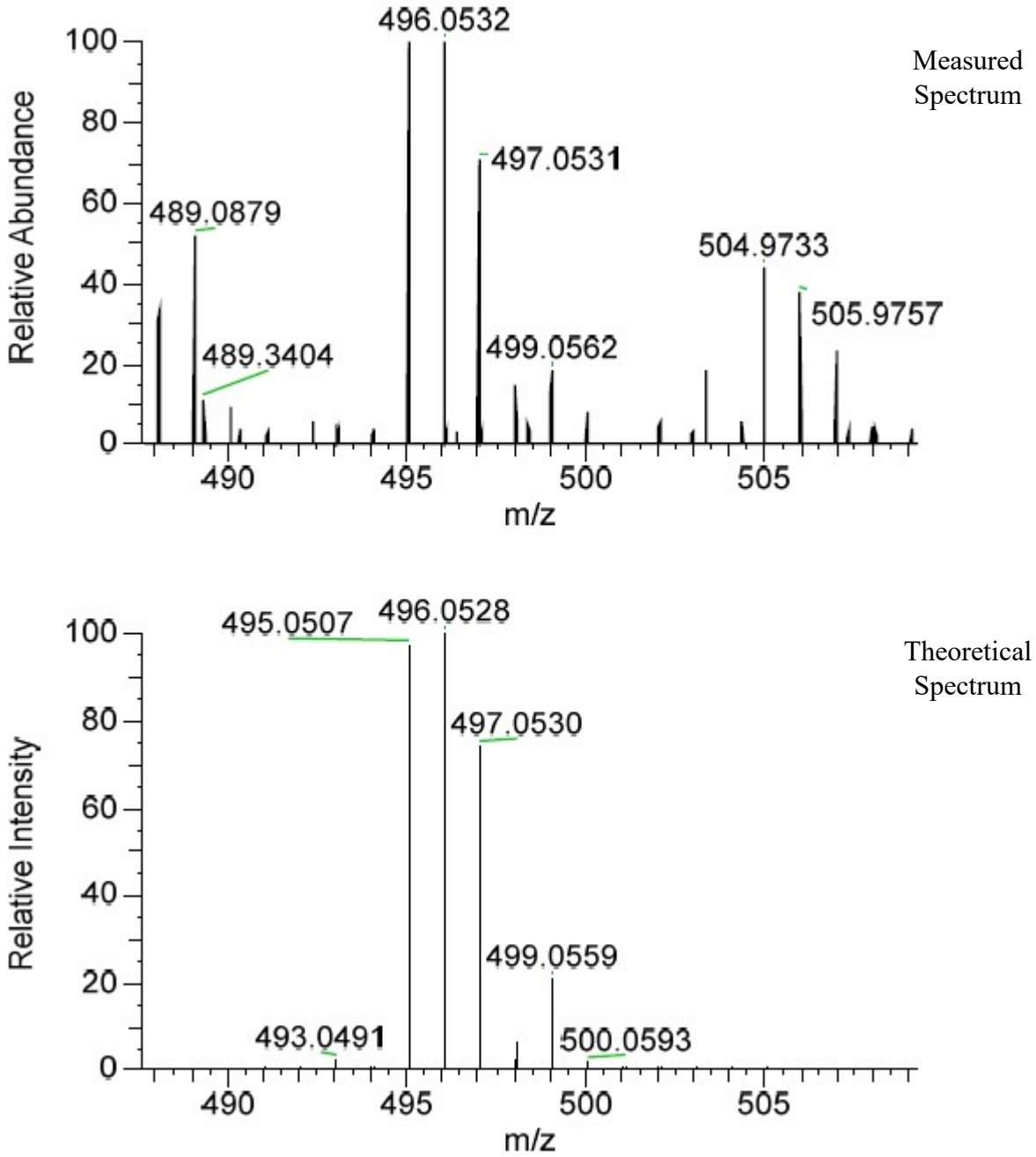

Figure A3.4 Accurate ESI-MS for trans,trans,trans-[Pt(pz)$_2$(N$_3$)$_2$(OH)$_2$] , fragment [M+Na]$^+$ (M_r = 496.05, accuracy 0.8 ppm).

A.4 DSC Data

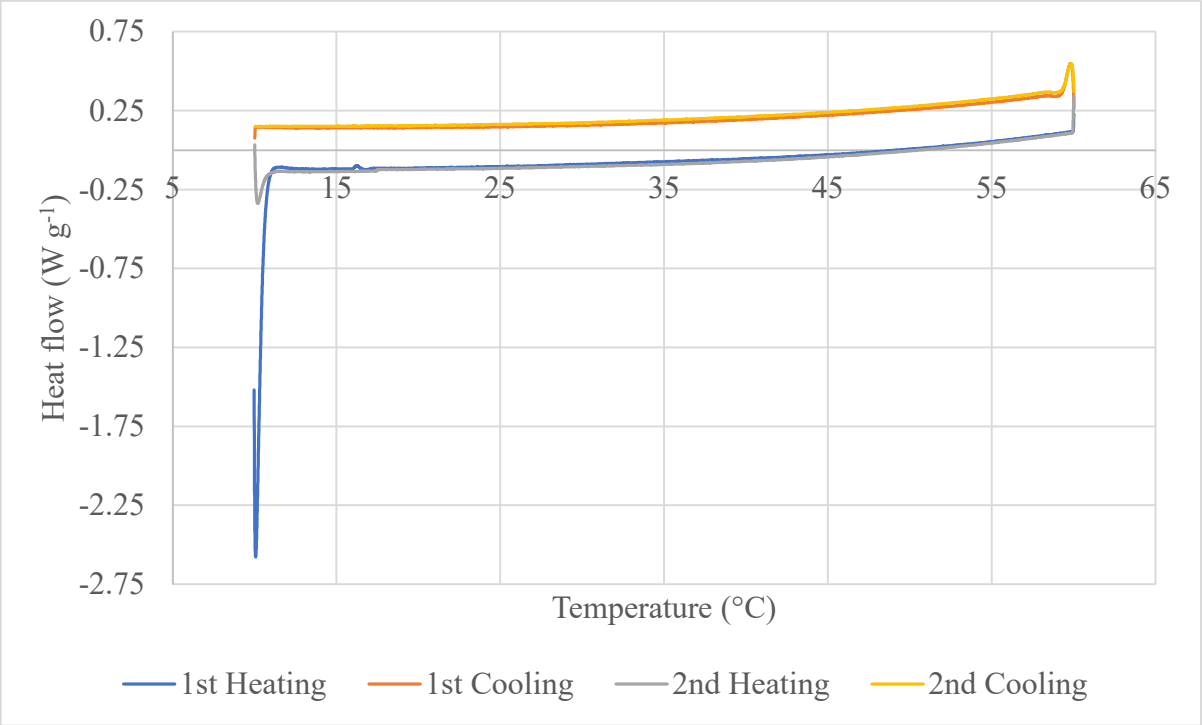

Figure A4.1 Thermal transition profiles for standard composition liposomes in sodium sulphate (200 mM).

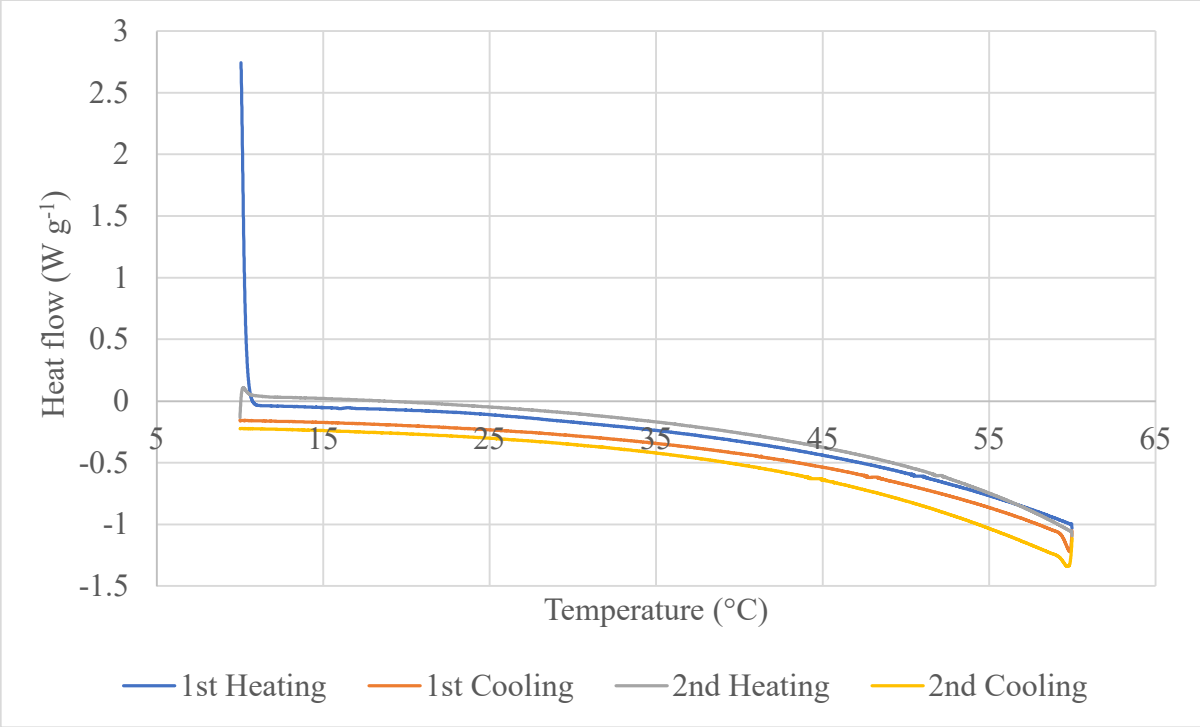

Figure A4.2 Thermal transition profiles for standard liposomes in calcium acetate (200 mM).

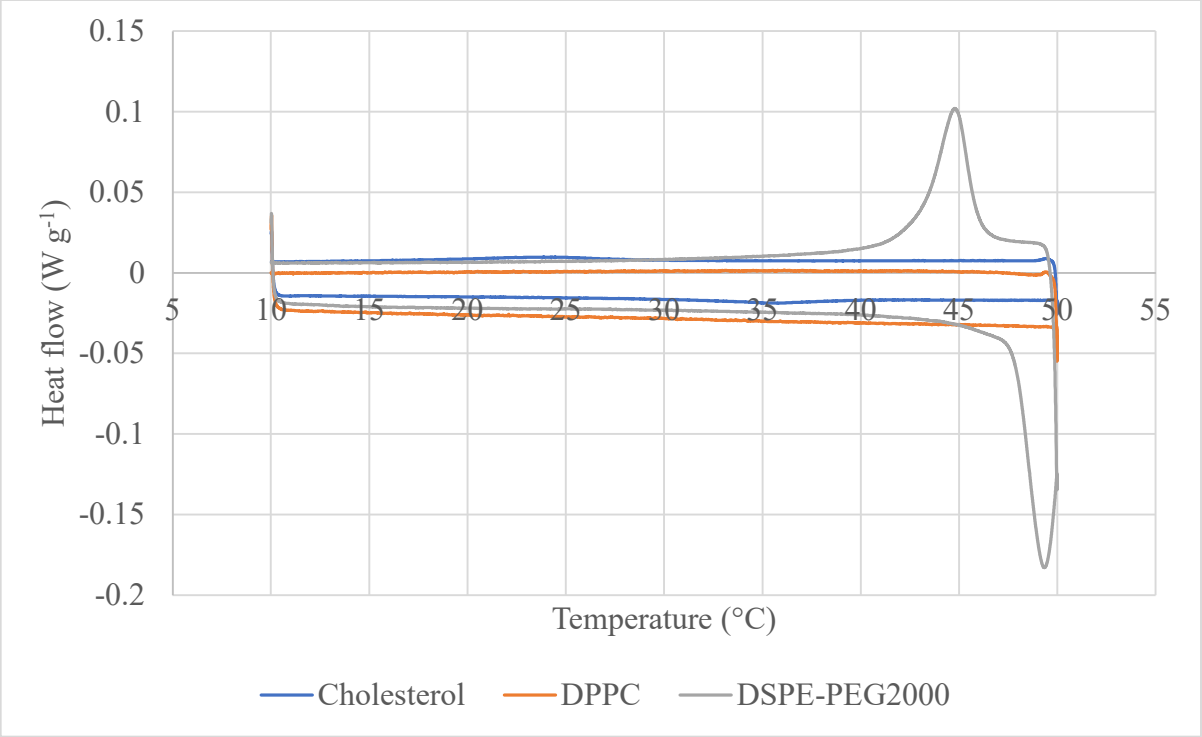

Figure A4.3 Thermal transition profiles for the individual solid lipids cholesterol (blue), DPPC (orange), and DSPE-PEG2000 (grey).

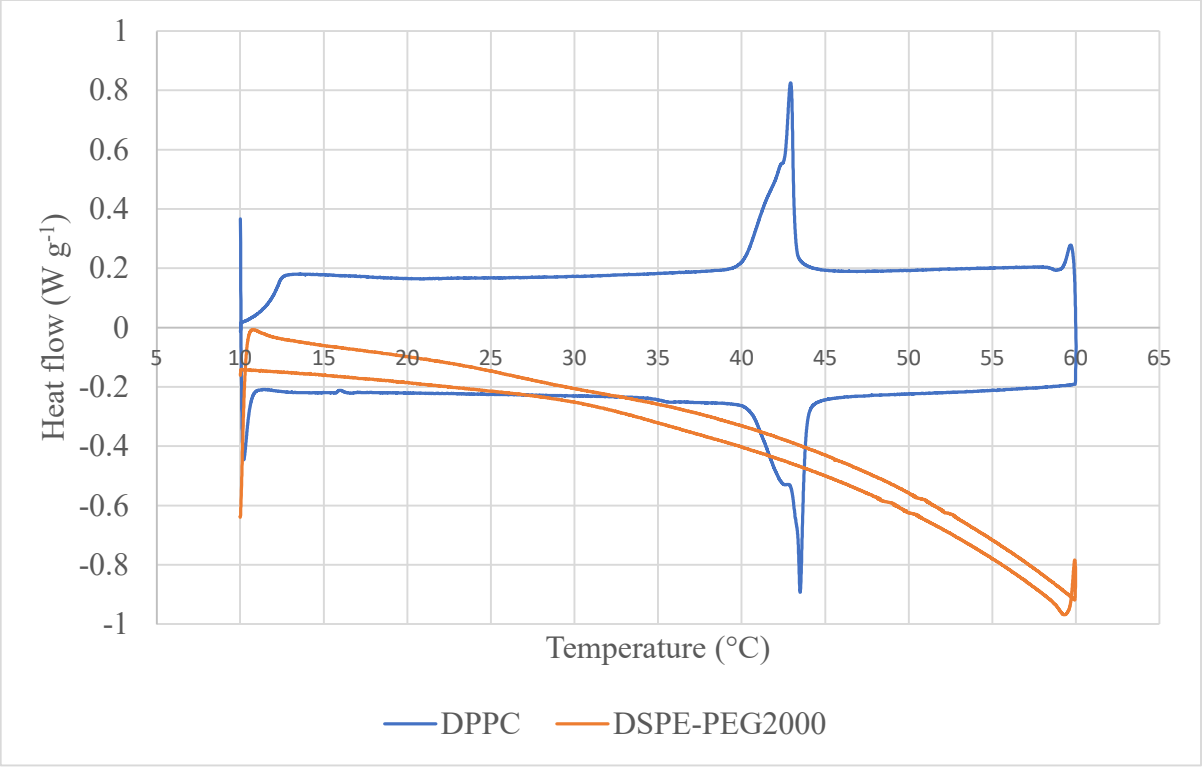

Figure A4.4 Thermal transition profile for liposomes made from the individual lipids DPPC (blue), and DSPE-PEG2000 (orange).

A.5 ICP-MS Data

Anomalous values are included in the same colour as the batch they are from, and are marked with an asterisk, but they have not been included on the trendlines. For cross-linked liposomes, days -1 and 0 represent the day of loading with -1 corresponding to the pre-UV sample and 0 corresponding to the post-UV sample.

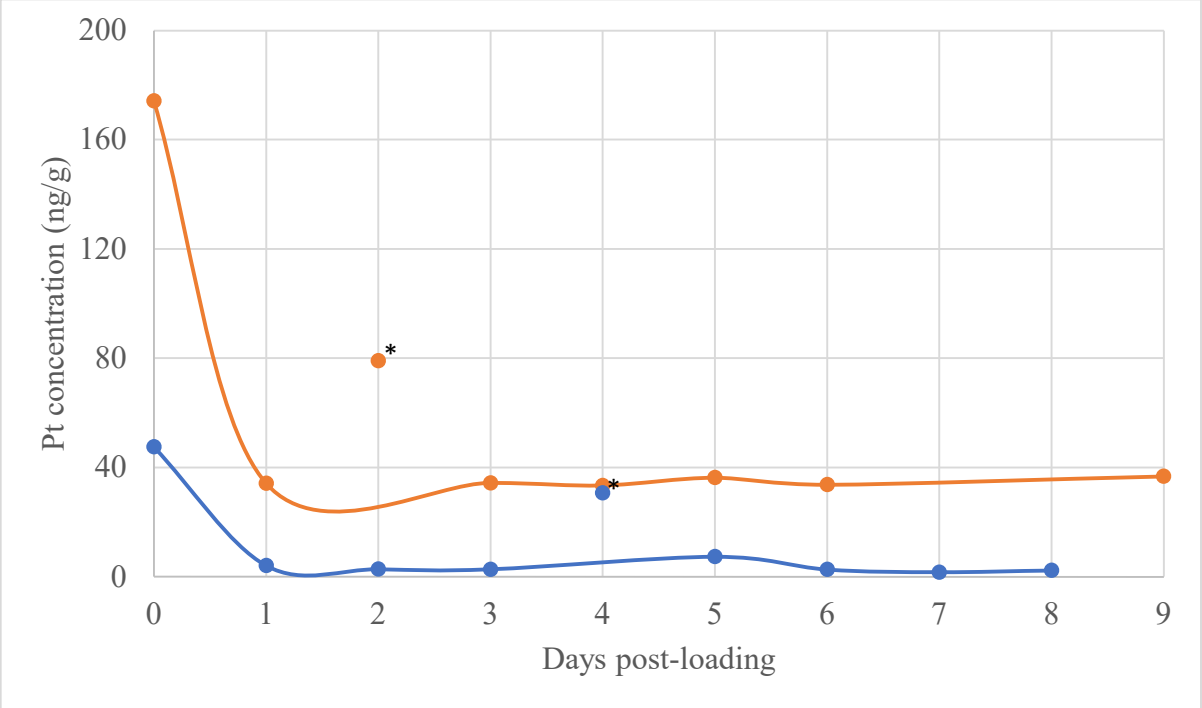

Figure A5.1 Change in Pt concentration of the intraliposomal matrix for standard liposomes loaded by the calcium acetate method; trans,trans,trans-$[Pt(py)_2(N_3)_2(OH)_2]$ (blue), iproplatin (orange).

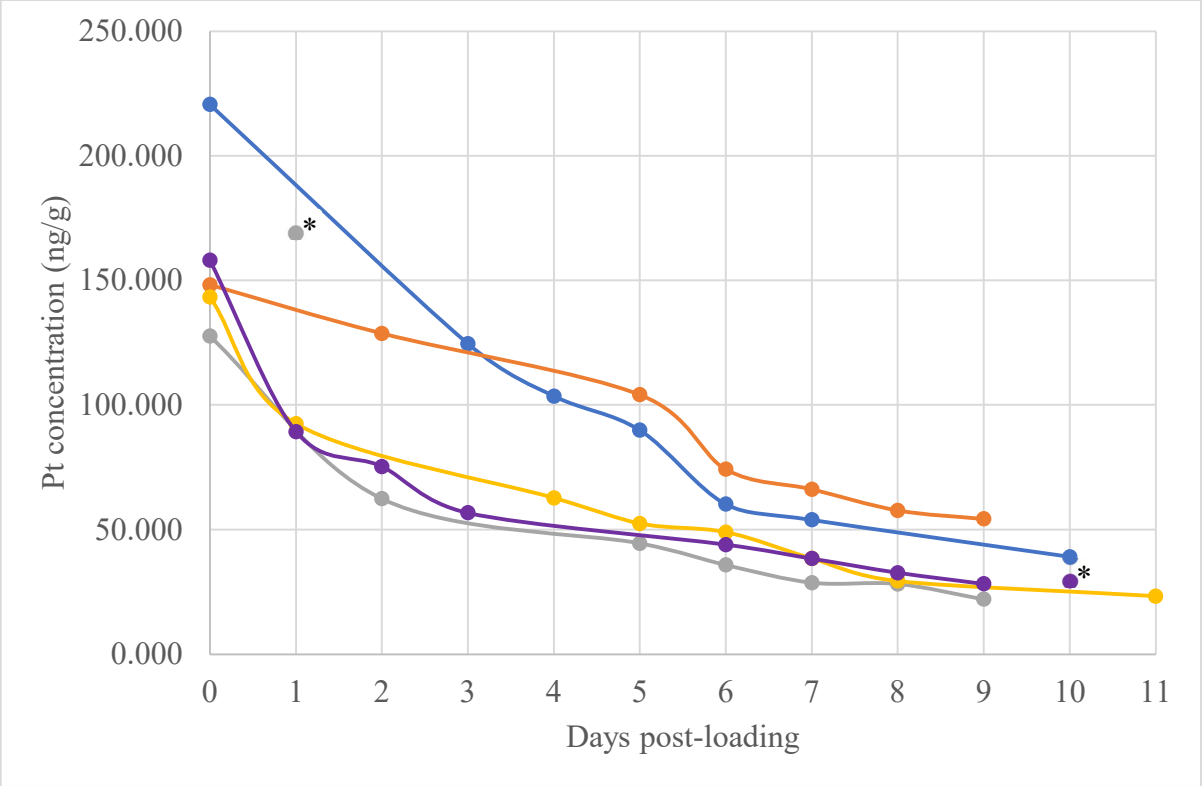

Figure A5.2 Change in Pt concentration of all batches of standard calcium acetate loaded liposomes; Blue - Batch 1, Orange - Batch 2, Grey - Batch 3, Yellow - Batch 4, Purple - Batch 5.

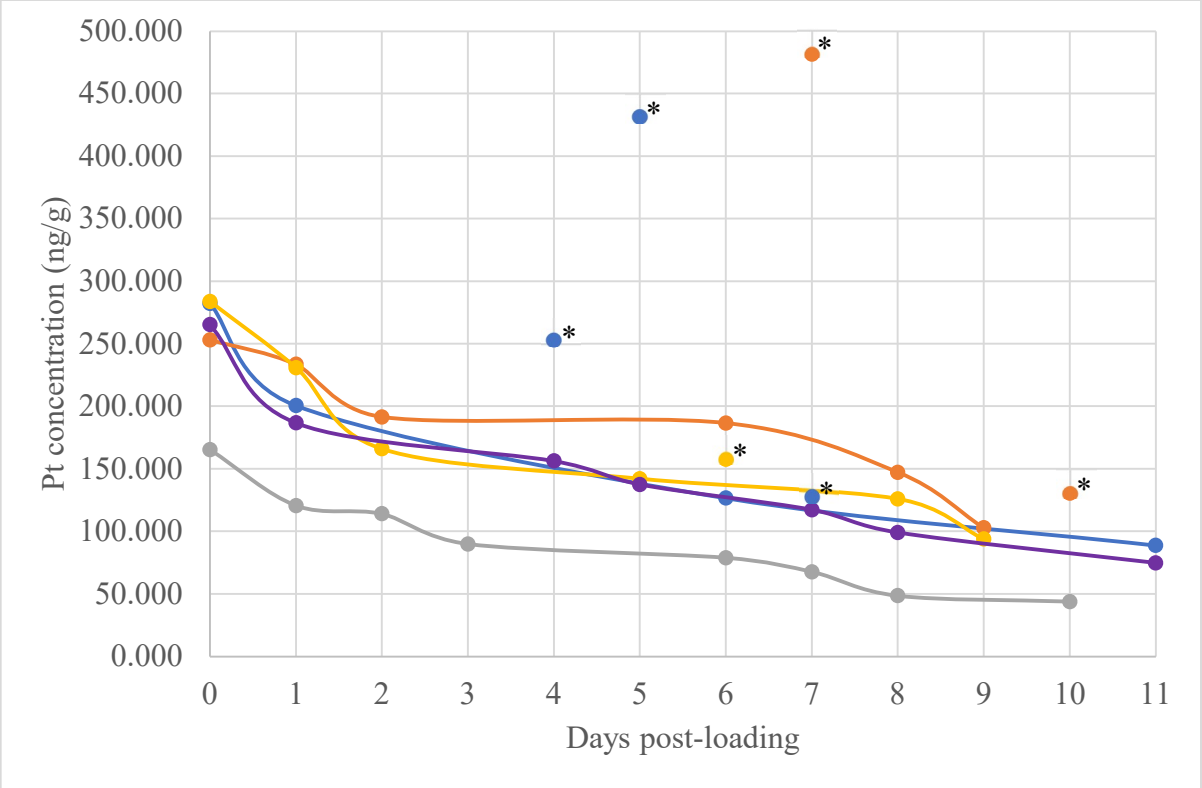

Figure A5.3 Graph showing all batches of standard ammonium sulphate loaded liposomes; Blue - Batch 1, Orange - Batch 2, Grey - Batch 3, Yellow - Batch 4, Purple - Batch 5.

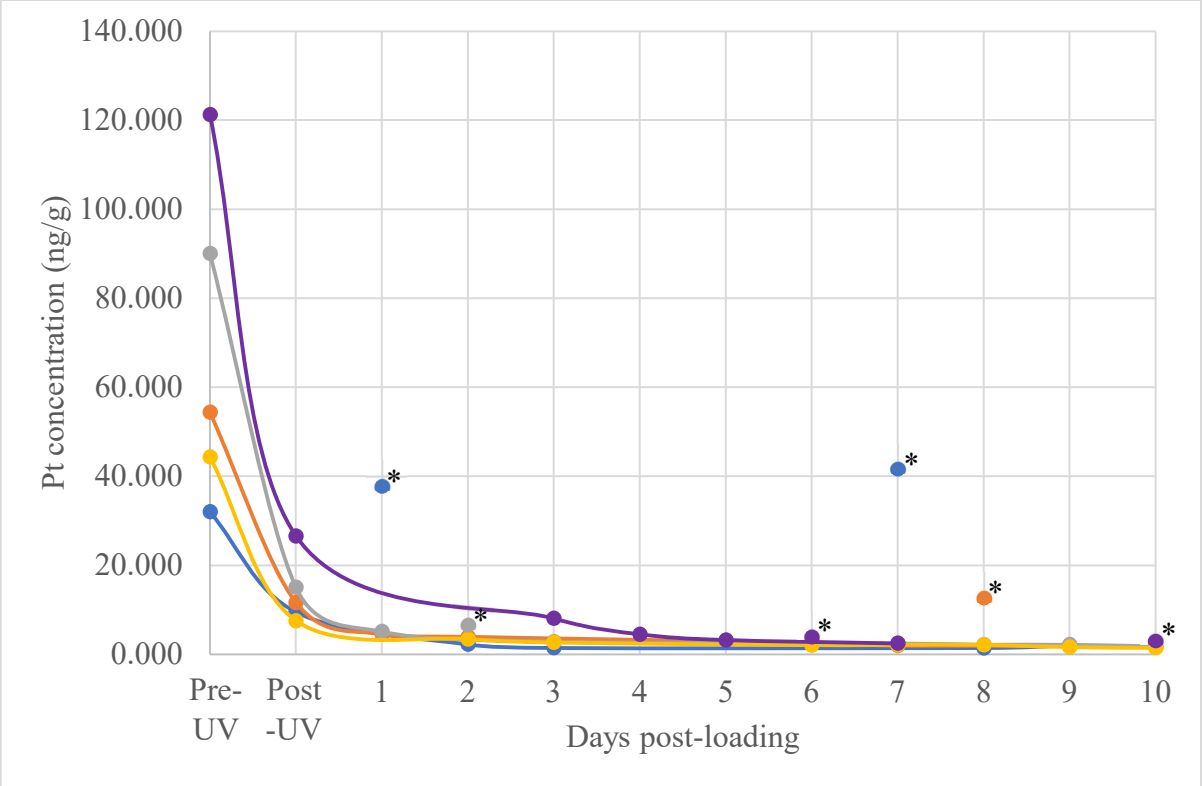

Figure A5.4 Graph showing all batches of cross-linked calcium acetate loaded liposomes; Blue - Batch 1, Orange - Batch 2, Grey - Batch 3, Yellow - Batch 4, Purple - Batch 5.

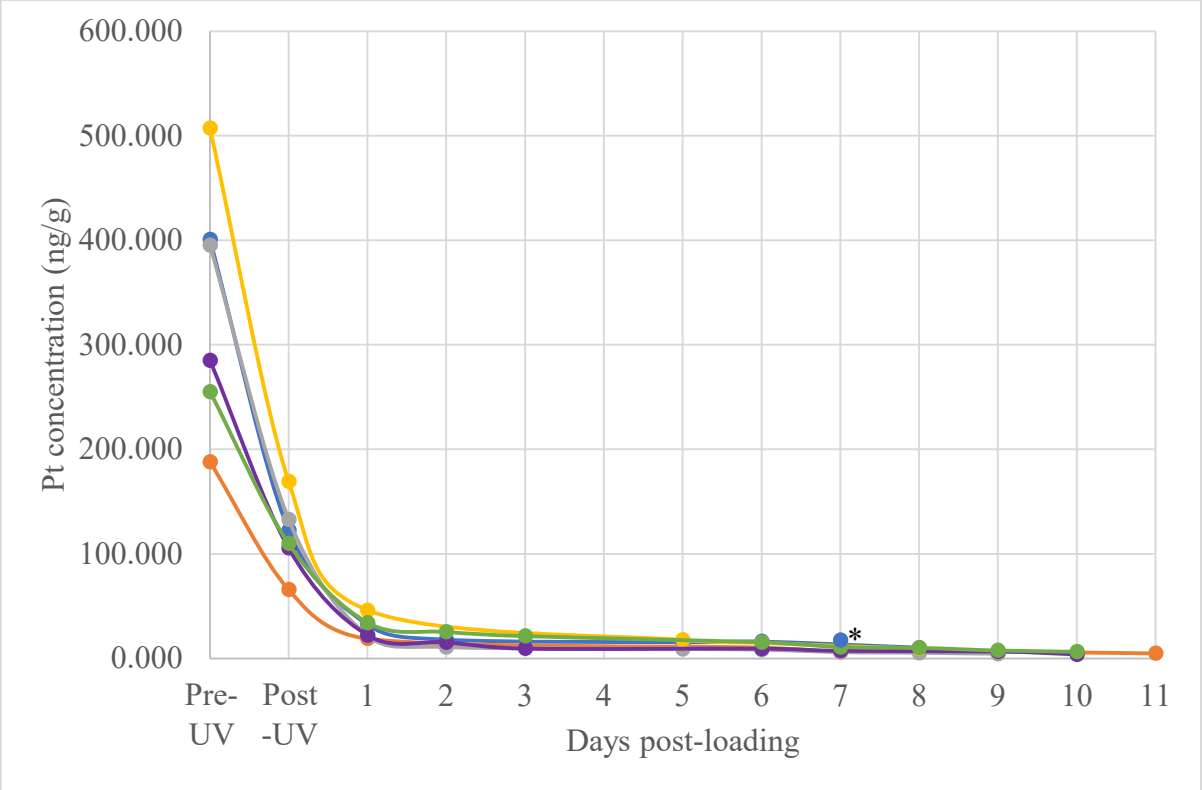

Figure A5.5 Graph showing all batches of cross-linked ammonium sulphate loaded liposomes; Blue - Batch 1, Orange - Batch 2, Grey - Batch 3, Yellow - Batch 4, Purple - Batch 5, Green – Batch 6.